

Free-form-deformation parameterization for multilevel 3D shape optimization in aerodynamics

Michele Andreoli, Janka Ales, Jean-Antoine Desideri

► **To cite this version:**

Michele Andreoli, Janka Ales, Jean-Antoine Desideri. Free-form-deformation parameterization for multilevel 3D shape optimization in aerodynamics. [Research Report] RR-5019, INRIA. 2003. inria-00071565

HAL Id: inria-00071565

<https://hal.inria.fr/inria-00071565>

Submitted on 23 May 2006

HAL is a multi-disciplinary open access archive for the deposit and dissemination of scientific research documents, whether they are published or not. The documents may come from teaching and research institutions in France or abroad, or from public or private research centers.

L'archive ouverte pluridisciplinaire **HAL**, est destinée au dépôt et à la diffusion de documents scientifiques de niveau recherche, publiés ou non, émanant des établissements d'enseignement et de recherche français ou étrangers, des laboratoires publics ou privés.



INSTITUT NATIONAL DE RECHERCHE EN INFORMATIQUE ET EN AUTOMATIQUE

***Free-form-deformation parameterization for
multilevel 3D shape optimization in aerodynamics***

Michele Andreoli — Aleš Janka — Jean-Antoine Désidéri

No 5019

Novembre 2003

THÈME 4

A large, light gray, stylized 'R' logo that overlaps the blue box.

R *apport
de recherche*



Free-form-deformation parameterization for multilevel 3D shape optimization in aerodynamics

Michele Andreoli ^{*}, Aleš Janka [†], Jean-Antoine Désidéri [‡]

Thème 4 — Simulation et optimisation
de systèmes complexes
Projet Opale

Rapport de recherche no 5019 — Novembre 2003 — 85 pages

Abstract: A versatile parameterization technique is developed for 3D shape optimization in aerodynamics. Special attention is paid to construct a hierarchical parameterization by progressive enrichment of the parametric space. After a brief review of possible approaches, the free-form deformation framework is elected for a 3D tensorial Bézier parameterization. The classical degree-elevation algorithm applicable to Bézier curves is still valid for tensor products, and its application yields a hierarchy of embedded parameterizations. A drag-reduction optimization of a 3D wing in transonic regime is carried out by applying the Nelder-Mead simplex algorithm and a genetic algorithm. The new parameterization including degree-elevation is validated by numerical experimentation and its performance assessed.

Key-words: shape optimization, Aerodynamics, simplex method, genetic algorithm, Bézier curves, multi-level parameterization, free-form deformation

^{*} Facoltà di Ingegneria Aerospaziale, Università di Pisa, Italy

[†] INRIA Sophia Antipolis, projet OPALE

[‡] INRIA Sophia Antipolis, projet OPALE

Une paramétrisation 3D de type “free-form” pour l’optimisation multi-niveau en aérodynamique

Résumé : On développe une technique versatile de paramétrisation pour l’optimisation de forme 3D en aérodynamique. On s’attache à construire une paramétrisation hiérarchique par enrichissement progressif de l’espace des paramètres. Après un bref exposé des approches possibles, on opte pour la formulation “free-form deformation” par le biais d’une paramétrisation de Bézier 3D par produit tensoriel. La hiérarchie des paramétrisations emboîtées s’appuie sur l’algorithme classique d’élévation du degré des paramétrisations de Bézier, encore applicable aux produits tensoriels. On traite un problème 3D de minimisation de la traînée d’une voilure d’avion en régime transsonique par l’algorithme du simplexe de Nelder-Mead et un algorithme génétique. On valide la méthode par expérimentation numérique et on évalue le gain en efficacité réalisé par la stratégie d’enrichissement.

Mots-clés : optimisation de forme, aérodynamique, méthode du simplexe, algorithme génétique, courbes de Bézier, paramétrisation multi-niveau, free-form deformation

Contents

1	Introduction	5
2	Shape Optimization in Aerodynamics	6
2.1	Flow Solver	7
	Discretization in space	7
	Boundary conditions	10
	Time integration	11
	Flow solver setup for optimization	12
3	Parameterization	12
3.1	Shape Representation	13
3.2	Bézier Curves	17
3.2.1	Polynomial Curves	17
3.2.2	The de Casteljau Algorithm	18
3.2.3	Properties of Bézier Curves	19
3.2.4	Bézier patches and volumes	21
3.3	Mesh Deformation	22
3.3.1	Linear and torsional springs for unstructured meshes	23
	Experiments	24
3.3.2	Transpiration Condition	25
3.3.3	Conclusion	27
4	Genetic Algorithms	28
4.1	Coding	28
4.1.1	Binary coding	29
4.2	Fitness function	30
4.3	Selection	30
4.3.1	Roulette-wheel	31
4.3.2	Tournament	32
4.4	Crossover	32
4.5	Mutation	32
4.6	Parameters of configuration	33
4.7	Conclusion	33
4.8	Validation of GAs on an analytic function	34
5	Derivative-Free Optimization Algorithms	35
5.1	Spendley, Hext and Himsworth simplex method	36
5.2	Nelder and Mead simplex method	36
5.2.1	Reflection	37
5.2.2	Expansion	37
5.2.3	Contraction	38
5.2.4	Reduction	39
5.3	Conclusion	39
6	Numerical Experiments	39
6.1	Geometry of the test-case wing	40
6.2	Computational Mesh	42

Simplex method	44
6.3 Simplex method for coarse parameterization (degree 6-1-1)	46
6.3.1 Simplex size	46
6.3.2 Non linear flow residual	48
6.4 Simplex method for rich parameterization (degree 9-1-1)	52
6.4.1 Simplex size	52
6.4.2 Non liner flow residual	54
6.5 Simplex method with degree elevation	57
6.5.1 Testcase 1: degree elevation for small simplex.	60
6.5.2 Testcase 2: degree elevation of best vs. all simplex vertices.	61
6.6 Parameterization enriching vs. finest parameterization only.	64
6.6.1 Large simplex	64
6.7 Summary and conclusions for simplex experiments	66
Genetic Algorithms	71
6.8 Set-up parameters for genetic algorithm	71
6.9 Genetic Range	71
6.10 Genetic algorithm with degree Elevation	75
6.10.1 Non linear flow residual	76
6.11 Degree elevation vs. fine parameterization only	77
6.12 Summary and conclusions for GAs experiments	81
7 Conclusions and perspectives	82

1 Introduction

Optimal Shape Design has been developed over the years, from the abstract field of calculus of variations to applications in structural mechanics and is becoming now a valuable tool for the design optimization in aeronautics, turbomachinery and automobile industry. Recent major improvements in CFD methods and optimization techniques were beneficial to 3D aircraft shape optimization, reducing significantly the time cycle for aircraft design through fully automated shape optimization. However, in order to be successfully employed at designing modern civil transport and business jets with more complex configurations, it is necessary to investigate new criteria and robust optimizers.

An essential issue in optimal shape design is the choice of parameterization for the shape. A survey of different shape parameterization techniques is proposed for example in Samareh [43]. The ultimate interest of a parametrization is to describe the shape or the shape modifications with a reduced set of parameters, which would still permit to satisfy a large set of industrial constraints, coming from geometry (thickness, volume, twist) or aerodynamics (lift, drag, or momentum). Still, such a set of parameters might be quite large, especially in 3D. Unfortunately, too rich parametrizations cause problems in the convergence of the optimization process, due to its stiffness and due to non-optimality of most of the optimization algorithms with respect to number of shape parameters. To overcome the stiffness of the optimization process, our idea, inspired by nested iterations for numerical resolution of PDEs, is to proceed by successive enriching/coarsening of parameterizations using a *multilevel* approach [27]. The goal is to unlock the stiffness of the system through the use of a coarse parametrization with only a few parameters.

Knowing what are the advantages and limits of each particular parametrization choice [43], in this paper we are presenting a kind of parametrization, based on Free Form Deformation [44], which allows us to parameterize complex shapes in 3D (wings or complete aircrafts) and allowing the implementation of a multilevel-approach. The proposed parameterization is then used in an optimization process to solve a 3D wing drag-reduction problem in transonic flow regime. The main objectives of the presented work are:

- to review different parametrization techniques and develop a parametrization using Free-Form Deformation with Bézier tensor-product (Bézier volume) for complex 3D shapes;
- to apply the parametrization to a 3D wing transonic optimization problem with one fixed flow regime;
- to validate the parametrization using Derivative-Free Optimization algorithms (Nelder-Mead simplex method and Genetic Algorithms);
- to apply a multilevel approach in the optimization process: progressive enriching of the search space through degree elevation (using the properties of Bézier curves).

In view of the objectives above, the paper is structured in the following way.

Chapter 2 introduces the general problem of optimal design in Aerodynamics and its mathematical description. It also contains a general description about drag force in Aerodynamics and about the flow solver. In a transonic regime, the presence of a shock wave has to be well detected. Different flow solver results are shown, comparing their quality and their CPU-cost.

Chapter 3 contains the description of the new parametrization technique. Free Form Deformation, with Bézier tensorial 3D parametrization (Bézier volume) is proposed to describe only the shape deformation, and not the shape itself. A review of Bézier curves, surfaces and volumes follows. Then, we discuss various mesh-deformation techniques, with particular interest

in linear/torsional springs and in simulating boundary deformation by transpiration boundary conditions.

Chapter 4 describes Genetic Algorithms. A summary of properties and characteristics of these algorithms is presented with a validation of the algorithm on a minimization problem with an analytical function.

Chapter 5 contains an introduction on Derivative-Free Optimization Algorithms and in particular concerns the simplex methods. Description of different simplex methods is given with a special attention to the Nelder-Mead simplex method.

Chapter 6 presents the results obtained in the optimization. We present the wing geometry and the 3D unstructured mesh created to simulate the flow-field around it. Using our parametrization, Nelder-Mead simplex method and Genetic Algorithms have been applied to solve the optimization problem. Different tests are done to see the influence of parameters like: degree of Bézier parametrization, simplex diameter, resolution of the flow, coding of parameters for the genetic algorithm. Ultimately, we discuss about the use of the multilevel approach.

The last Chapter concludes the work and presents the future perspectives.

2 Shape Optimization in Aerodynamics

The general problem of optimization is *a computational problem in which the object is to find the best of all possible solutions; more formally, to find a solution in the feasible region which has the minimum (or maximum) value of the objective function subject to some constraints.*

Three components describe such a problem: control (design) parameters x_c , the minimized objective (cost) functional $J(x_c)$, depending explicitly or implicitly (through a solution $W(x_c)$ of some physical state problem) on the values of design parameters, and the constraints. A general shape optimization problem can be expressed as a minimization problem over x_c in the form

$$\begin{aligned} J(x_c, W(x_c), \nabla W(x_c)) &\rightarrow \min \\ E(x_c, W(x_c), \nabla W(x_c)) &= 0 \\ g_1(x_c) &\leq 0 \\ g_2(W(x_c)) &\leq 0 \end{aligned}$$

where E represents the state equations, W are state variables of the underlying physical problem, and g_1, g_2 are the geometrical and the state constraints, respectively.

For shape-optimization in aerodynamics, the design parameters usually specify aerodynamic bodies. The cost functional depends usually on the solution of a flow problem around these bodies. The geometrical constraints are usually imposed of thickness, volume or other geometrical quantities of the aerodynamic shape. Aerodynamic constraints are usually expressed in terms of the lift coefficient C_L , drag coefficient C_D or momentum coefficient C_M .

The evaluation of the objective (cost) function J needs a solution $W(x_c)$ of a flow problem, obtained by resolution of a system of PDEs. Different levels of approximations are possible in modelling the flow physics: potential flow, inviscid flow (Euler), viscous flow (Navier-Stokes), mean-time averaged turbulent flow (Reynolds-averaged Navier-Stokes - RANS), direct numerical simulation (DNS), large-eddy simulations (LES). The computational cost and the need for computer resources grow rapidly with the complexity of the model, considering the fact that a typical optimization requires to evaluate cost-functional for hundreds or thousands different shapes x_c .

Various optimization techniques are possible to minimize the objective function: deterministic or stochastic, gradient-based or gradient-free methods.

The *deterministic* methods, or gradient-based methods, are based on the gradient of the cost function. Through the knowledge of gradient, the minimization direction is found. Such problem of optimal design can be treated within the mathematical theory of control of systems described by partial differential equations.

The *stochastic* methods choose solutions by a random process. The most known are the evolutionary algorithms and the genetic algorithms. They both mimic the process of natural evolution but they are different in the structure.

The *gradient-free* methods work without the knowledge of cost-function derivatives. The most known are the direct-search optimization algorithms: pattern search methods, simplex methods and methods with adaptive sets of search directions.

2.1 Flow Solver

In our optimization we have restricted ourselves to inviscid flows in 3D modelled by the Euler equations. The equations can be written in a conservative form:

$$\frac{\partial W}{\partial t} + \vec{\nabla} \cdot \vec{F}(W) = 0 \quad , \quad W = (\rho, \rho \vec{U}, E)^T \quad , \quad \vec{\nabla} = \left(\frac{\partial}{\partial x}, \frac{\partial}{\partial y}, \frac{\partial}{\partial z} \right)^T \quad (1)$$

where $\vec{F}(W) = (F_1(W), F_2(W), F_3(W))^T$ is the vector of the convective fluxes whose components are given by:

$$F_1(W) = \begin{pmatrix} \rho u \\ \rho u^2 + p \\ \rho uv \\ \rho uw \\ u(E + p) \end{pmatrix} \quad , \quad F_2(W) = \begin{pmatrix} \rho v \\ \rho v^2 + p \\ \rho vw \\ \rho vw \\ v(E + p) \end{pmatrix} \quad , \quad F_3(W) = \begin{pmatrix} \rho w \\ \rho w \\ \rho vw \\ \rho w^2 + p \\ w(E + p) \end{pmatrix}$$

In the expression (1), ρ is the density, $\vec{U} = (u, v, w)^T$ is the velocity vector, E is the total energy per unit of volume and p denotes the pressure. The pressure is deduced from the other variables using the state equation for a perfect gas

$$p = (\gamma_p - 1) \left(E - \frac{1}{2} \rho \|\vec{U}\|^2 \right)$$

where γ_p is the ratio of specific heats ($\gamma_p = 1.4$ for the air).

Discretization in space The flow domain Ω is assumed to be a polygonal bounded region of \mathbb{R}^2 . It is discretized by a triangulation \mathcal{T}_h , where h is the maximal length of the edges of \mathcal{T}_h . A vertex of the mesh is denoted by s_i , and the set of neighboring vertices by $N(s_i)$. We associate to each vertex S_i a control surface (or cell) denoted by C_i , which is constructed as the union of local contributions from the set of triangles sharing s_i . The contribution of a given triangle is obtained by joining its barycenter G to the midpoints I of the edges adjacent to s_i (see Fig. 1).

The boundary of C_i is denoted by ∂C_i and the unitary normal vector exterior to ∂C_i by $\vec{v}_i = (v_{ix}, v_{iy})$. The union of all these cells constitutes a discretization of Ω often qualified as dual to \mathcal{T}_h :

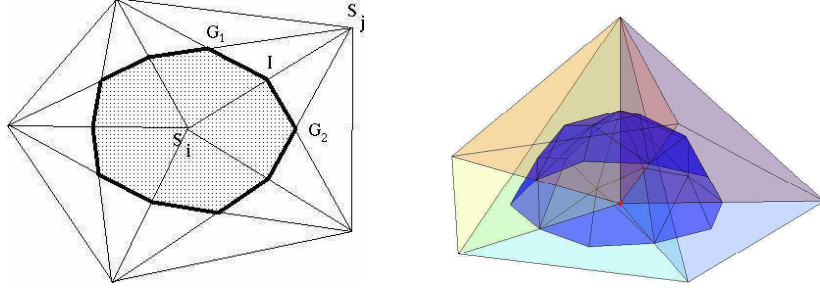


Figure 1: Barycentric control cell C_i on a 2D triangular mesh (left), half-cell in 3D (right)

$$\Omega_h = \bigcup_{i=1}^{N_v} C_i,$$

where N_v is the number of vertices of \mathcal{T}_h .

The spatial discretization method combines the following elements:

- a finite volume formulation together with upwind scheme for the discretization of the convective fluxes,
- extension to second order accuracy is obtained by using the MUSCL (Monotonic Upwind Schemes for Conservative Laws) introduced by van Leer [49] and extended to unstructured triangular meshes by Fezoui and Stoufflet [8].

Integrating Eq. (1) over C_i and using Gauss theorem results in :

$$\begin{aligned} \int \int_{C_i} \frac{\partial W}{\partial t} d\vec{x} + \sum_{j \in N(i)} \int_{\partial C_{ij}} \vec{F}(W) \cdot \vec{v}_i d\sigma \\ + \int_{\partial C_i \cap \Gamma_w} \vec{F}(W) \cdot \vec{n}_i d\sigma + \int_{\partial C_i \cap \Gamma_\infty} \vec{F}(W) \cdot \vec{n}_i d\sigma = 0, \end{aligned} \quad (2)$$

where $\partial C_{ij} = \partial C_i \cap \partial C_j$. A first order finite volume approximation of the first term of (2) can be written as:

$$W_i^{n+1} - W_i^n + \Delta t \sum_{j \in N(i)} \phi_F(W_i^n, W_j^n, \vec{v}_{ij}) = 0 \quad (3)$$

where ϕ_F denotes a numerical flux function such that:

$$\phi_F(W_i, W_j, \vec{v}_{ij}) \approx \int_{\partial C_{ij}} \vec{F}(W) \cdot \vec{v}_i d\sigma \quad , \quad \vec{v}_{ij} = \int_{\partial C_{ij}} \vec{v}_i d\sigma \quad (4)$$

The numerical flux (4) yields a conservative scheme if for any edge $[s_i, s_j]$ the following condition is verified:

$$\phi_F(W_i, W_j, \vec{v}_{ij}) = -\phi_F(W_j, W_i, \vec{v}_{ji}). \quad (5)$$

Upwinding is introduced in the calculation of (3) by using the approximate Riemann solver of Roe [42] which gives:

$$\phi_F(W_i, W_j, \vec{v}_{ij}) = \frac{\vec{F}(W_i) + \vec{F}(W_j)}{2} \cdot \vec{v}_{ij} - |A_R(W_i, W_j, \vec{v}_{ij})| \frac{(W_j - W_i)}{2}, \quad (6)$$

where $A_R(W_i, W_j, \vec{v}_{ij}) = \left(\frac{\partial F}{\partial W}(W_i, W_j, \vec{v}_{ij}) \right)_R$ is the so-called matrix of Roe that verifies the following property:

$$A_R(W_i, W_j, \vec{v}_{ij})(W_j - W_i) = F(W_j, \vec{v}_{ij}) - F(W_i, \vec{v}_{ij}) \quad (7)$$

with:

$$F(W, \vec{v}_{ij}) = \vec{F}(W) \cdot \vec{v}_{ij} \quad (8)$$

The numerical flux (6) can thus be reformulated as:

$$\phi_F(W_i, W_j, \vec{v}_{ij}) = F(W_j, \vec{v}_{ij}) - A_R^+(W_i, W_j, \vec{v}_{ij})(W_j - W_i) \quad (9)$$

or as :

$$\phi_F(W_i, W_j, \vec{v}_{ij}) = F(W_j, \vec{v}_{ij}) + A_R^-(W_i, W_j, \vec{v}_{ij})(W_j - W_i) \quad (10)$$

with $A_R(W_i, W_j, \vec{v}_{ij}) = A_{\vec{v}_{ij}}(\tilde{W})$ with the Roe average state (\tilde{W}) given by:

$$\begin{cases} \tilde{W} &= (\tilde{\rho}, \tilde{\rho}\tilde{u}, \tilde{\rho}\tilde{v}, \tilde{E})^T \\ \tilde{\rho} &= (\sqrt{\rho_1}\rho_1 + \sqrt{\rho_2}\rho_2)/(\sqrt{\rho_1} + \sqrt{\rho_2}) \\ \tilde{u} &= (\sqrt{\rho_1}u_1 + \sqrt{\rho_2}u_2)/(\sqrt{\rho_1} + \sqrt{\rho_2}) \\ \tilde{v} &= (\sqrt{\rho_1}v_1 + \sqrt{\rho_2}v_2)/(\sqrt{\rho_1} + \sqrt{\rho_2}) \\ \tilde{H} &= (\sqrt{\rho_1}H_1 + \sqrt{\rho_2}H_2)/(\sqrt{\rho_1} + \sqrt{\rho_2}) \end{cases} \quad (11)$$

where $H = \frac{\gamma p}{(\gamma-1)\rho} + \frac{u^2+v^2}{2}$ is the total enthalpy per unit volume. On the other hand, we have that:

$$A^\pm(\tilde{W}) = T(\tilde{W})\Lambda^\pm(\tilde{W})T^{-1}(\tilde{W}) \quad (12)$$

with:

$$\Lambda = \left(\vec{U} \cdot \vec{v} - c, \vec{U} \cdot \vec{v}, \vec{U} \cdot \vec{v}, \vec{U} \cdot \vec{v} + c \right)^T, \quad (13)$$

where $c = \sqrt{\gamma \frac{p}{\rho}}$ denotes the speed of sound. The MUSCL technique [49] for the extension to a second order approximation of (4) relies on a linear interpolation of the state vector W_{ij} and W_{ji} at the interface (I_{ij}) between cells C_i and C_j :

$$\tilde{W}_{ij} = \tilde{W}_i + \frac{1}{2}(\vec{\nabla}\tilde{W})_i \cdot s_i \vec{s}_j, \quad \tilde{W}_{ji} = \tilde{W}_j - \frac{1}{2}(\vec{\nabla}\tilde{W})_j \cdot s_i \vec{s}_j, \quad (14)$$

where $\tilde{W} = \left(\rho, \vec{U}, p \right)^T$ (see Fig 2). The interpolation is done using the physical variables instead of the conservative variables. Then, the interpolated states (14) are used as arguments to the numerical flux function (3).

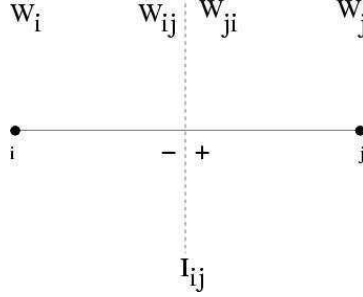


Figure 2: Interpolated physical states W_{ij} and W_{ji} between cells C_i and C_j .

The nodal gradients $(\vec{\nabla}\tilde{W})_i$ are obtained from a weighted average of the P1 Galerkin (centered) gradients computed on each triangle of the finite element support of s_i :

$$(\vec{\nabla}\tilde{W})_i = \frac{\int \int_{C_i} \vec{\nabla}\tilde{W}|_T d\vec{x}}{\int \int_{C_i} d\vec{x}} = \frac{1}{\text{area}(C_i)} \sum_{T \in C_i} \frac{\text{area}(T)}{3} \sum_{k=1, k \in T}^3 (\tilde{W})_k \vec{\nabla}\phi_k^T \quad (15)$$

where $\phi_k^T(x, y, z)$ is the P1 basis function defined at the vertex S_k and associated with the triangle T . The construction given by Eq.(14)-(15) results in a half-upwind scheme which is second order accurate but can present spurious oscillations in the solution, expressing a loss of monotony. A classical way to remedy this problem is to make a compromise between the first order and the second order schemes through the use of a slope limitation procedure.

Boundary conditions The terms 3 and 4 in the second line of Eq. (2) are associated with the boundary conditions of the problem. These are now taken into account in the weak formulation. The following situations are considered:

- *solid wall*. We impose on Γ_w the slip condition $\vec{U} \cdot \vec{n} = 0$. This condition is introduced in the corresponding term of Eq.(2) which results in :

$$\int_{\partial C_i \cap \Gamma_w} \vec{F}(W) \cdot \vec{n}_i d\sigma = p_i \cdot \text{area}(\partial C_i) \begin{pmatrix} 0 \\ \tilde{n}_{ix} \\ \tilde{n}_{iy} \\ 0 \end{pmatrix} \quad (16)$$

- *far-field boundary*. On Γ_∞ , we make use of a uniform flow state vector, i.e. we assume that the flow at infinity is uniform (this assumption is valid for external flows):

$$\rho_\infty = 1, \vec{U}_\infty = (u_\infty, v_\infty)^T \quad \text{with} \quad \|\vec{U}_\infty\| = 1, p_\infty = \frac{1}{\gamma M_\infty^2} \quad (17)$$

where M_∞ is the far-field Mach number. Here, an *upwind-downwind* flux decomposition is used between the external information (W_∞) and the state vector W_i associated to a boundary vertex $s_i \in \Gamma_\infty$. More precisely, the corresponding boundary integral of the second term of Eq.(2) is evaluated through a non-reflexive version of the Steger and

Warming flux decomposition:

$$\int_{\partial C_i \cap \Gamma_\infty} \vec{F}(W) \cdot \vec{n}_i d\sigma = A^+(W_i, \vec{n}_{i\infty}) \cdot W_i + A^-(W_i, \vec{n}_{i\infty}) \cdot W_\infty. \quad (18)$$

Time integration Assuming $W(\vec{x}, t)$ constant on each cell C_i (in other words a mass lumping technique is applied to the temporal term in Eq.(2)) we obtain the following set of semi-discrete equations:

$$area(C_i) \frac{dW_i^n}{dt} + \Psi(W_i^n) = 0 \quad , \quad i = 1, \dots, N_v, \quad (19)$$

where $W_i^n = W(\vec{x}_i, t^n)$, $t^n = n\Delta t^n$ and:

$$\Psi(W_i^n) = \sum_{j \in N(i)} \phi_F(W_{ij}, W_{ji}, \vec{v}_{ij}) + \int_{\partial C_i \cap \Gamma} \vec{F}(W) \cdot \vec{n}_i d\sigma. \quad (20)$$

Explicit time integration procedures for time integration of (19) are subject to a stability condition expressed in terms of a CFL (Courant-Friedrichs-Lewy) number. An efficient time advancing strategy can be obtained by means of a implicit linearized formulation such as the one described in Fezoui and Stoufflet [8] and briefly outlined here. First, the implicit variant of Eq. (19) writes as:

$$\frac{area(C_i)}{\Delta t^n} \delta W_i^{n+1} + \Psi(W_i^{n+1}) = 0 \quad , \quad i = 1, \dots, N_v \quad (21)$$

where $\delta W_i^{n+1} = W_i^{n+1} - W_i^n$. Then, applying a first order linearization to the nodal flux $\Psi(W_i^{n+1})$ yields the Newton-like formulation :

$$\left(\frac{area(C_i)}{\Delta t^n} + \frac{\partial \Psi(W^n)}{\partial W} \right) \delta W^{n+1} = -\Psi(W_i^n) \quad (22)$$

In practice, we replace the exact Jacobian of the second order flux $\frac{\partial \Psi(W^n)}{\partial W}$ by an approximate Jacobian matrix $J(W^n)$ resulting from the analytical differentiation of the first order flux (6) with respect to the cell-averaged states W_i :

$$P(W^n) \delta W^{n+1} = \left(\frac{area(C_i)}{\Delta t^n} + J(W^n) \right) \delta W^{n+1} = -\Psi(W_i^n). \quad (23)$$

The resulting Euler implicit time integration scheme is in fact a modified Newton (see Fezoui and Stoufflet [8] for details). As a consequence, one cannot ensure that this formulation will yield a quadratically converging method for time steps tending to infinity. The matrix $P(W^n)$ is sparse and has the suitable properties (diagonal dominance (ie. M-matrix) in the scalar case) allowing the use of a relaxation procedure (Jacobi or Gauss-Seidel) in order to solve the linear system of Eq.(22). Moreover, an efficient way to get second order accurate steady solutions while keeping the interesting properties of the first order upwind matrix is to use the second order elementary convective fluxes based on Eq.(14)-(15) in the right-hand side of Eq. (22). The above implicit time integration technique is well suited to steady flow calculations; for unsteady flow computation, this first order time accurate scheme is generally unacceptably dissipative.

Flow solver setup for optimization For resolution of the Euler problem, we have chosen an implicit scheme with Roe Flux approximation combined with MUSCL and van Albada limiters [48]. For approximative resolution of the linear system at each time-step we use a few relaxation of Gauss-Seidel method.

The stopping criteria is based on l^2 norm of the numerical flux in Energy equation. By an l^2 norm of energy residual we mean a Euclidean norm over the degrees of freedom in the right-hand side of the linear system, corresponding to discretization of total energy E . We will call it the *non-linear flow residual*.

3 Parameterization

One of the crucial points in the correct definition of a shape optimization problem is the choice of the parameterization technique describing the optimal shape. Such a parameterization should be:

- *versatile*: possibility to describe quite a broad spectrum of potentially complex 3D shapes with geometrical constraints,
- *concise*: it should use as few parameters as possible, because the number of design parameters heavily affect the CPU cost of the optimization process.

In this respect, we could use an a-priori approximate knowledge of the expected shape of the searched optimum (or its regularity). Moreover, in addition of the two crucial properties above, we search for parameterizations in which one can introduce the notion of:

- parameterization hierarchy,
- self-adaptivity.

A survey of shape parameterization techniques is proposed in Samareh [43]. The most used approaches are as the following.

- **Discrete Approach**: it is based on using the coordinates of the boundary points as design variables (see Fig. 3(a)). This approach is easy to implement. However, it is too much connected to the solution mesh and does not enable adaptive-mesh flow evaluations. Due to the excessive refinement of the parametrization, comparable to the resolution of the mesh, it is difficult to maintain a smooth geometry of the optimized shape. For a model with a large number of grid points, the number of design variables often becomes very large, which leads to high cost and a difficult (stiff) optimization problem to solve. It is easy to parameterize complex 3D objects, but there are some problems with definition of normals to a discrete surface (see Fig. 3(b)). Hierarchical parameterization using this approach might be done for example by agglomeration [27].
- **Polynomial and Spline Approaches**: the shape is described by a polynomial curve in a very compact form with a small set of design variables. For example, with a Bézier curve, the control points are used as design variables (see Fig. 4). Despite recent progress, it is still difficult to parameterize and construct complex, three-dimensional models based only on polynomial and spline representations. Complex shape requires a large number of control points. The smoothness of the shape deformation is assured. Moreover, with Bézier parameterization, the property of degree elevation (Section 3.2.3) might be employed to construct a hierarchical parametrization.

- **CAD-based Approach:** most solid modelling CAD systems use either a boundary representation (B-Rep) or a constructive solid geometry method to represent a physical, solid object. Based on a complete mathematical definition of a solid, it is possible to create a complete geometry. These system use Boolean operations such as intersection and union of simple features (e.g. holes, slots, cuts, protrusion, fillets, chamfers, etc.). Existing Feature-based solid modelling (FBSM) CAD tools are not capable of calculating sensitivity derivatives analytically. After reconstructing the shape geometry, usually a new mesh must be generated.
- **Analytical Approach:** the formulation is based on adding shape functions (analytical functions) linearly to the baseline shape. All participating coefficients are initially set to zero, so the first computation gives the baseline geometry. The shape functions are smooth functions based on previous airfoil design. This method is very good for wing parameterization, but not simple to generalize for complex geometries.
- **Free Form Deformation (FFD) Approach:** FFD is one of the techniques of deforming computer-generated objects, which comes from Computer Graphics [44]. The FFD approach operates on the whole space regardless of the representation of the deformed objects embedded in the space. Instead of manipulating the object directly, FFD deforms a lattice that was built around the object . The lattice is a space, in the shape of a cube or an arbitrary volume [1], which wraps around the object . This lattice is basically a composite of Bézier tensor patches in 3D called a Bézier volume, but it is also possible to use B-spline or NURBS ([5], [22]). When we move the control points of the lattice, the lattice is deformed. At the same time, the object inside the lattice is deformed (see Fig. 5).

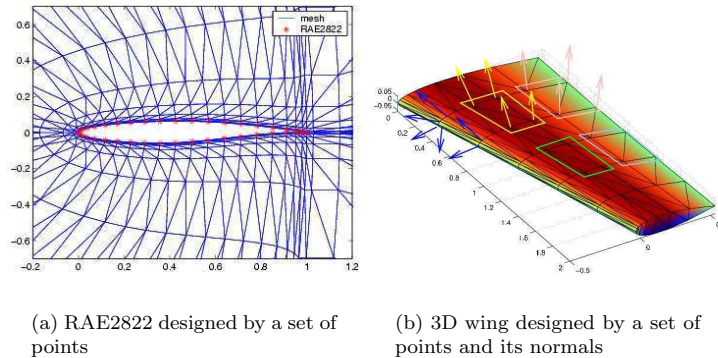


Figure 3: Discrete Approach

3.1 Shape Representation

In this work, the free-form deformation (FFD) method, with Bézier volume (the next section is a review about Bézier curves and its properties), has been applied.

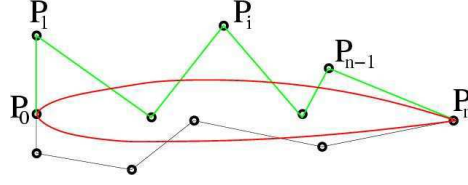


Figure 4: Polynomial approach

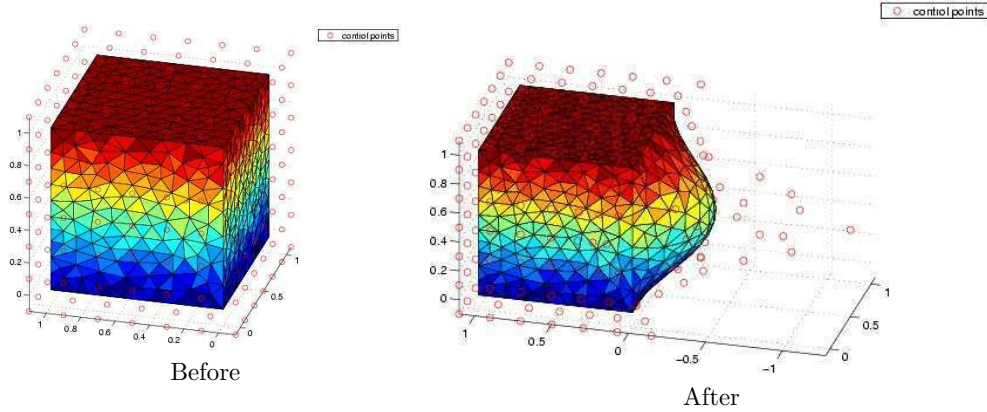


Figure 5: FFD Approach

One of the inconveniences of standard Bézier curves/patches is that they describe only smooth objects, and for a non-smooth object they need a very high order curves/patches (with danger of oscillation) or several curves/patches joined by some continuity condition C^0, C^1 . Using several glued patches puts an obstacle to the degree elevation process, which works only for one patch. A better idea is to describe through Bézier parameterization just the deformation and not the shape itself. We can write for any mesh node q :

$$\mathbf{x}_q = \mathbf{x}_q^{init} + \sum_{i=0}^l \sum_{j=0}^m \sum_{k=0}^n B_i^l(s_q) B_j^m(t_q) B_k^n(u_q) \delta \mathbf{p}_{ijk}$$

In this way, even if the shape is not smooth, we will look for a smooth deformation (see Fig. 6). For *Bézier delta formulation*, control points lose its meaning of position, the only input determining the parameterization is the assignment of Bézier parameters $\mathbf{t}_q = (s_q, t_q, u_q)$ for every node q of the mesh.

The choice of \mathbf{t}_q can modify the shape of the control box around the object. Suppose, for example, that we should search for an optimal wing whose form is obtained only by a linear interpolation of root and tip sections (no double curvature), and keeping fixed the leading edge and the trailing edge. If we choose for \mathbf{t}_q the node values of the mesh, the box will be like the one shown in Fig. 7, and the displacement of the control points at the tip section will not allow us to respect these constraints. For this reason, a new set of (s_q, t_q, u_q) coordinates might be calculated, through a scale factor between root and tip sections, which give us a box like the

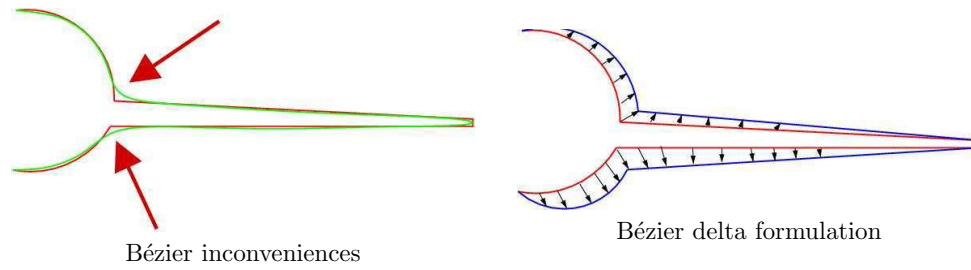


Figure 6: Bézier parameterization

one shown in Fig. 8 following tightly a given planform.

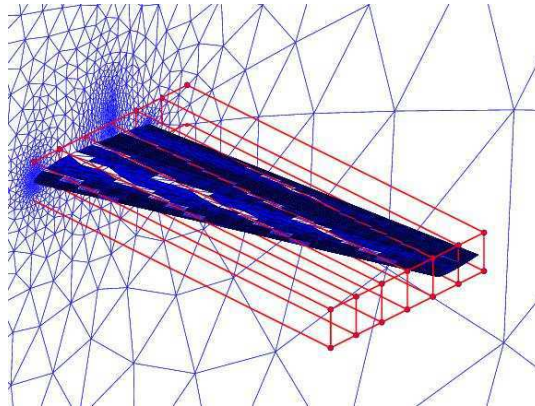


Figure 7: General box around the wing

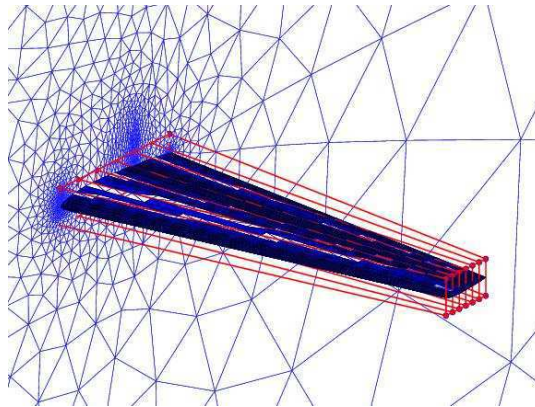


Figure 8: Box of Bézier control points around the wing

The choice of Bézier volume for FFD is done because of the degree elevation property (see Section 3.2.3). It will allow us to construct a hierarchy of embedded Bézier parameterizations

and a hierarchy of rigorously-nested optimization search spaces. The choice of degree of the tensorial Bézier representation in the three directions is up to the design engineers. In Chapter 6 we will show testcases with different degree but the way how we move the control points remains the same for different degree.

For example, if we look at a Bézier representation of order 6 (x direction), 1 (y direction), 1 (z direction) the box around the wing is like in Fig. 9. The four corners of the box are fixed, to keep fixed the leading and the trailing edge, and the resting control points can move only in y direction (see Fig. 10). Moreover, for the range of displacement of control points it is possible to use an arbitrary interval (for example 10% of root thickness or more). The choice of this range, as we will see in Chapter 6, has a direct implication for the results of the optimization when using genetic algorithms.

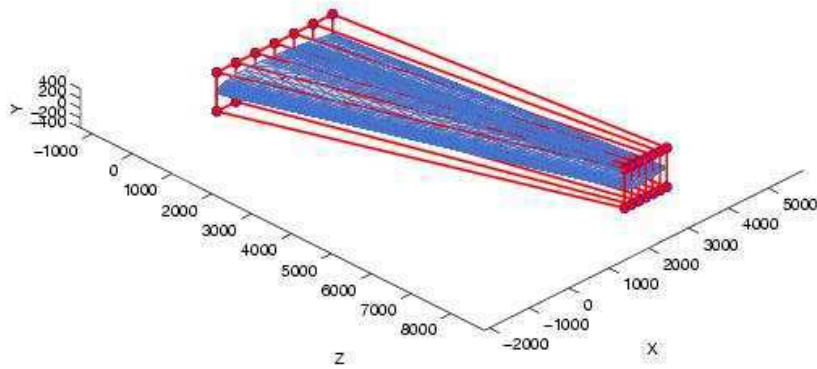


Figure 9: Example of Bézier representation, degree 6-1-1

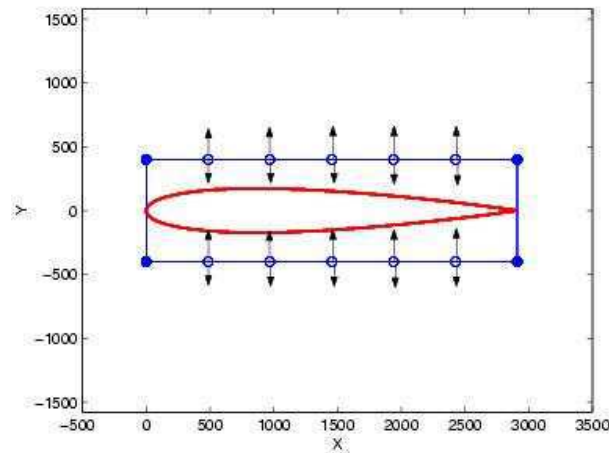


Figure 10: Root control point authorized displacements

We remark here that our parameterization is not limited to wings. In an optimization of engine-pylon-body junction for an aircraft, for example, the box should be like in Fig. 11.

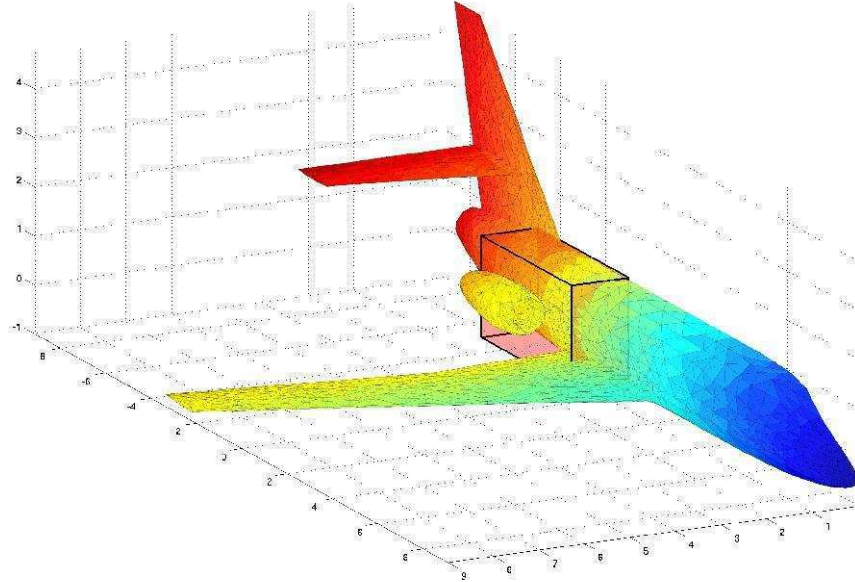


Figure 11: Free-form deformation for an engine-pylon-body optimization

3.2 Bézier Curves

The Bézier curve representation is used most frequently in computer graphics and geometric modelling. The curve is defined geometrically, which means that the parameters have a geometric meaning - they are just points in three-dimensional space. This parametrization was developed by two competing European engineers in the 1960s to attempt drawing automotive components. Two engineers responsible for their development were Pierre Bézier who worked for Renault and Paul de Casteljau who worked for Citroën. The curve was named after Pierre Bézier, even though de Casteljau first used the curve. Bézier was the first to publish and therefore the idea bears his name. Later, the curve was developed in the 1970s for CAD/CAM operations.

3.2.1 Polynomial Curves

A two-dimensional (three-dimensional, d -dimensional) *polynomial curve* is a parameterized curve $t \mapsto P(t)$:

$$P_n(t) = \sum_{i=0}^n a_i \cdot t^i = a_n t^n + \dots + a_1 t + a_0 \quad \text{with} \quad a_n, a_{n-1}, \dots, a_1, a_0 \in \mathbb{R}^2(\mathbb{R}^3, \mathbb{R}^d)$$

The set of all d -dimensional polynomial curves of degree n is denoted by P_n^d . The standard basis for P_n is the *monomial basis* $1, t, t^2, \dots, t^n$.

Another possible basis for P_n , used in the Bézier curves, is the basis of Bernstein polynomials. The polynomial

$$B_i^n(t) = \binom{n}{i} t^i (1-t)^{n-i}, \quad i = 0, \dots, n$$

is called the i^{th} Bernstein polynomial of degree n . Properties of the binomial coefficients are:

- definition: $\binom{n}{i} = \frac{n!}{i!(n-i)!}$
- recursive definition: $\binom{n}{i} = 1$, $\binom{n+1}{i+1} = \frac{n+1}{i+1} \binom{n}{i}$
- Pascal triangle: recursion $\binom{n+1}{i+1} = \binom{n}{i+1} + \binom{n}{i}$ and symmetry $\binom{n}{i} = \binom{n}{n-i}$

Properties of Bernstein polynomials are:

1. $\sum_{i=0}^n B_i^n(t) = (t + (1-t))^n$ (Binomial Theorem: $(a+b)^n = \sum_{k=0}^n \binom{n}{k} a^k b^{n-k}$)
2. $\sum_{i=0}^n B_i^n(t) = 1$ (partition of 1)
3. $B_i^n(t) \geq 0$, $t \in [0, 1]$ (positivity)
4. $B_i^n(t) = t \cdot B_{i-1}^{n-1}(t) + (1-t) \cdot B_i^{n-1}(t)$ (recursion)
5. $B_i^n(t) = B_{n-i}^n(1-t)$ (symmetry)
6. $B_i^n(t)$ has a maximum in $[0, 1]$ at $t = \frac{i}{n}$

A polynomial curve

$$\mathbf{P}_n(t) = \sum_{i=0}^n \binom{n}{i} (1-t)^{n-i} t^i \mathbf{p}_i$$

is called a *Bézier curve* of degree n . The points \mathbf{p}_i are called *control points* or *Bézier points*, the polygon formed by the control points is called the *control polygon*.

3.2.2 The de Casteljau Algorithm

For the evaluation of the points of the curve $\mathbf{P}_n(t)$, we avoid calculating $\binom{n}{i}$ because it is not numerically stable. Instead, we use a method for evaluating Bézier curves by the de Casteljau algorithm.

Given: control points $\mathbf{p}_0, \dots, \mathbf{p}_n$ of a Bezier curve and $t \in \mathbb{R}$, set

$$\mathbf{p}_i^r(t) = (1-t) \mathbf{p}_i^{r-1}(t) + t \mathbf{p}_{i+1}^{r-1}(t) \quad \begin{cases} r = 1, \dots, n \\ i = 0, \dots, n-r \end{cases}$$

$$\mathbf{p}_i^0(t) = \mathbf{p}_i.$$

then: $\mathbf{p}_0^n(t)$ is the point with parameter value t on the Bézier curve \mathbf{P}_n .

The polygon \mathbf{P} formed by $\mathbf{p}_0, \dots, \mathbf{p}_n$ is called the *Bézier polygon* or *control polygon* of the curve \mathbf{P}_n . Figure 12 illustrates the cubic case. The point \mathbf{p}_0^3 is obtained from repeated linear interpolation. The cubic case $n = 3$ is shown for $t = 1/4$.

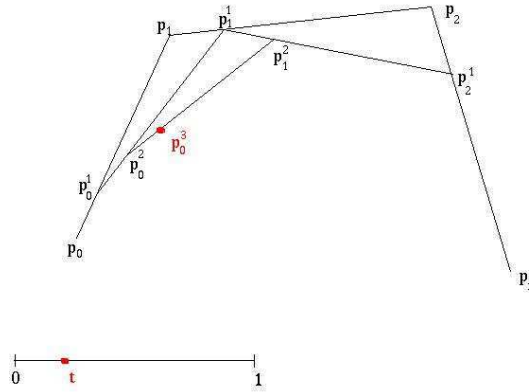


Figure 12: The de Casteljau algorithm

3.2.3 Properties of Bézier Curves

The de Casteljau algorithm allows us to infer several important properties of Bézier curves.

Affine invariance. Bézier curves are invariant under affine maps, which means that the following two procedures yield the same result: (1) first, compute the point at given t and then apply an affine map to it; (2) first, apply an affine map to the control polygon and then evaluate the mapped polygon at parameter value t . Affine invariance is a direct consequence of the de Casteljau algorithm because the algorithm is composed of a sequence of linear interpolations (or, equivalently, of a sequence of affine maps).

Convex hull property. For $t \in [0, 1]$, $\mathbf{P}_n(t)$ lies in the convex hull (see Fig. 13) of the control polygon. This follows since every intermediate \mathbf{p}_i^r is obtained as a convex barycentric combination of previous \mathbf{p}_j^{r-1} .

Endpoint interpolation. The Bézier curve passes through the points \mathbf{p}_0 and \mathbf{p}_n . We have $\mathbf{P}_n(0) = \mathbf{p}_0$ and $\mathbf{P}_n(1) = \mathbf{p}_n$.

Symmetry. It does not matter if the Bézier points are labeled $\mathbf{p}_0, \mathbf{p}_1, \dots, \mathbf{p}_n$ or $\mathbf{p}_n, \mathbf{p}_{n-1}, \dots, \mathbf{p}_0$. The curves that correspond to the two different orderings look the same. Written as formula:

$$\sum_{j=0}^n \mathbf{p}_j B_j^n(t) = \sum_{j=0}^n \mathbf{p}_{n-j} B_j^n(1-t)$$

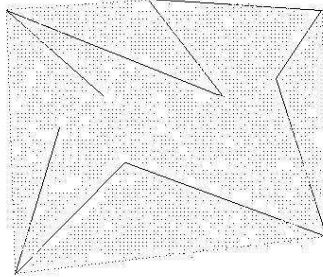


Figure 13: Convex hull: a polygon and its convex hull, shown shaded

It follows from the symmetry of Bernstein polynomials.

Derivatives. The derivative of a Bézier curve is another Bézier curve, obtained by differencing the original control polygon. Written as a formula:

$$\frac{d^r}{dt^r} \mathbf{P}_n(t) = \frac{n!}{(n-r)!} \sum_{j=0}^{n-r} \Delta^r \mathbf{p}_j B_j^{n-r}(t).$$

where

$$\begin{aligned} \Delta^r \mathbf{p}_j &= \Delta^{r-1} \mathbf{p}_{j+1} - \Delta^{r-1} \mathbf{p}_j \\ \Delta \mathbf{p}_j &= \mathbf{p}_{j+1} - \mathbf{p}_j \end{aligned}$$

is the iterated forward difference operator. In particular, the arc begins at \mathbf{p}_0 (and terminates at \mathbf{p}_n), admits $\mathbf{p}_0\mathbf{p}_1$ (resp. $\mathbf{p}_{n-1}\mathbf{p}_n$) as tangent at $t = 0$ (resp. $t = 1$); similarly, the curvature can be controlled by \mathbf{p}_2 at the origin, and by \mathbf{p}_{n-2} at the endpoint.

Integrals. The integral of a Bézier curve is another Bézier curve.

Degree elevation. Degree elevation increase the degree of a curve without changing the shape of the curve. Given a Bézier curve of degree n , based on $n + 1$ control points \mathbf{p}_k ($k = 0, 1, \dots, n$), the new set of $n + 2$ control points \mathbf{p}'_k ($k = 0, 1, \dots, n + 1$) given by

$$\begin{aligned} \mathbf{p}'_0 &= \mathbf{p}_0, \\ \mathbf{p}'_k &= \frac{k}{n+1} \mathbf{p}_{k-1} + \left(1 - \frac{k}{n+1}\right) \mathbf{p}_k, \quad 1 \leq k \leq n, \\ \mathbf{p}'_{n+1} &= \mathbf{p}_n, \end{aligned}$$

defines the same geometrical curve, now viewed as a Bézier curve of degree $n + 1$ (see Fig. 14).

A Bézier curve admits infinitely many representations of different degrees. Repeating the degree elevation process will produce convex control polygon with larger and larger number of points, and, at the limit, the control polygon will converge to the curve. By degree elevation, the distribution of the Bézier parameters t over the curve does not change, i.e. $\mathbf{P}_n(t) = \mathbf{P}_{n+1}(t)$.

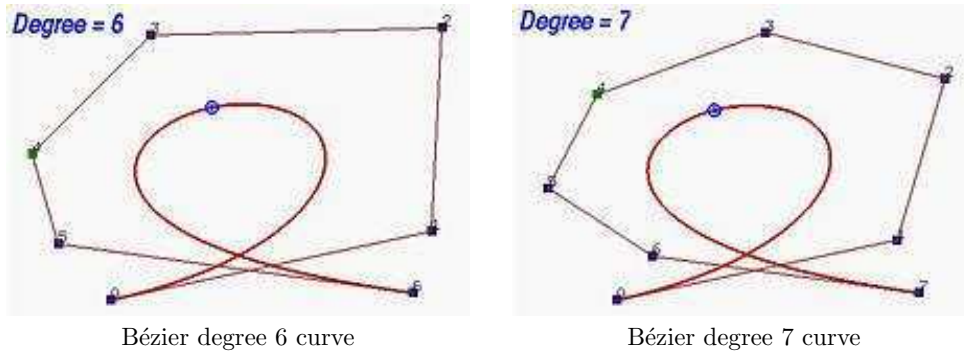


Figure 14: Degree elevation

3.2.4 Bézier patches and volumes

The Bézier patch is the surface extension of the Bézier curve.

A way to build a surface is to sweep a curve through space such that its control points move along some curves. The control points of these control curves describe the surface (see Fig. 15). The surface representation by these control points has properties analogous to those of a univariate curve representation. Similarly, one can build multidimensional volumes by sweeping a surface or volume through space such that its control points move along curves. Whereas a Bézier curve of degree n is a function of one variable (Bézier parameter) and takes a sequence of $(n + 1)$ control points, the patch is a function of two variables with an array of control points.

The patch is constructed from an $(n + 1) \times (m + 1)$ array of control points

$$\{\mathbf{p}_{i,j} : 0 \leq i \leq n, 0 \leq j \leq m\} \quad ,$$

and the resulting surface, which is now parameterized by two variables, is given by the equation

$$\mathbf{P}(s, t) = \sum_{i=0}^m \sum_{j=0}^n B_i^m(s) B_j^n(t) \mathbf{p}_{i,j}.$$

Similarly, a Bézier volume can be defined as follows:

$$\mathbf{P}(s, t, u) = \sum_{i=0}^l \sum_{j=0}^m \sum_{k=0}^n B_i^l(s) B_j^m(t) B_k^n(u) \mathbf{p}_{i,j,k} \quad ,$$

with a cube of $(l + 1) \times (m + 1) \times (n + 1)$ control points.

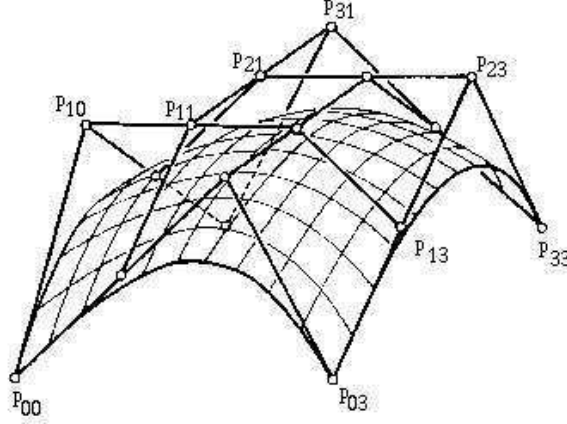


Figure 15: Bézier surface of degree (3,3) and its Bézier control net

3.3 Mesh Deformation

During the shape-optimization process, parts of the mesh boundary are being changed (displaced and deformed), and the 3D computational mesh must follow the deformed surface. Therefore, we have to develop a robust algorithm, which would move the computational mesh for the largest skin-deformations possible, and would give an acceptable volumic mesh for the CFD calculations. The mesh moving techniques have to be of a reasonable CPU complexity, because the mesh update has to take place, theoretically, each time a new shape is explored.

In the literature [32], one might choose from:

- *explicit deformation*: we prescribe the deformation to apply to each mesh node (Marocco [31]), knowing the shape skin deformation; the deformation for a node is proportional to its distance to the shape. We can write, for an internal node i :

$$\begin{cases} (\delta x_m)_i &= \frac{1}{\alpha_i} \sum_{k \in \Gamma_w} w_k \alpha_{ki} \delta \tilde{x}_i \\ \delta \tilde{x}_m &= \delta \tilde{x} \quad \text{on} \quad \Gamma_w \end{cases}$$

where δx_m is the sought variation of the mesh nodes, w_k is a weight for the contribution of each of the nodes k of the shape which depends on the length of the neighboring segments, $\alpha_{ki} = \frac{1}{|\tilde{x}_k - \tilde{x}_i|^\beta}$ with β a positive arbitrary parameter, $\alpha_i = \sum_{k \in \Gamma_w} w_k \alpha_{ki}$ is a

normalization parameter and Γ_w is the moving shape with a prescribed displacement $\delta \tilde{x}_m$. This algorithm is quite robust but expensive. The complexity is proportional to the number of the shape nodes times the number of mesh nodes.

- *elliptic smoothing*: we can solve the following elliptic system:

$$\begin{cases} (I - \eta\Delta)\delta x_m &= \bar{\delta\tilde{x}} \\ \bar{\delta\tilde{x}} &= \delta\tilde{x} \quad \text{on} \quad \Gamma_w \\ \bar{\delta\tilde{x}} &= 0 \quad \text{in} \quad D, \end{cases}$$

where δx_m is the mesh variation, η the viscosity coefficient in the mesh deformation process, taken proportional to local element size, Γ_w is the moving shape with displacement $\delta\tilde{x}_m$ and D internal nodes of the mesh. This algorithm is quite cheap but not very robust, and it does not keep the conformity of the element for fine meshes.

- *linear and torsional springs* : the existing fluid grid can be seen as a continuous or discrete pseudo-structural system with fictitious mass, damping and stiffness properties (Farhat [6]-[7]). A quasi-static version of the equation of the dynamic equilibrium for the system can be written as:

$$\begin{cases} \mathbf{K}\mathbf{q} &= \mathbf{0} \\ \mathbf{q} &= \bar{\mathbf{q}} \quad \text{on} \quad \Gamma_m, \end{cases}$$

where \mathbf{K} is the stiffness matrix, \mathbf{q} is the displacement vector and $\bar{\mathbf{q}}$ denotes the prescribed or somehow determined displacement vector on the moving boundary Γ_m .

- *transpiration conditions*: for small shape deformations, without moving the mesh, we can represent the shape modification by deriving more complex boundary conditions called *transpiration conditions*. With known structural displacements and velocities, a simple modification to the nodal boundary conditions on existing grid is capable of altering the displacements and velocities used in the flow solver for the new shape. No modifications are made to the existing grid except for a slight boundary condition modification to nodes on a deformable surface.

In our work, we have focused on implementation and use of linear/torsional springs and transpiration condition.

3.3.1 Linear and torsional springs for unstructured meshes

Linear and torsional springs method is a common way to modify a mesh around moving boundaries (Farhat et al. [6]-[7]).

As already said, the existing fluid grid can be seen as a continuous or discrete pseudo-structural system with fictitious mass, damping and stiffness properties. The system can be described using the equations of dynamic equilibrium. Most work on dynamic meshes has focused on the quasi-static version of this equation, which can be written in this way:

$$\mathbf{K}\mathbf{q} = \mathbf{0} \tag{24}$$

$$\mathbf{q} = \bar{\mathbf{q}} \quad \text{on} \quad \Gamma_m, \tag{25}$$

where \mathbf{K} is the stiffness matrix, \mathbf{q} is the displacement vector and $\bar{\mathbf{q}}$ denotes the prescribed or somehow determined displacement vector on the moving boundary Γ_m .

The collection of the edges of the mesh can be assimilated with a network of linear springs. However, it has been shown in [6] that linear springs (even for a 2D mesh) are not sufficient to prevent elements collapsing to inadmissible computational mesh. Therefore, one introduces, complementary to linear springs, a system of torsional springs, between each 2 edges leading from the same node (see Fig. 16 - 2D case).

The linear stiffness coefficient of the spring between the generic nodes i and j is chosen to be inversely proportional to the length l_{ij} of the supporting edge

$$k_{ij} = \frac{1}{l_{ij}} \quad ,$$

and the torsional stiffness coefficient is given by

$$C_i^{ijk} = \frac{1}{\sin^2 \theta_i^{ijk}} = \frac{l_{ij}^2 l_{ik}^2}{4A_{ijk}^2} \quad .$$

While the linear spring prevents the vertex collision along the edge (ij) , the torsional spring controls the angle at vertex i and consequently the area of the triangle. After a rigorous kinematics analysis [6], it is possible to superpose the effect of the linear and torsional springs to get a global stiffness matrix \mathbf{K} . If we apply a deformation to the mesh boundaries, the new mesh is the position of equilibrium of the new pseudo-structural system. The displacement of the nodes is the solution of the linear system (24).

This method, originally devised for 2D only [6], has been generalized for 3D [7] in the following way. Let T^{pqrs} denote a tetrahedron (as in Fig. 16 - 3D case). To prevent the collision of vertex s with face pqr , we propose to insert a triangle τ^{sjq} inside the tetrahedron T^{pqrs} . The best anti-collision effect might be attained if the triangle τ^{sjq} is in a plane perpendicular to the face pqr (see Fig. 16). Indeed, if the tetrahedron volume tends to zero due to the vertex s colliding with the face pqr , the area of sjq tends to zero. Hence, controlling the area of τ^{sjq} by torsional springs prevents vertex s from penetrating face pqr . The transfer of the elastic forces that are associated with torsional springs from the triangle τ^{sjq} to the tetrahedron T^{pqrs} is discussed in [7].

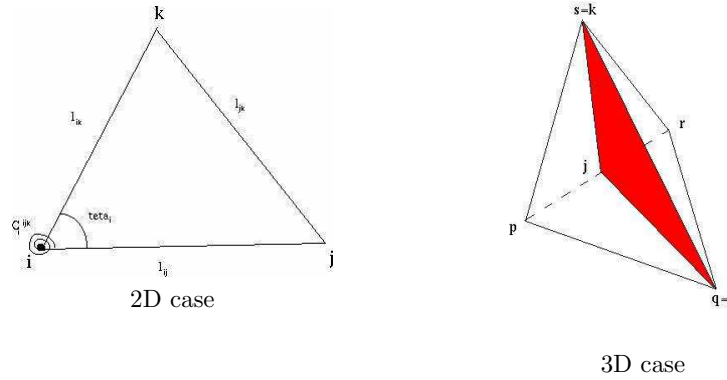


Figure 16: Torsional springs elements

Experiments This method, for the 2D case, is robust for general unstructured meshes and for quite large deformations (see Fig. 17). Some results of the 3D case can be seen in Fig. 18 - 19, from our experience the 3D variant is much less robust than the 2D one.

The springs method uses a linearized pseudo-elasticity model, therefore only small deformation are treated. In terms of CPU time, the torsional spring method is quite expensive. In the 3D, case for example, after the computation of the local stiffness matrix for one tetrahedron, we have to iterate for all the tetrahedra in the mesh and, at the end, to solve a linear system.

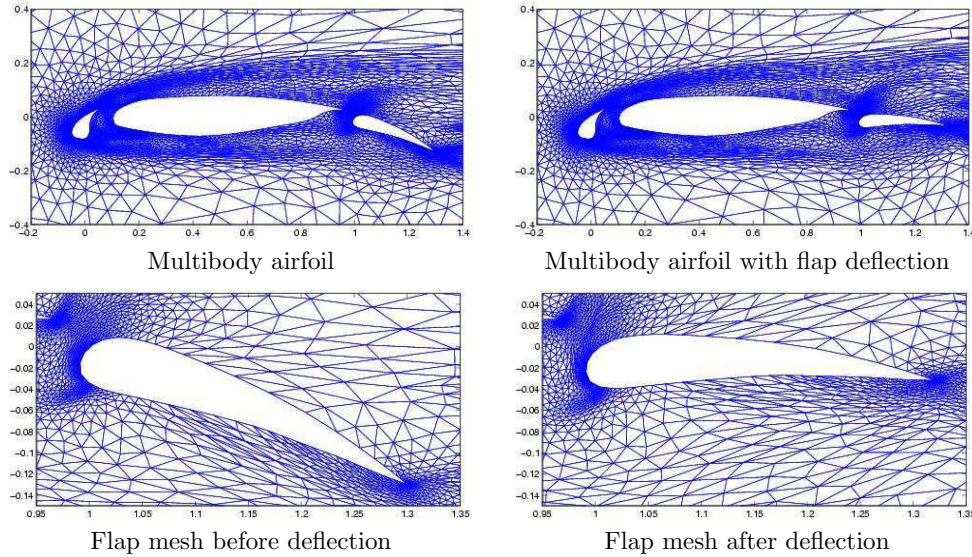


Figure 17: Example of 2D springs method for unstructured meshes

3.3.2 Transpiration Condition

Transpiration can trace its origins to 1950's in [25]. This paper describes the method of equivalent sources for modeling the influence of the boundary layer on the inviscid flow outside them. Rather than thickening an actual airfoil, the boundary layer effect could be accounted for by an equivalent surface distribution of sources.

Simplicity, speed and accuracy are the greatest advantages of the transpiration concept.

The idea is simple. With known structural displacements and velocities, a simple modification to the nodal boundary conditions on the existing grid is capable of altering the displacements and velocities used in the flow solver. No modifications are made to the existing grid except for a slight boundary condition modification to nodes on a deformable surface.

When we have a deformation of the surface, we have also a change in orientation of the normal (see Fig. 20(a)). Transpiration assumes that there is no significant stretching or volumetric change within the element so that the area of each element remains constant. Assuming that a normal has an x, y and z components, a change in orientation is accomplished by changing the velocity boundary condition on the affected nodes. This change in boundary conditions comes in the form of an additional fluid velocity outside the existing surface elements (see Fig. 20(b)).

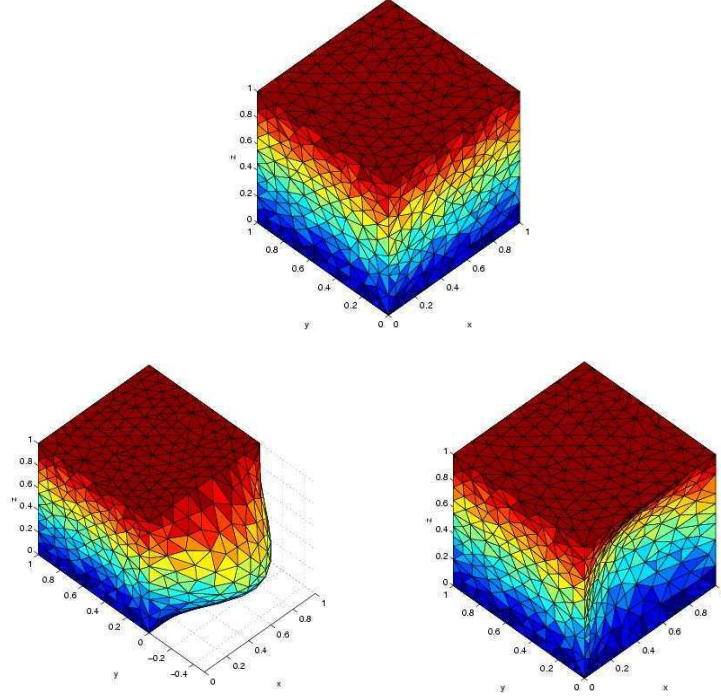


Figure 18: Cube and Deformed Cube

Let us denote by *shell* the shape to be emulated by transpiration and by \vec{n}_{shell} the normal of the shell. The slip boundary term of the flux $\Psi(W)$ is defined as follows:

$$\Psi(W)_{slipboundary} = qW + \begin{pmatrix} 0 \\ p(W)n_x \\ p(W)n_y \\ p(W)n_z \\ p(W)q \end{pmatrix}$$

with:

$$q = \vec{V} \cdot (\vec{n} - \vec{n}_{shell}),$$

where \vec{V} is the velocity of the fluid. In summary, each surface element that has undergone a change in orientation acts as a source sheet. The strenght of the source is determined by the extent of the simulated deflection.

This approximation has proved accurate enough for rather large perturbations of the boundary and very robust. Its accuracy has been effectively demonstrated over time through work done in [9], [41].

With the transpiration method, there is no mapping from one coordinate system to another, no relative nodal displacements, no elementary volume changes, no changes of the computational domain, no need to iteratively solve for a new nodal boundary conditions, etc. In an environment where speed, without sacrificed accuracy, is of primary concern, transpiration method has shown itself as a viable tool.

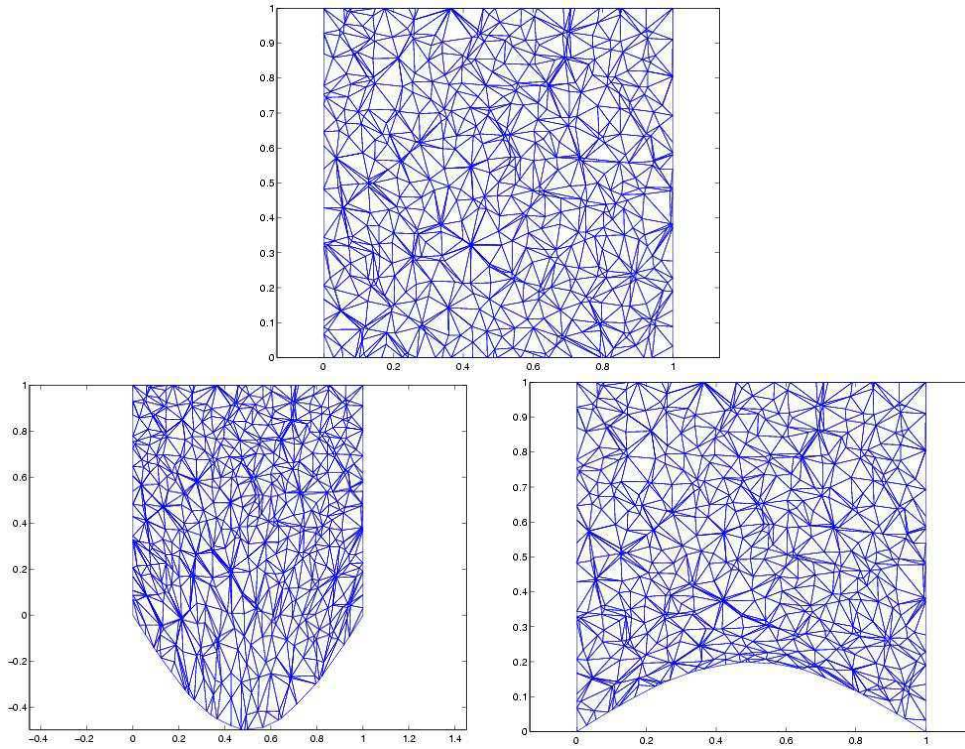
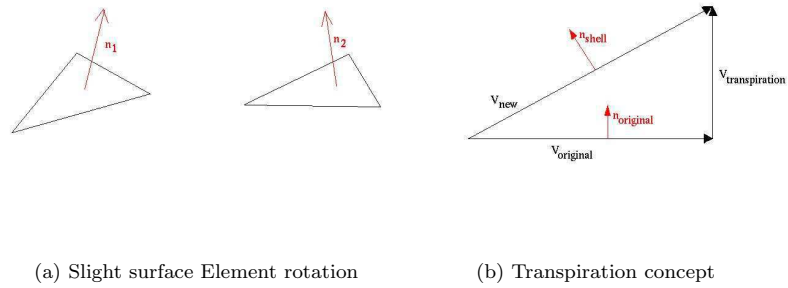


Figure 19: Section Z=0.5



(a) Slight surface Element rotation

(b) Transpiration concept

Figure 20: Transpiration

3.3.3 Conclusion

Without considering the transpiration method where we are not moving the mesh, none of the methods guarantee the conformity of the elements when the deformation is important.

In the present work, inspired by the approach used by N. Marco and A. Dervieux [27] and by Young et al. [14] and by the results obtained, we have chosen to represent the shape modification by applying a *transpiration condition*.

4 Genetic Algorithms

In *The Origin of Species* [3], Charles Darwin stated the theory of natural evolution. Over many generations, biological organisms evolve according to the principles of natural selection like “survival of the fittest” to reach some remarkable forms of accomplishment. In nature, individuals in a population have to compete with each other for vital resources. Because of such selection, poorly performing individuals have less chance to survive, and the most adapted, or “fit” individuals produce a relatively larger number of offsprings. After a few generations, species evolve spontaneously to become more and more adapted to their environment. In 1975, Holland developed this idea in *Adaptation in natural and artificial system*. By describing how to apply the principles of natural evolution to optimization problems, he laid down the first Genetic Algorithm. Holland’s theory has been further developed and now Genetic Algorithms (GAs) emerge as a powerful adaptive method to solve search and optimization problems. Some results can be seen in [28, 29, 30].

In Genetic Algorithms, we use the term *individual* to denote one configuration of the optimal shape. The feasibility of the shape is judged by a *fitness* function, reflecting the minimized cost functional and penalizing geometrically unfeasible individuals. The shape parameters of one individual are encoded in the individual’s *chromosome*. The Genetic Algorithm operates simultaneously on an entire population of individuals (shapes), the initial population being generated either randomly or as a set of feasible individuals using an a-priori engineering guess. The core of the Genetic Algorithm consists in selection, crossover and mutation operators, whose role is to mimic natural empiric laws of survival of the fittest (selection), their procreations (crossover) and occasional mutations. The generation operators are usually not deterministic, they implement their operators in the probabilistic sense, with a given probability distribution. The crossover is performed with a *crossover probability* p_{cross} (or *crossover rate*); two selected individuals (parents) exchange parts of their chromosome to create two offsprings. This operator tends to enable the evolutionary process to move towards “promising” regions of the search space. The mutation operator is introduced to prevent premature convergence to local optima by randomly sampling new points in the search space. It is carried out by flipping bits at random, with some (small) probability p_{mut} .

Genetic algorithms are *stochastic* iterative processes that are not guaranteed to converge. They have a great potential to explore the whole search space and identify multiple local maxima and to converge to the global optimum while a “point to point” method will generally stall in a local optimum only. They are found more robust in the case of non differentiable, multi-modal or non convex functions, and are particularly interesting for search of a trade-off optimum with respect to several criteria (Pareto front, Nash game).

4.1 Coding

To apply Genetic Algorithms to a specific problem, we must first define an appropriate representation for the solution. We must find a way to encode any solution of the problem into a chromosome of a certain structure. This structure shared by all the chromosomes is called the genetic representation. Solutions might be encoded into a string of bits of a given length. The advantage of bit-string chromosomes is their versatility and simplicity. Historically, GAs have

1. **Initial population** (random or heuristically)
2. **Coding** (binary, character-based, real-valued, etc.)
3. **Evaluation of population** (fitness function)
4. **Selection** (Roulette-wheel or Tournament)
5. **Crossover** (Uniform or N-point)
6. **Mutation**
7. **Update** (new generation → go to step 3)

Table 1: Genetic Algorithms

always tried to be a universal solver, able to deal with a wider range of problems. So, binary coding was seen as a standard representation that can fit almost all kinds of search space. Indeed, a string of bits can encode integers, real numbers, sets or whatever is appropriate for the optimized problem. Moreover, the genetic operators over the binary chromosomes are quite simple. Mutation and recombination of bit strings can be done with very simple and universal operators. However, bit strings are often not really appropriate for particular problems. A problem-specific representation, where integer genes represent integer parameters, real genes represent real parameters, character strings represent sets, and so on, can be customized in a way that gives more sense and coherence to the algorithm.

4.1.1 Binary coding

Let us focus on binary coding of real parameters in the chromosome. It can be viewed as a fixed-point representation of real-parameters. For every real parameter x_i , we give a range of variation and a coding-precision. The bit-length of the part of the binary chromosome reserved for encoding x_i , $x_i \in [l_i^{inf}, l_i^{sup}]$, with at least the given precision ϵ_i is then calculated as the smallest integer $nbit_i$ such that

$$2^{nbit_i} - 1 \geq \frac{(l_i^{sup} - l_i^{inf})}{\epsilon_i}.$$

The chromosome is the set of all the genes describing the variables of one individual, the total number of bit for one individual is then

$$nbit = \sum_{i=1}^n nbit_i.$$

The decoding of the chromosome is done by the formula:

$$x_i = l_i^{inf} + \frac{l_i^{sup} - l_i^{inf}}{2^{nbit_i} - 1} \sum_{i_{bit}=1}^{nbit_i} 2^{i_{bit}-1} Ch(i_{bit}),$$

where $Ch(i_{bit})$ is the binary value (0 or 1) of the gene i_{bit} associated with the variable x_i . For example, for a chromosome with two real parameters

- parameter 1: $l_1^{inf} = 1.1$, $l_1^{sup} = 3.1$, $\epsilon = 1 \rightarrow nbit_1 = 2$,
- parameter 2: $l_1^{inf} = -8.0$, $l_1^{sup} = -1.0$, $\epsilon = 1 \rightarrow nbit_2 = 3$,

the length of the chromosome is $nbit = 5$.

Inversely, if we have, for example, the chromosome [11011], the decoded real value parameters x_1 and x_2 are as follows:

$$\begin{aligned} x_1 &= 1 + \frac{2}{3}(2^0 \cdot 1 + 2^1 \cdot 1) = 3.0 \\ x_2 &= -8 + \frac{7}{7}(2^0 \cdot 0 + 2^1 \cdot 1 + 2^2 \cdot 1) = -2.0 \end{aligned}$$

4.2 Fitness function

Once the genetic representation has been defined, the next step is to associate to each solution (chromosome) a value corresponding to the fitness function. There is generally no problem in determining the fitness function. Particular attention should be taken due to the fact the selection is done according to the fitness of individuals.

In the case of multicriteria optimisation, the fitness function is definitely more difficult to determine. There is often a dilemma as how to determine if one solution is better than another. The trouble comes more from the definition of a 'better' solution rather than from how to implement a GA to resolve it. For more advanced problems, it may be useful to consider something like Pareto optimality or other ideas from multicriteria optimisation theory.

The constraints in Genetic Algorithms are introduced mostly by penalization and usually the feasibility region is rapidly detected by Genetic Algorithm process. The penalty method allows constraints to be violated, depending on the magnitude of the violation. However, a penalty that is proportional to the degree of infeasibility is incurred which degrades the objective function. If the penalty is large enough, highly infeasible individuals will rarely be selected for reproduction, and the GA will concentrate on feasible or nearly-feasible solutions.

In the case of wing optimization if we are interested only in drag reduction but we want to keep lift, one possible fitness function, with a penalty on lift-preservation, is

$$J = \frac{C_D}{C_{D_0}} + 10^4 \cdot \max\left(0, 0.999 - \frac{C_L}{C_{L_0}}\right),$$

where the subscript 0 is referring to the original wing. In this case, 0.1% or more loss in lift will increase the fitness function by more than 10, while lift increasing is not penalized at all.

4.3 Selection

The selection operator is designed to implement the law of the survival of the fittest. Like everywhere in the genetic algorithm, two aspects are to be considered: the convergence of the genetic algorithm towards some solution and the variety (diversity) of the genetic material influencing the exploratory potential for new solutions. Usually, these two aspects act in contradiction. Following this remark, the design of a good selection operator must introduce an algorithm which would handicap bad individuals but would not spoil the variety of the genetic material by choosing systematically only the best individuals to be *parents* for a new generation.

individual	fitness value	probability	percentage
1	169	0.144	14.4%
2	576	0.492	49.2%
3	64	0.055	5.5%
4	361	0.309	30.9%

shoot	result	selection
1	35.4	2
2	87.9	4
3	56.7	2
4	12.7	1

Table 2: Example of the roulette-wheel selection

Typically we can distinguish two types of selection schemes, *proportionate* selection and *ordinal-based* selection. Proportionate-based selection picks out individuals based upon their fitness values relative to the fitness of the other individuals in the population. Ordinal based selection schemes select individuals not upon their raw fitness, but upon their relative ordering (ranking) within the population.

4.3.1 Roulette-wheel

Roulette-wheel selection is the classic and popular fitness-proportionate selection. It simply assigns to each solution a sector of a roulette wheel whose size (the angle it subtends) is proportional to the appropriate fitness measure (usually a scaled fitness of some sort). Then it chooses a random position on the wheel (and the solution to which that position was assigned, as if spinning the wheel). In order to create a new population of parents, the weighted roulette-wheel is spun n times, where n is the population size (see Table 2 and Fig. 21).

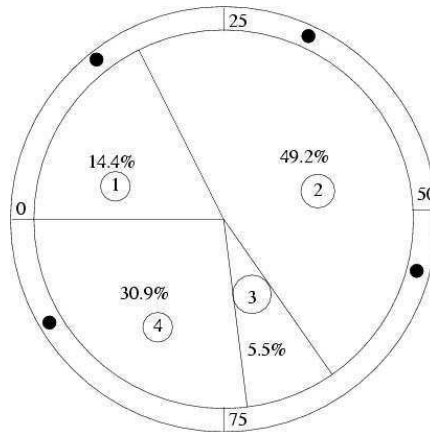


Figure 21: Roulette-wheel selection

4.3.2 Tournament

Tournament selection is an ordinal-based scheme, robust and relatively simple. Many variations exist, but the basic mechanism is to pick k members of the population at random and then select one of them in some very simple manner that depends on fitness. Choosing the best members of the tournament produces a relatively strong selection pressure. So, generally the best is chosen with the probability p , if it fails to be chosen, the second best is chosen with the probability p , and so on until the final solution is chosen. The selection pressure can be adjusted by changing k and p . Clearly tournament selection as described is unaffected by the absolute fitness values, and in effect depends only on the rank of any solution in the population.

4.4 Crossover

It is the process of taking two parent solutions and producing from them a child. There are many different reproducing operators. The most common is an N-point crossover. The N-point crossover takes two chromosomes, aligns them and divides them by N cuts into N+1 segments. A child is produced by choosing alternatively a segment from one or the other parent. Two different children can be produced depending if the first segment is taken from the mother or from the father. An example of 1-point crossover is shown in Fig. 22.

Uniform crossover is quite different from the N-point crossover. Each gene (bit) in the offspring is created by copying the corresponding gene from one or the other parent, chosen according to a randomly generated binary crossover mask of the same length as the chromosomes. Where there is a 1 in the crossover mask, the gene is copied from the first parent, and where there is a 0 in the mask the gene is copied from the second parent (see Fig. 23). A new crossover mask is randomly generated for each pair of parents. Offsprings therefore contain a mixture of genes from each parent.

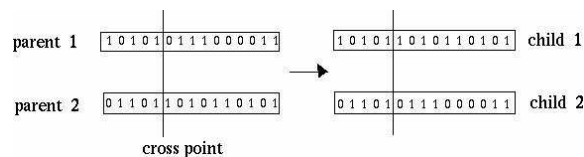


Figure 22: 1-point crossover

4.5 Mutation

Mutation is a simple operator consisting of random changes in the value of genes in a chromosome. Mutation has traditionally been considered as a simple search operator. If crossover is supposed to exploit the current solutions to find better ones, mutation is supposed to help for the exploration of the whole search space. Mutation is often seen as a background operator to maintain genetic diversity in the population. There are many different forms of mutation for

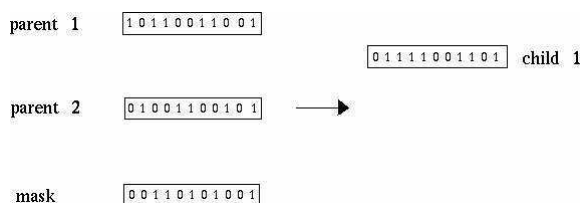


Figure 23: Uniform crossover

the different kinds of chromosome coding schemes. For binary coding, a simple mutation can consist in inverting the value of each gene with a small probability.

4.6 Parameters of configuration

Let us summarize what kind of information one should input to Genetic Algorithms:

- *coding*: range of variation $[\min, \max]$ and coding-precision ϵ
- choice of genetic operators *selection*, *crossover*, *mutation*
- probabilities for stochastic genetic operators
- population size and stopping condition

In Chapter 6 we will use the following notations for Genetic Algorithms tests:

popsiz: the size of the population

maxgen: maximum number of generations

pcross: percentage of crossover

pmutat: percentage of mutation

selecttype: type of selection (tournament or roulette-wheel)

crossstype: type of crossover (N-point, uniform, etc.)

4.7 Conclusion

Since about fifteen years ago, Genetic Algorithms have been introduced in aerodynamics shape design problems (see [19],[37], [40],[35]).

The main concern related to the use of genetic algorithms is the computational effort needed for the accurate evaluation of a configuration that might lead to unacceptable computer time if compared with more classical algorithms. Eventhough, they can be effectively parallelized, the CPU cost related to evaluation of the whole population is quite high.

A review of the basic structure of a Genetic Algorithm is:

1. initialize randomly a population of individuals
2. evaluate the individuals following their fitness (cost functional) value
3. apply genetic operators (selection, crossover and mutation) to the population
4. re-run from point 2 until the convergence is reached.

4.8 Validation of GAs on an analytic function

Let us consider in this section a global minimization problem of an analytical objective function F , known as the Rastrigin function:

$$F(\vec{x}) = A \cdot n + \sum_{i=1}^n x_i^2 - A \cdot \cos(\omega \cdot x_i)$$

$$A = 10 ; \omega = 2 \cdot \pi ; x_i \in [-5.12, 5.12]$$

The *Rastrigin Function* is a typical example of non-linear multimodal function. This function was first proposed by Rastrigin as a 2-dimensional function [47] and has been generalized by Mühlhenbein et al. in [33] to \mathbb{R}^n . This function is a fairly difficult problem due to its large search space and its large number of local minima. The surface of the function is determined by the external variables A and ω , which control the amplitude and frequency modulation, respectively.

The optimum solution of the problem is the vector $\vec{x} = (0, \dots, 0)$ with the function value $F(\vec{x}) = 0$.

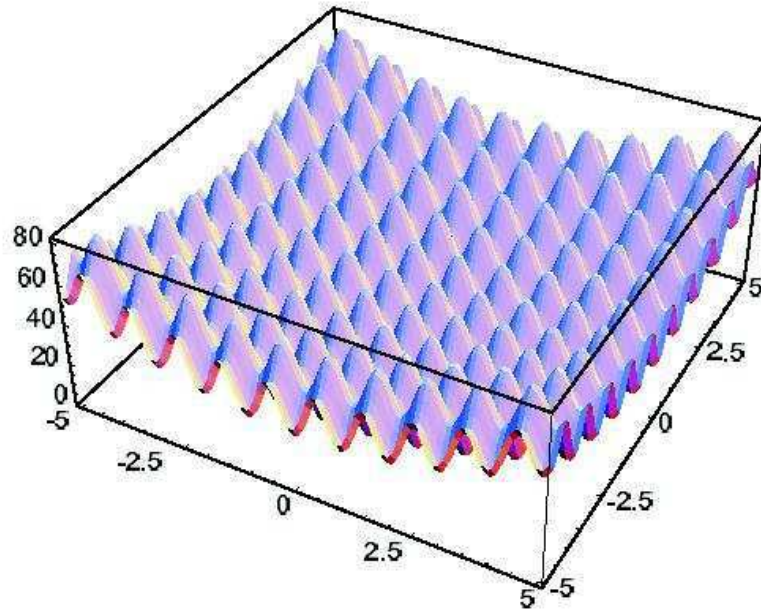


Figure 24: Rastrigin Function

Let us validate our genetic algorithm in this type of problem. The common parameters for our Genetic Algorithm are:

- *maxgen*: 300
- *pcross*: 0.85
- *pmutat*: 0.005
- *selecttype*: roulette-wheel
- *crosstype*: 2-points

In Fig. 25 we can see the convergence history choosing an high *popsize* value (100).

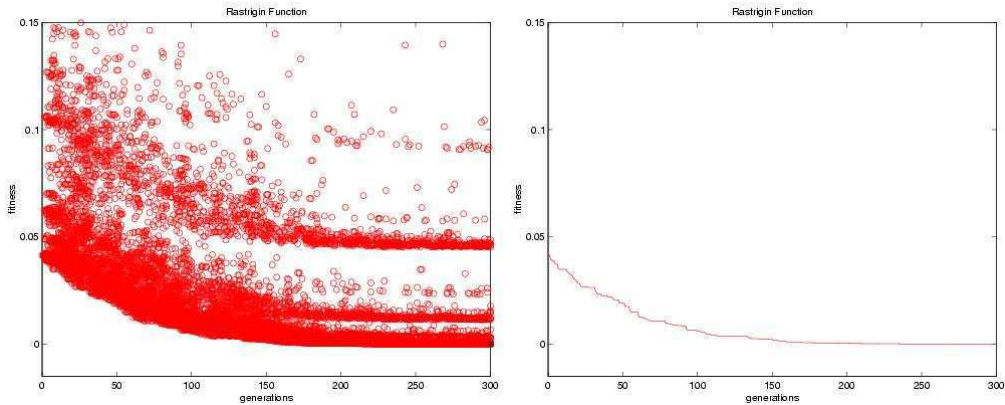


Figure 25: Convergence history (*popsize* = 100)

Genetic Algorithms are able to find the optimum solution in few generations and we can see in Fig. 25 that there is also an agglomeration of individuals in the local minima values. We see from Fig. 25, that we have roughly attained the global minimum $F(\vec{x}) = 0$ after 150 generations, the next 150 generations were needed to improve the precisions of our guess. Also, we remark that the genetic algorithm was able to identify more than one converged state corresponding to local minima (the clusters of fitness values).

We shall note for our future CPU-complexity considerations that minimum has been achieved after 300×100 function evaluations. Most of the optimization algorithms are not able to find global minimum. Genetic algorithms are more powerful in this respect, although they are quite time-consuming.

5 Derivative-Free Optimization Algorithms

A class of optimization algorithms working without the knowledge of cost-function derivatives is called the *derivative – free optimization* algorithms. One of the representatives of such algorithms are the *direct search methods* [39], [23]. Among the direct search methods we count, for example,

- *pattern search methods*,
- *simplex methods*,

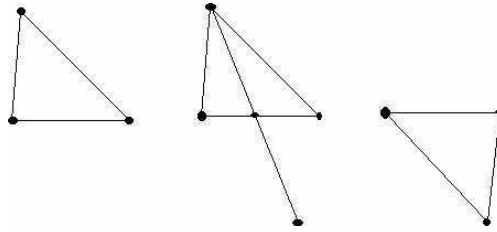


Figure 26: Original simplex, reflection and the resulting simplex

- *methods with adaptive sets of search direction.*

Although these methods have been developed heuristically and no proof of convergence have been derived for them, in practice they have generally proved to be robust, fast and reliable. While they do not assure finding global minimum, they only rarely fail to locate at least a local minimum of the cost-function. In our work, we have focused on implementation and use of a simplex method.

The simplex methods are characterized by the simple device that they use to guide the search for minimum - a non-degenerate simplex in \mathbb{R}^n . A simplex is a set of $n + 1$ points in \mathbb{R}^n and a non-degenerate simplex is one for which the set of edges adjacent to any vertex forms a basis for the space. For the minimization of a function of n variables, the search depends on the comparison of function-values in $n + 1$ vertices of the simplex.

5.1 Spendley, Hext and Himsworth simplex method

The basic idea of simplex search, due to Spendley, Hext and Himsworth [45], is the attempt to reflect bad simplex vertices through a hyper-plane specified by the resting vertices. Importantly, this operation of evolving towards parameter-values with low cost-function value does not degenerate the simplex (see Fig. 26).

Starting from this consideration, we can see how this method works. After the identification of the worst vertex in the simplex (the one with the least desirable cost value), there is a reflection of this worst through the centroid of the opposite face. If the reflected vertex is still the worst vertex, then we choose the "next worst" vertex and we repeat the process. When the method is near to the minimum, there is a circling sequence of simplices. For example, in Fig. 27, after five reflections the search is back where it started, without replacing x_i , which means that x_i is in the neighborhood of a minimum point. When this situation has been detected, the authors suggested two alternatives: either reduce the lengths of the edges adjacent to the minimum vertex and resume the search, or resort to a higher-order method to obtain faster local convergence [23].

5.2 Nelder and Mead simplex method

The modification of the simplex algorithm of Spendley proposed by Nelder and Mead [34] has additional moves designed to accelerate the search. They have proposed to supplement the basic reflection move with additional options to deform the simplex in a way that they suggested would better adapt to the features of the objective function. For this purpose, they added expansion and contraction moves.

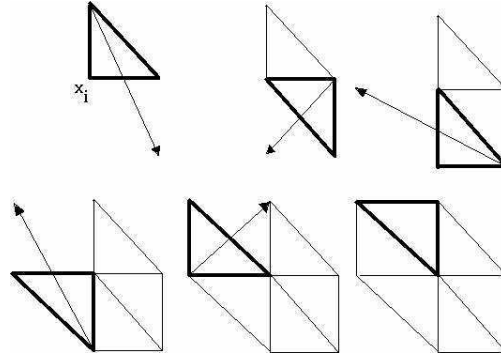


Figure 27: Behaviour near a minimum

5.2.1 Reflection

At the generic iteration k , the reflection of the vertex $x_j^k \in \mathbb{R}^n$ is denoted by x_r^k (see Fig. 28) and its coordinates are defined by the relation

$$x_r^k = (1 + \alpha)\bar{x}^k - \alpha x_j^k \quad ,$$

where α is a positive constant, called the *reflection* coefficient, generally fixed to 1, and \bar{x}^k is the centroid of the points. After this, there are some possibilities:

- x_r^k is the best among the other points \Rightarrow expansion move ,
- x_r^k is still the worst value \Rightarrow contraction move ,
- otherwise x_r^k is taken like a new value of x_j^k and a new iteration is done.

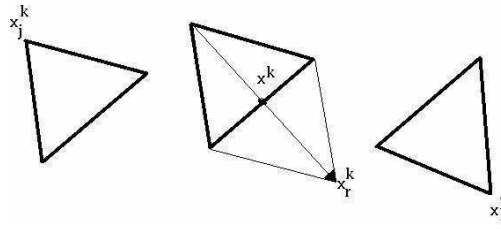


Figure 28: Reflection move

5.2.2 Expansion

If the reflection has produced a new best value, we expand x_r^k to x_e^k (see Fig. 29) by the relation

$$x_e^k = \gamma x_r^k + (1 - \gamma)\bar{x}^k \quad ,$$

where γ is called *expansion* coefficient; it is greater than 1 and usually it is the ratio of the distance $x_e^k \bar{x}^k$ to $x_r^k \bar{x}^k$. After this step, the possibilities are:

- x_e^k is better than $x_r^k \Rightarrow x_e^k$ is taken as new value for the next iteration ,
- x_e^k is worst than $x_r^k \Rightarrow x_r^k$ is taken as new value for the next iteration .

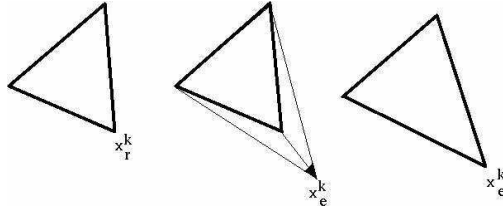


Figure 29: Expansion move

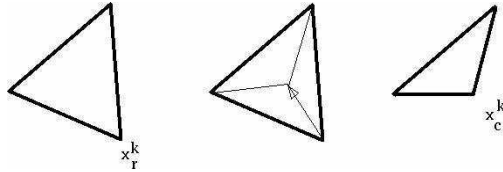
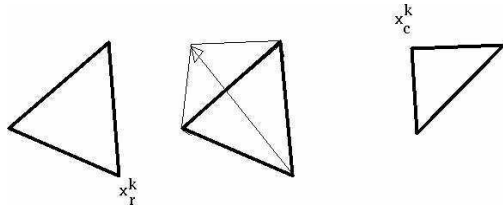
5.2.3 Contraction

If the reflection has always produced the worst cost-function value, the choice is to replace x_r^k with a new vertex position x_c^k using the relation

$$x_c^k = \beta x_r^k + (1 - \beta) \bar{x}^k, \quad \text{if } f(x_r^k) < f(x_j^k) \quad (\text{Fig. 30})$$

$$x_c^k = \beta x_j^k + (1 - \beta) \bar{x}^k, \quad \text{if } f(x_r^k) > f(x_j^k) \quad (\text{Fig. 31})$$

If x_c^k is a better value, it is replacing the vertex x_j^k in the next iteration. In the other case, the simplex is not good for the topology of the problem and a reduction move is necessary.

Figure 30: Contraction move, if $f(x_r^k) < f(x_j^k)$ Figure 31: Contraction move, if $f(x_r^k) > f(x_j^k)$

5.2.4 Reduction

All the points are replaced by

$$x_i^{k+1} = \frac{x_i^k + x_m^k}{2},$$

where x_m^k is the best value.

There are two possibilities:

- $f(x_r^k) > f(x_j^k) \Rightarrow$ the reduction is applied (see Fig. 32),
- $f(x_r^k) < f(x_j^k) \Rightarrow x_r^k$ replaces x_j^k (reflection) and then the reduction is applied (see Fig. 33).

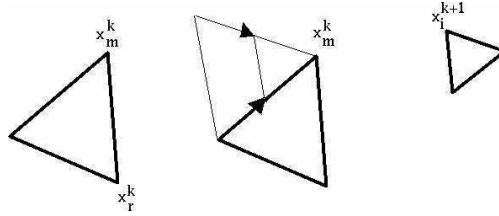


Figure 32: Reduction move, if $f(x_r^k) > f(x_j^k)$

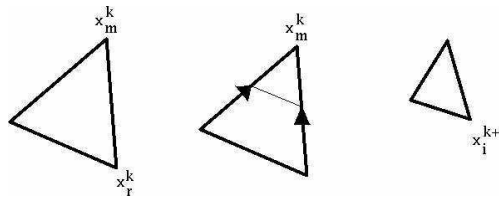


Figure 33: Reduction move, if $f(x_r^k) < f(x_j^k)$

5.3 Conclusion

The Nelder-Mead simplex algorithm is enjoying an enduring popularity. Of all the direct search methods, it is the one most often found in numerical software packages. However, this algorithm is not yet accepted by the mathematic community for lack of convergence demonstrations. Recently it has been proved [21] that the algorithm converges towards a stationary point in \mathbb{R}^1 .

6 Numerical Experiments

This chapter describes some results obtained with the optimization code. In particular, we consider optimization by genetic algorithms and by simplex method. At first, we are comparing the two approaches with respect to both the ability to find the globally best shape within the prescribed search-space, and their speed and CPU cost. Also, we conduct some comparative

studies of different set-ups of parameters of the respective methods. Most important is, nevertheless, the comparison of optimizations using the Bézier degree elevation idea in order to speedup the convergence.

In all tests, we are optimizing a 3D wing in transonic regime. In the following two sections we will describe our test-case, its geometry, discretization mesh, cost functional and imposed aerodynamic and geometric constraints.

6.1 Geometry of the test-case wing

The wing is a swept back wing. Starting from a given planform sketch in Fig. 34 (courtesy of Piaggio Aero Industries), we have chosen for our test-planform the dimensions shown in Fig. 35. The main chord at the root is 2911 mm, the sweep angle is 19.7° in the leading edge and 6.4° in the trailing edge, while the span length is 7540 mm. The root chord is 1057 mm.

To construct the 3D geometry, we have used a Bézier representation of a NACA0012 airfoil (see Fig. 39), which is a polynomial profile, with two Bézier curves of order 8 (extrado and intrado). The 3D wing is composed by 20 slices of NACA0012 profile placed equidistantly and scaled at different span-lengths (see Fig. 40).

The free-stream state regime is:

Mach number	0.83
Angle of flow incidence	2°

In all the tests, the minimized cost function (*fitness*) is:

$$J = \frac{C_D}{C_{D_0}} + 10^4 \cdot \max\left(0, 0.999 - \frac{C_L}{C_{L_0}}\right),$$

The 0 subscript is referring to the original wing. With this cost function, 0.1% or more loss in lift will increase the fitness function by more than 10, while lift-increasing is not penalized at all.

In Fig. 36 we can see the pressure and the Mach fields of the original wing. These results are obtained using the flow solver of Chapter 2.1, with a stopping criterion $\epsilon = 10^{-6}$ on non linear flow residual.

In the following figures, we plot the adimensional pressure computed as

$$p^* = \frac{p}{\rho_\infty \|\vec{U}_\infty\|^2},$$

where p is the local pressure, ρ_∞ the density and \vec{U}_∞ the velocity at infinity.

The Mach field is shown only for supersonic values of velocity. In a transonic optimization problem, we are interested to see if this region is reduced or not during the process. As we can see in Fig. 36, in a transonic regime, there is a shock wave over the extrado of the wing. In front of the shock wave, the fluid particles are in a supersonic regime, and behind in a subsonic one. The intensity of the wave is strictly correlated with the size of supersonic-regime zones but, at the same time, also with the intensity of the drag. It means that the shock wave and, in particular, the drag are reduced if we reduce the supersonic zones.

In all the results, we will take for comparison the C_L and C_D values of the original wing that we have obtained with a non linear flow residual 10^{-6} . We can see in Table 3 the difference in C_L and C_D between a well converged flow-solution (non linear flow residual 10^{-6}) and weakly converged flow solution (non linear flow residual 10^{-3}).

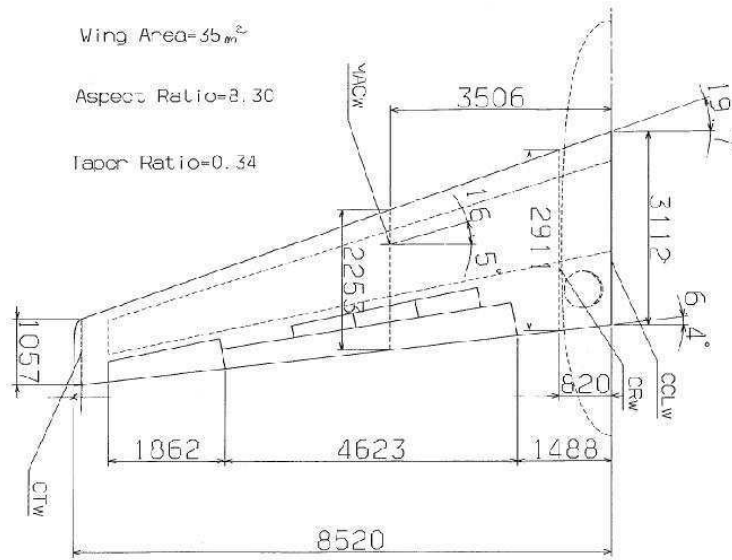


Figure 34: Geometry of the wing (courtesy of Piaggio Aero Industries)

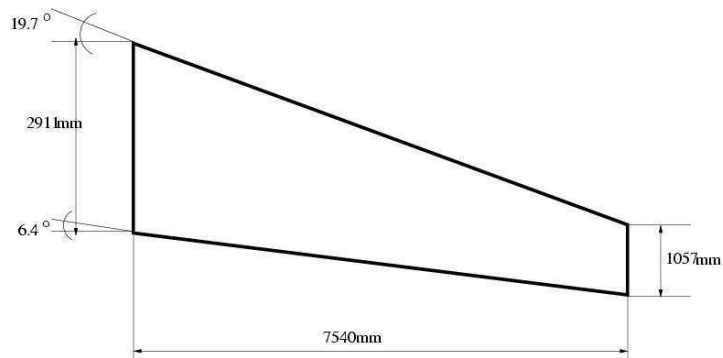


Figure 35: Planform Geometry

	10^{-3}	10^{-6}
C_L	0.3192006583	0.3192007875
C_D	0.0263540181	0.0263532471

Table 3: influence of non linear flow residual on the original solution

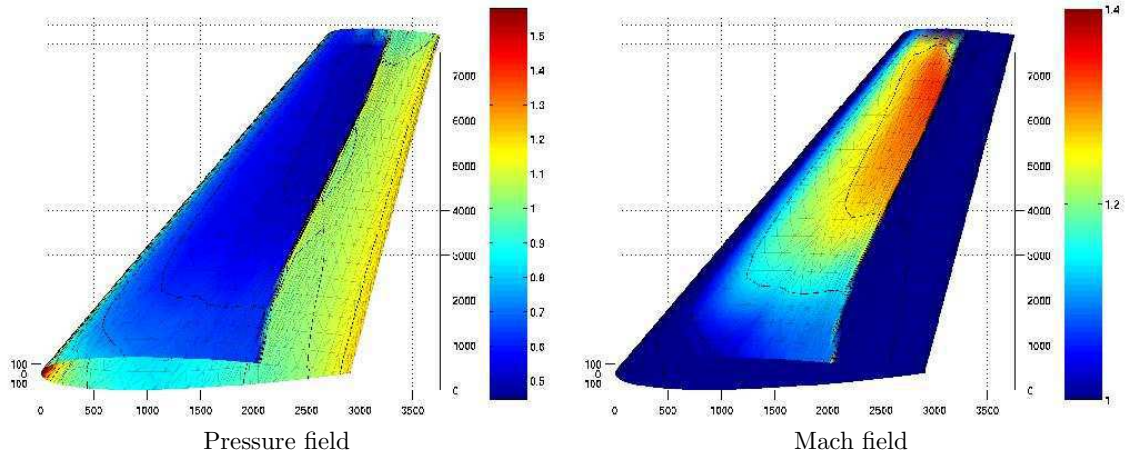


Figure 36: Original wing

As seen in Chapter 3, the 3D Bézier tensorial parameterization allows us to choose its degree in three directions x - y - z . Throughout this presentation, x -direction is placed along the chord, y -direction is thicknesswise and z -direction spanwise.

One of the geometric constraints we are to apply is the so-called *no-double curvature* requirement. This constraint coming from the manufacturing process translates into restricting all possible optimal wing shapes to those whose shape can be obtained by a linear interpolation of the root and tip sections along the spanwise direction. Hence, to satisfy this option, we choose a particular parametric box following the wing planform and set the degree of parameterization in z -direction to 1. We choose degree 1 also in the y direction (thickness). With these choices, we are moving only the control points along the x direction.

As already said in Chapter 3, we fix the four corners of the control box (see Fig. 38). This choice, and the degree 1 in y direction, allows us to keep fixed the leading and the trailing edge and the planform area.

Through this study, we compare parameterizations of degree 6, 7, 8, 9 along the x -direction (chord-wise), i.e. with 7, 8, 9, and 10 control points along the x -direction. Let us refer to different degree parameterizations by i - j - k , where i denotes the degree in x -direction, i.e. in our study $i=6,7,8,9$, j is the degree in y -direction and k in z -direction, i.e. for us $j=k=1$.

In Fig. 37 there is an example of parameterization of degree 6-1-1 (x - y - z direction).

6.2 Computational Mesh

Usually, grid generation methods may be classified into three categories, depending on the choice of topology and the type of elements used to construct the grid,:

1. unstructured grids;
2. structured grids;
3. hybrid grids.

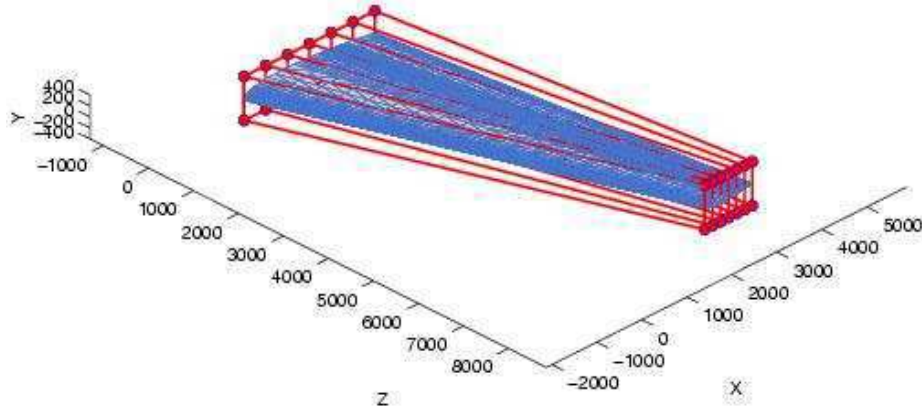


Figure 37: Bézier representation of degree 6-1-1

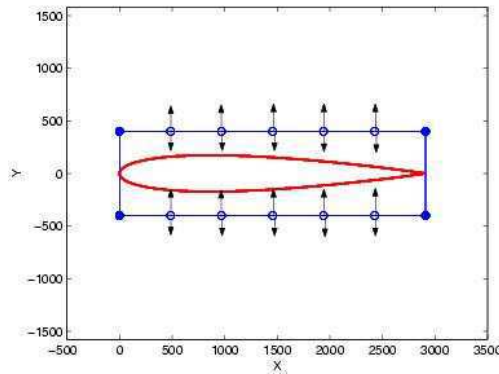


Figure 38: Root control point authorized displacements

These categories describe the layout of the physical cell and the neighbour relationship between cells in a given grid.

Unstructured grids are typically formed by simplices such as tetrahedra; these grids can be generated in most complex domains and mesh refinement can be done without difficulties. This grid is usually refined in sensible flow areas and coarsened in unimportant zones.

Structured grids are usually formed by hexahedra (eight nodes and six quadrilateral faces). Their rigid structure may favour the computation (for the spatial derivatives) and diminish the computational errors due to the discretization. They tend to propagate the refinements inside the mesh. To limit the fine grid propagation a multi-block grid is necessary. A multi-block grid is a collection of structured grids that together fill the domain.

Hybrid grids take advantage of both unstructured and structured methods by applying structured meshes near to the body and unstructured meshes in the outer boundaries.

Classical structured grid generation is well documented by Thompson in [46], for unstructured see George [10], [11].

As seen in section 2.1, our flow solver is based on unstructured grids. For the flow regime parameters, we need a 3D adapted mesh for transonic flow with a shock solved with Euler solver. For future developments, we prefer to have not only the 3D external mesh for the CFD calculations, but also a second, auxiliary interior mesh, needed for applying geometric constraints on wing volume, wing-box position, or relative change in local thickness. Considering a high CPU complexity of an optimization process, where several hundreds or thousands of flow-evaluations will be necessary, we are searching for the smallest mesh possible giving us still acceptable results.

With these consideration, and eager to test 2D and 3D mesh deformation techniques, we have created our mesh in this way:

- creation of a 2D transonic mesh of a RAE2822 airfoil (see Fig. 41): this is an adapted mesh for transonic flow solved with a 2D Euler solver at the same regime ($M = 0.83$, $\alpha = 2^\circ$); the number of nodes of the 2D mesh is 1004; the shock position is refined;
- substitution of a RAE airfoil in 2D with a NACA0012 airfoil using torsional springs method of Section 3.3.1 (see Fig. 42);
- generation of 20 slices of 2D NACA mesh along the span direction on a rectangular planform (see Fig. 43);
- generation of 11 slices of the tip section mesh from tip to far-field;
- creation of elements (tetrahedra) between the slices (20+11) applying a scale factor between root and tip section.

The resulting mesh is shown in Fig. 44. The number of nodes is 31124 and the number of elements is 173445. The supposed emplacement of the transonic shock is refined.

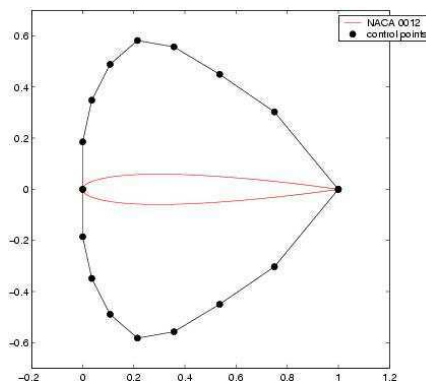


Figure 39: NACA0012 and its control points

Simplex method

Let us take the simplex method of Nelder-Mead as in Chapter 5 and perform several tests for our test-case with different degrees of parameterization and different settings.

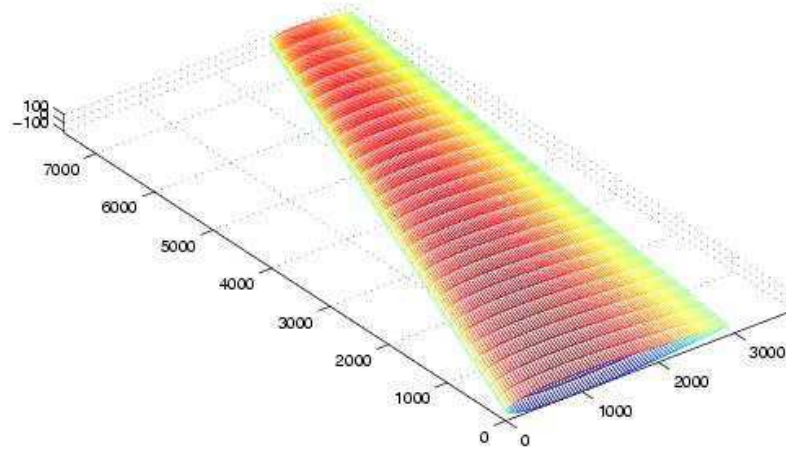


Figure 40: 3D wing

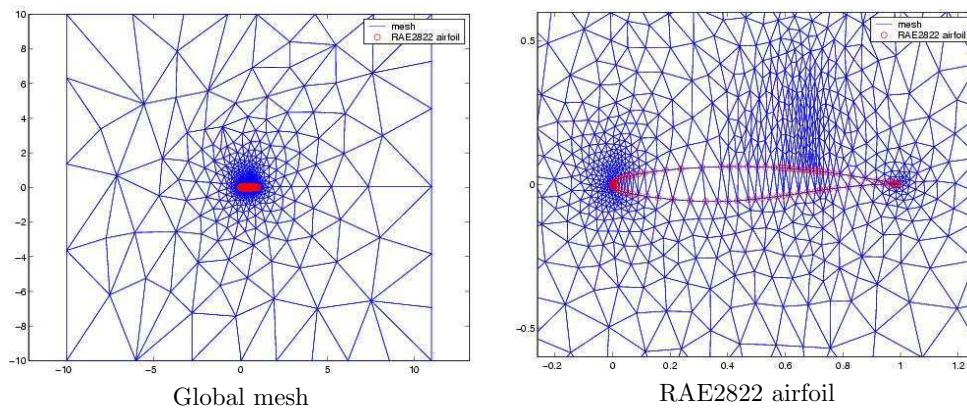


Figure 41: 2D transonic mesh (also in the interior of the profile)

First of all, we will take degree 6-1-1 parameterization (ie. the coarsest) and test the quality of solutions and convergence speeds of the simplex method with respect to the simplex diameter (size) of the initial simplex.

We shall remember that simplex method finds local minimum only.

Secondly, we study the possibility of saving up to 50% of CPU time by poorer resolution of the flow problem and its effects on the quality of the solution.

The two kind of tests as above are then repeated for the finest parameterization of degree 9-1-1.

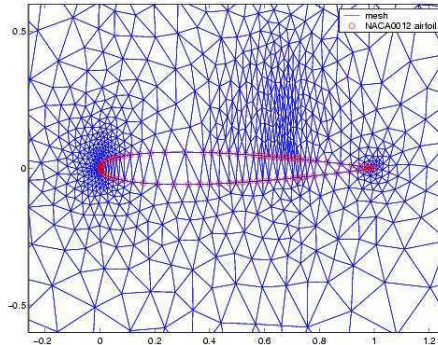


Figure 42: NACA 0012 mesh (also in the interior of the profile)

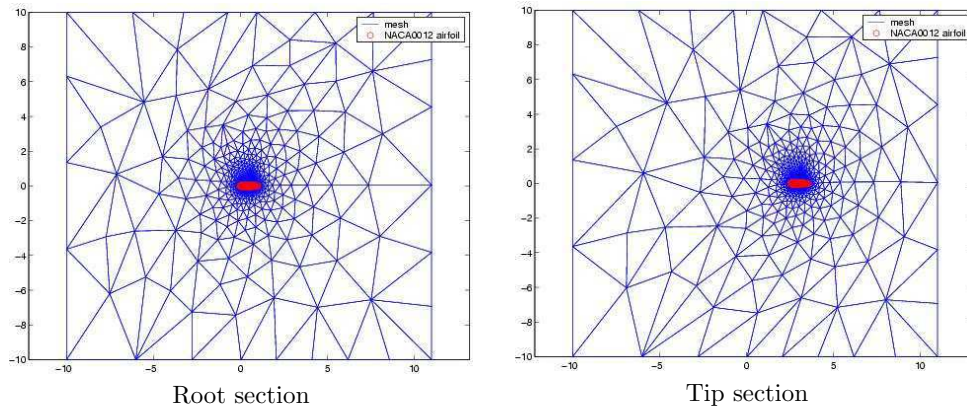


Figure 43: Example of 2 slices (root and tip section)

After this validation phase, we will finally study the influence of the degree-elevation strategy on the speed of convergence.

6.3 Simplex method for coarse parameterization (degree 6-1-1)

6.3.1 Simplex size

Simplex method being one of the methods of descent, it tends to converge to local minima only. Nevertheless, unlike a gradient-based method, the descent is tested only in discrete values of parameters - the simplex vertices. Therefore, by choosing a big simplex at initialization, it might happen that the simplex during its reflection iterations will be able to skip local minima.

Let us test this idea numerically: starting from the same initial solution, we will compare convergence and quality of solution when using a small simplex (simplex diameter $\epsilon = 10^{-1}$) or a large simplex ($\epsilon = 10^{+2}$). The definition of the 2 test-cases is summarized in Tab. 4.

In Figs. 45 - 46 and in Tab. 5 we can see the convergence history and the fitness results. In the convergence history plots, we show the fitness of all $n + 1$ simplex vertices at each iteration (evolutions) of the simplex, n is the number of design parameters. At the same time, we give the minimum envelope of the fitness on the right of the convergence plot. Usually, between 2

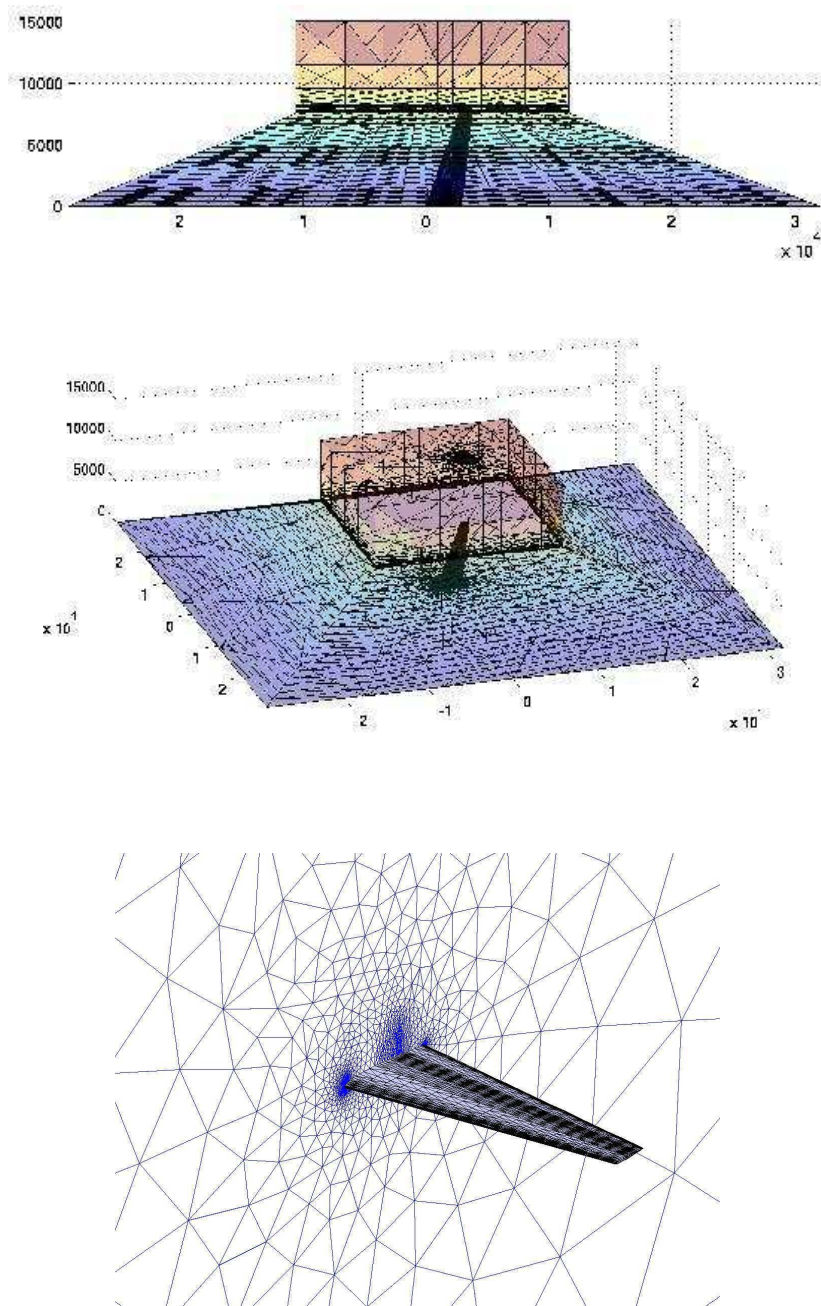


Figure 44: 3D mesh: wing and far-field boundaries (above), detail of the wing and symmetry plane (below).

	degree	res	ϵ
Testcase A	6-1-1	10^{-6}	10^{-1}
Testcase B	6-1-1	10^{-6}	10^{+2}

Table 4: Testcases A and B parameters

iterations of the simplex method, we need just one evaluation of fitness. In Fig. 46, however, we can observe a particular behaviour of the method around the 40th iteration : a massive resizing (shrinking) of the simplex, in the reduction move.

In Fig. 47 we can see the Mach field for the two solutions and the comparison in the root and tip sections.

The results of this test drives us to say that the choice of the simplex diameter ϵ in the method is very important. The differences in the solution quality and in the convergence speed are great. It seems, that starting with larger simplices is advantageous. One may explain this observation by the fact, that our cost-function has multiple local minima and that bigger *simplex diameter* of initial simplex gives the possibility to skip some of the local minima.

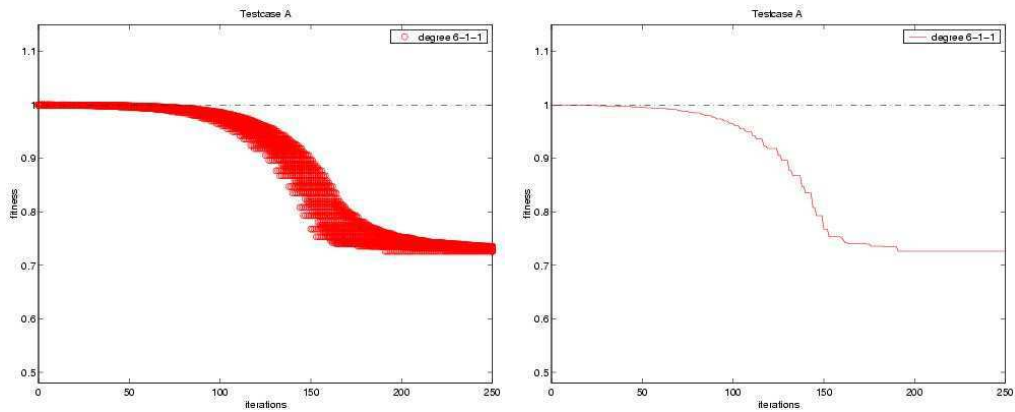


Figure 45: Convergence history (testcase A) - small simplex

	C_L	C_D	Fitness	Variation
Original	0.3192007875	0.0263532471	1	
Testcase A	0.3189389963	0.0191390335	0.726249536	-27.4%
Testcase B	0.3188854856	0.0129805887	0.492561266	-50.8%

Table 5: Testcases A and B results (large vs. small simplex)

6.3.2 Non linear flow residual

We have remarked in the precedent experience, that for one optimization test one needs about 300-400 cost function evaluations, ie. calculate 300-400 times the flow problem. The relative CPU time is several days. One natural question is whether or not we can save time by, for

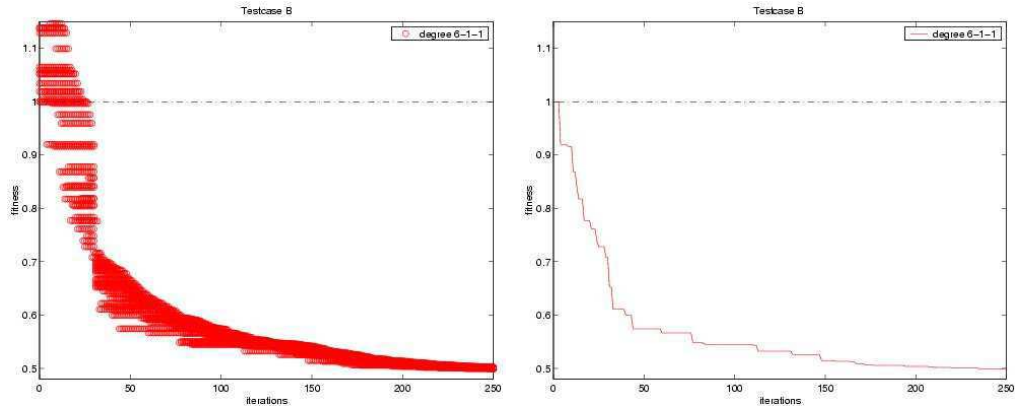


Figure 46: Convergence history (testcase B) - large simplex

example, simply changing our non linear flow residual, and resolving just roughly the flow problem.

Let us compare two optimizations using large initial simplex and resolving the flow problem either only very weakly, or almost completely. The CPU time difference between the two is almost 75%.

The parameters of the test-case are shown in Tab. 6.

	degree	ϵ	res
Testcase C	6-1-1	10^{+2}	10^{-3}
Testcase D	6-1-1	10^{+2}	10^{-6}

Table 6: Testcases C and D parameters

In Fig. 48 and in Tab. 8 we can see the convergence history and the fitness results. The values for the original wing are taken from the solution with non linear flow residual 10^{-6} .

In Fig. 49 we can see the computational time in hours. We notice, that the CPU-cost is rather different for the two cases. The attained solutions have similar fitness - the difference in fitness is only 0.1%. The solutions in terms of the optimal shapes are qualitatively similar, but not the same, see Fig. 50.

Let us repeat our experiment for small initial simplex $\epsilon = 10^{-1}$. The test-case definition is in Tab. 7.

	degree	ϵ	res
Testcase E	6-1-1	10^{-1}	10^{-3}
Testcase F	6-1-1	10^{-1}	10^{-6}

Table 7: Testcases E and F parameters

From the results that we can see in Tab. 9 and in the Fig. 52, we observe that in this case the differences in fitness (2.8%) and in the wing section are more important. It follows, probably, from the fact that the simplex size ϵ is small, hence the difference of simplex vertices in terms of shape is small, and just an approximative solution of the flow is not able to recognize it.

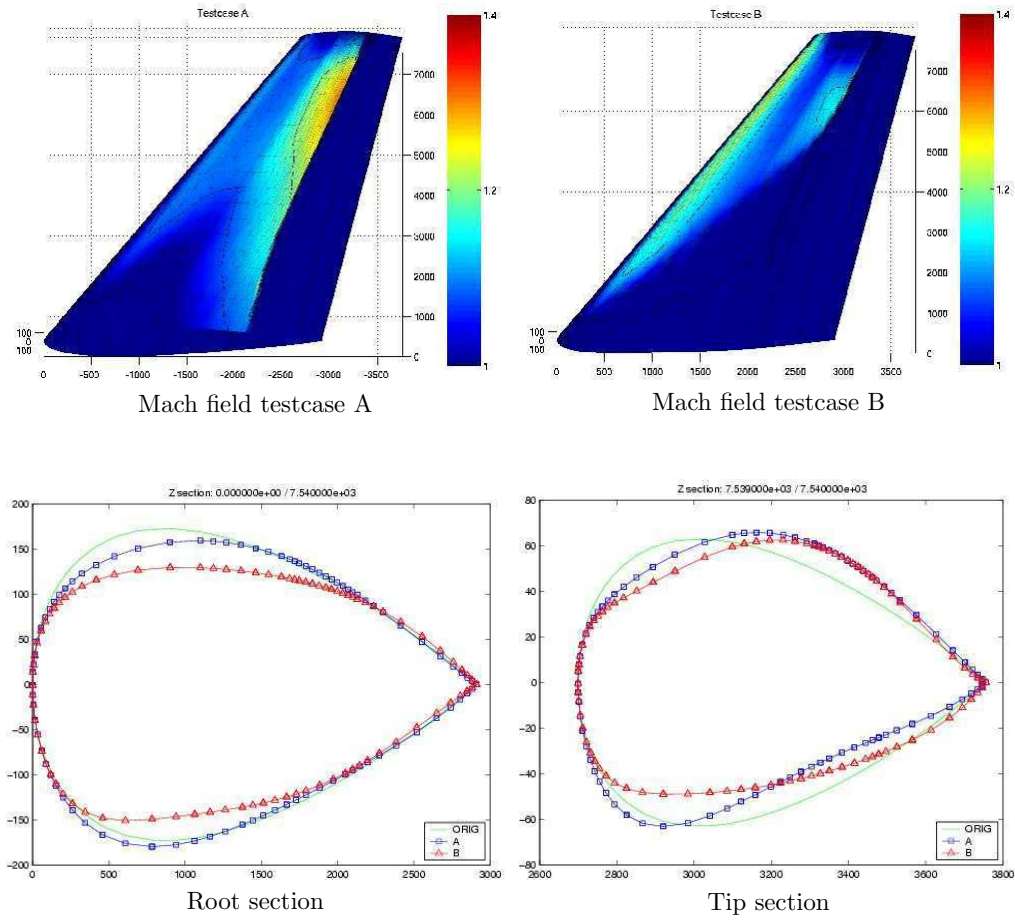


Figure 47: Testcases A and B

It seems, at this point, that saving time by just an approximative flow resolution might be viable. However, as we will see later, experiments for parameterizations 9-1-1 show that this way is quite dangerous, due to the diminished aptitude of the approximative solver to distinguish small variations of shape.

	C_L	C_D	Fitness	Variation
Original	0.3192007875	0.0263532471	1	
Testcase C	0.3190279479	0.0130044710	0.493453061	-50.7%
Testcase D	0.3188854856	0.0129805887	0.492561266	-50.8%

Table 8: Testcases C and D results

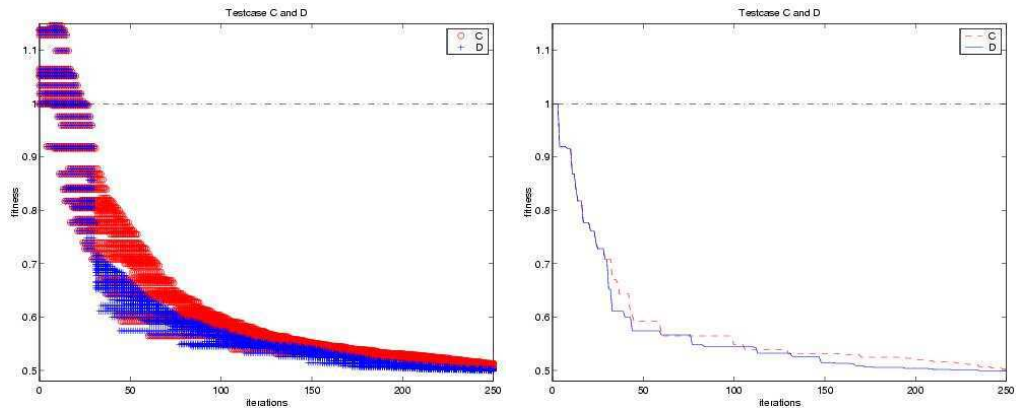


Figure 48: Convergence history (testcases C and D): precise vs. rough flow resolution for large simplex.

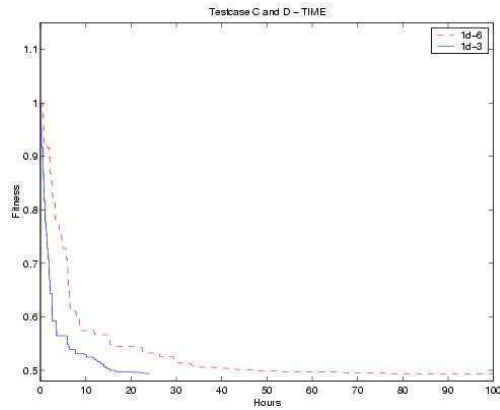


Figure 49: Computational time (testcases C and D)

	C_L	C_D	Fitness	Variation
Original	0.3192007875	0.0263532471	1	
Testcase E	0.3269697856	0.0198700887	0.753968091	-24.6%
Testcase F	0.3189389963	0.0191390335	0.726249536	-27.4%

Table 9: Testcases E and F results: precise vs. rough flow resolution for small simplex.

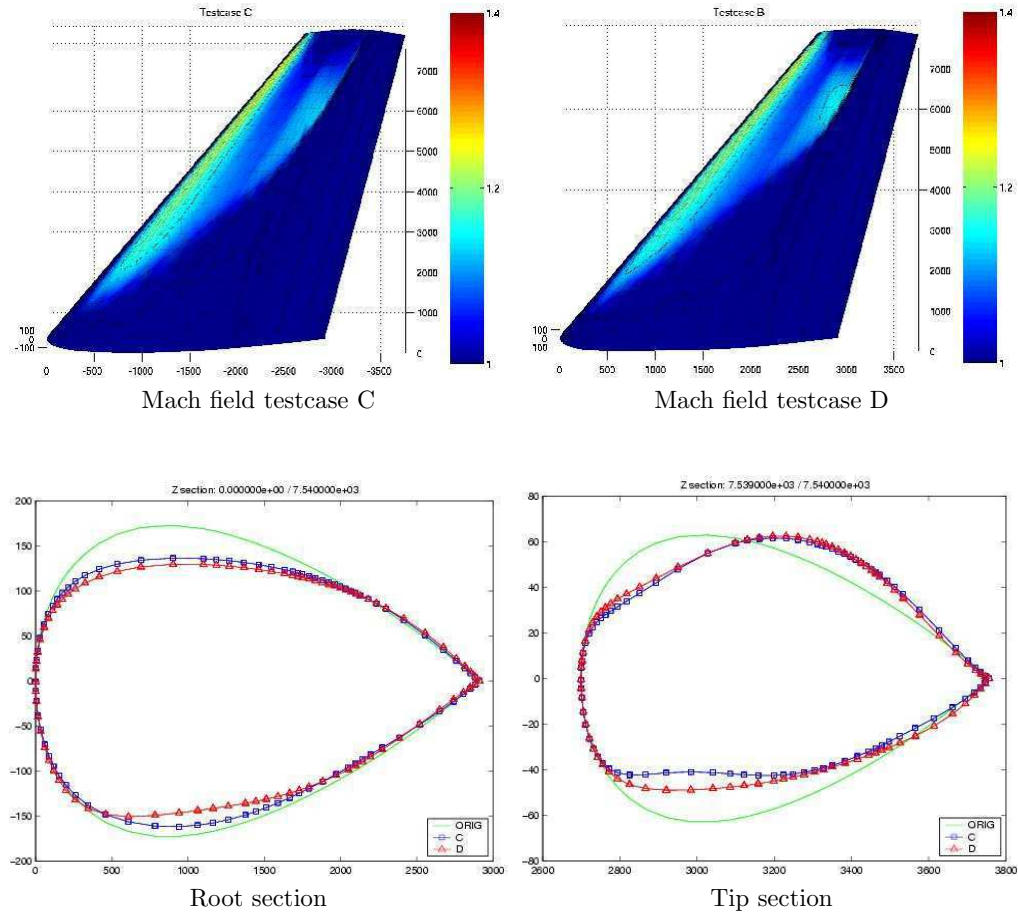


Figure 50: Testcases C and D

6.4 Simplex method for rich parameterization (degree 9-1-1)

Let us now refine our parameterization and use degree 9 in chord direction (9-1-1). We will repeat the tests concerning the influence of the initial simplex size and rough resolution of flow problems for the richer parameterization.

We follow two aims: first, we want to check our conclusion from Section 6.3 and second, we will compare the behaviour of the optimization with richer parameterization to the coarser one.

6.4.1 Simplex size

As in the experiments for coarse parameterization, let us have two test-cases with the same starting point, one using small initial simplex ($\epsilon = 10^{-1}$), the other using large initial simplex ($\epsilon = 10^{+2}$). The parameters are given in Tab. 10.

In Fig. 53 - 54 and in Tab. 11 we show the convergence history and the fitness results. The

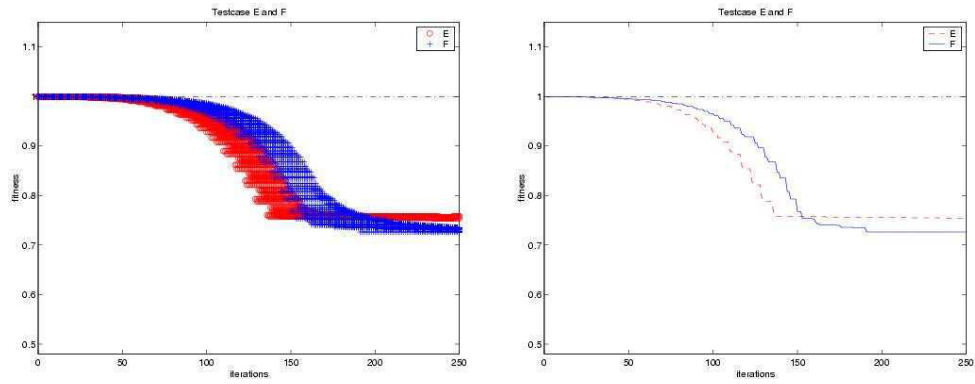


Figure 51: Convergence history (testcases E and F)

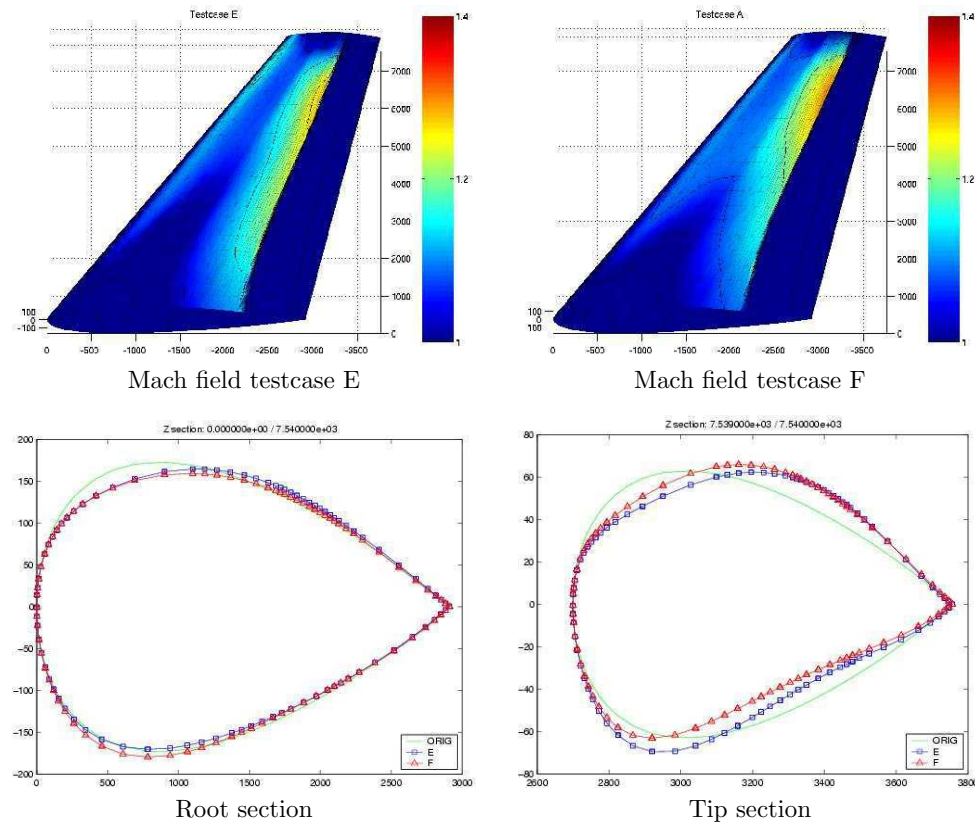


Figure 52: Testcases E and F

quality of the solutions is like in the testcases A and B corresponding for coarse parameterization (see Fig. 45 - 46) but we note here that the number of iterations for the degree 9-1-1, fine

	degree	res	ϵ
Testcase G	9-1-1	10^{-6}	10^{-1}
Testcase H	9-1-1	10^{-6}	10^{+2}

Table 10: Testcases G and H parameters

parameterization, is double. The two-time slower convergence in this test-case hints the stiffness of the optimization problem with respect to the number of parameters increasing.

In Fig. 55 there are the comparisons between the Mach field and the root and tip sections.

In this case, like for degree 6-1-1, we can say that the choice of the initial simplex size ϵ is important for the result. Like for coarse parameterization, the difference of best fitnesses of optimal shapes given by the two simplex algorithms is rather substantial - about 30% of the original drag.

This time, however, for the large simplex we did not have to use simplex shrinking which would result in a massive resizing and reevaluation of the whole simplex, like it has been noticed in Fig. 46 (40th iteration).

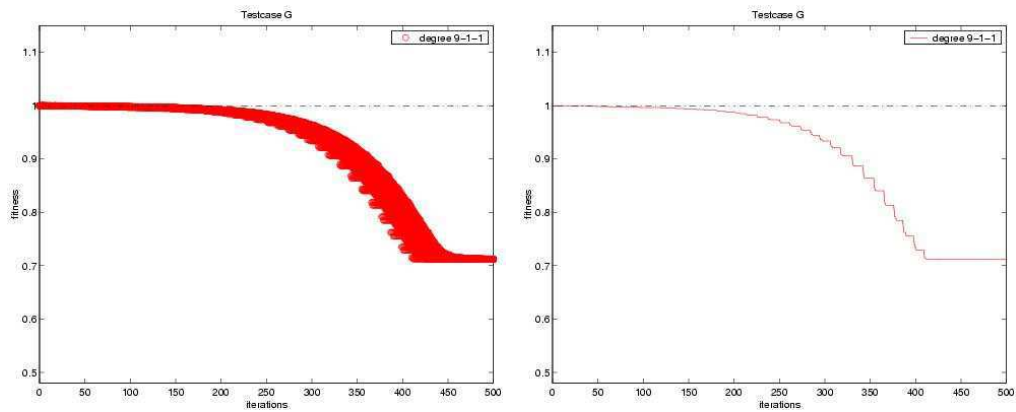


Figure 53: Convergence history (testcase G) - small simplex

	C_L	C_D	Fitness	Variation
Original	0.3192007875	0.0263532471	1	
Testcase G	0.3261269982	0.0187096749	0.709957104	-29.01%
Testcase H	0.3190795710	0.0130757173	0.496170934	-50.4%

Table 11: Testcases G and H results: small vs. large initial simplex

6.4.2 Non linear flow residual

Let us, also in this case, test the influence of non-exact solution of the flow problem at the convergence and quality of the results. First, take large initial simplex. The specifications of the testcases is in Tab. 12.

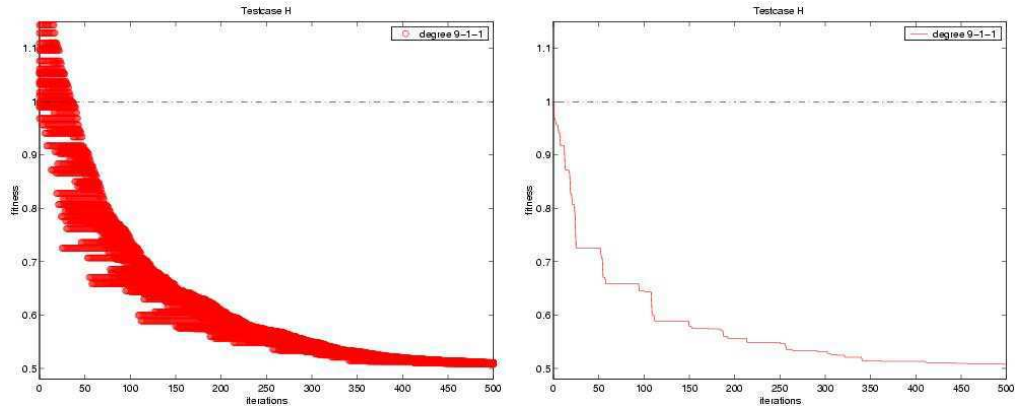


Figure 54: Convergence history (testcase H) - large simplex

	degree	ϵ	res
Testcase I	9-1-1	10^{+2}	10^{-3}
Testcase L	9-1-1	10^{+2}	10^{-6}

Table 12: Testcases I and L parameters

Fig. 56 and Tab. 14 show the convergence history and the fitness results. It seems, that in both cases, the simplex algorithm was able to attain similar fitness.

We can see the difference in computational time in Fig. 57. By using the inexact solver of the flow problem we have gained 50% of the CPU time.

In Fig. 58 we plot the Mach field and the root and tip sections for the two testcases.

From all the results obtained so far by lowering the non linear flow residual, it seems that if we are interested only in a qualitative solution and we want to save time, we can solve our optimization with an inferior flow residual. This statement is not always true, however.

A counter-example follows by using small initial simplex, see specification in Tab. 13.

	degree	ϵ	res
Testcase M	9-1-1	10^{-1}	10^{-3}
Testcase N	9-1-1	10^{-1}	10^{-6}

Table 13: Testcases M and N parameters

We can see in Fig. 59 - 60 that the two solutions in this case are very different. In particular, the testcase M shows a very small gain in fitness (see Tab. 15).

It seems that by reducing the precision of the flow solver we have lowered the threshold with which the flow solver is capable to distinguish two slightly different shapes. This, together with the fact that we start with a small simplex, ie. precisely with very small shape variations to choose from, results in a complete stagnation of the convergence.

However, if the threshold sensitivity of the flow solver matches the simplex size, the optimization with an approximate flow solver tends to give qualitatively good results two times more rapidly than with the precise flow resolution.

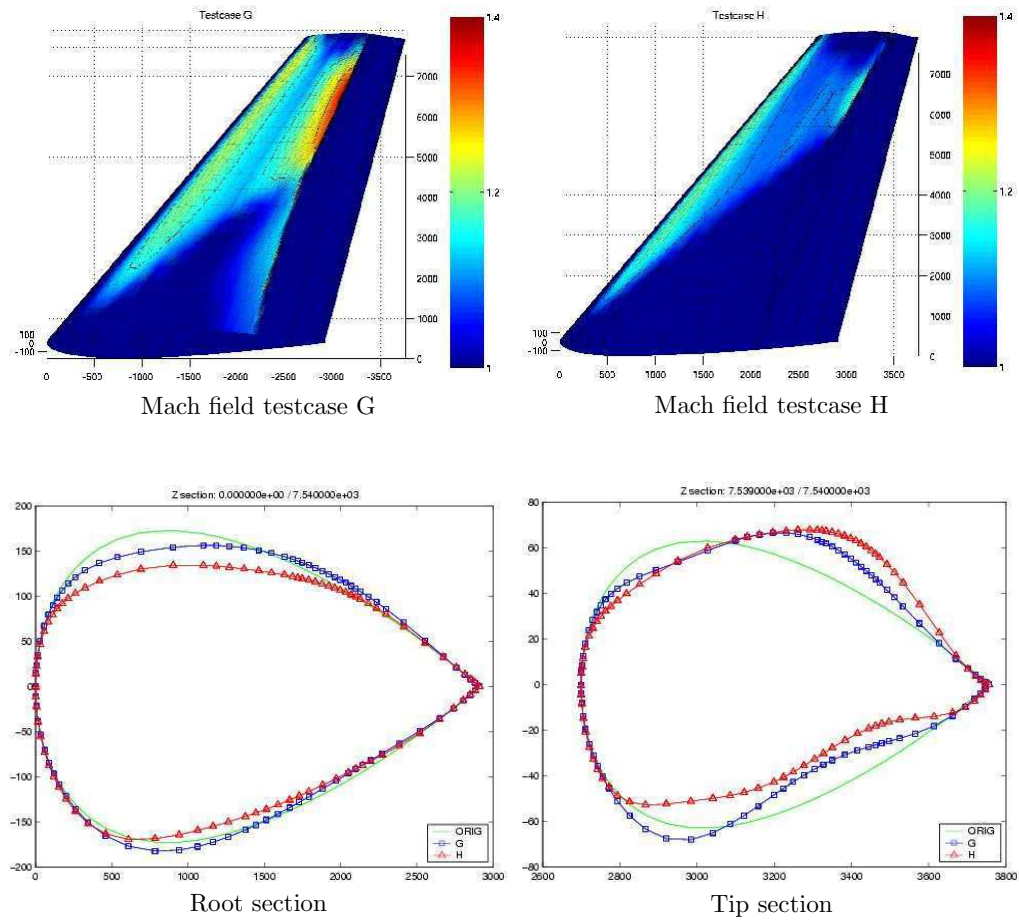


Figure 55: Testcases G and H: small vs. large initial simplex

	C_L	C_D	Fitness	Variation
Original	0.3192007875	0.0263532471	1	
Testcase I	0.3194382263	0.0133210986	0.505467458	-49.5%
Testcase L	0.3190795710	0.0130757173	0.496170934	-50.4%

Table 14: Testcases I and L results: precise vs. rough flow resolution for large simplex.

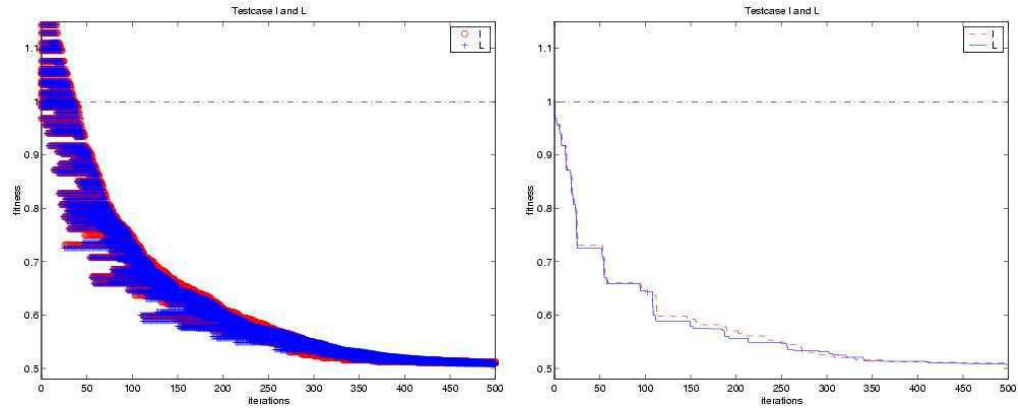


Figure 56: Convergence history (testcases I and L): precise vs. rough flow resolution for large simplex.

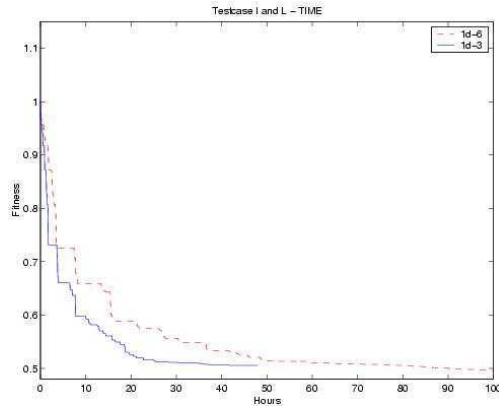


Figure 57: Computational time (testcases I and L)

	C_L	C_D	Fitness	Variation
Original	0.3192007875	0.0263532471	1	
Testcase M	0.3188905806	0.0261525242	0.992354335	-0.8%
Testcase N	0.3261269982	0.0187096749	0.709957104	-29.01%

Table 15: Testcases M and N results: precise vs. rough flow resolution for small simplex.

6.5 Simplex method with degree elevation

After some preliminary tests with the simplex method, we have noticed that the optimization problem converges almost two times less rapidly for parameterization of degree 9-1-1 than with the parameterization 6-1-1.

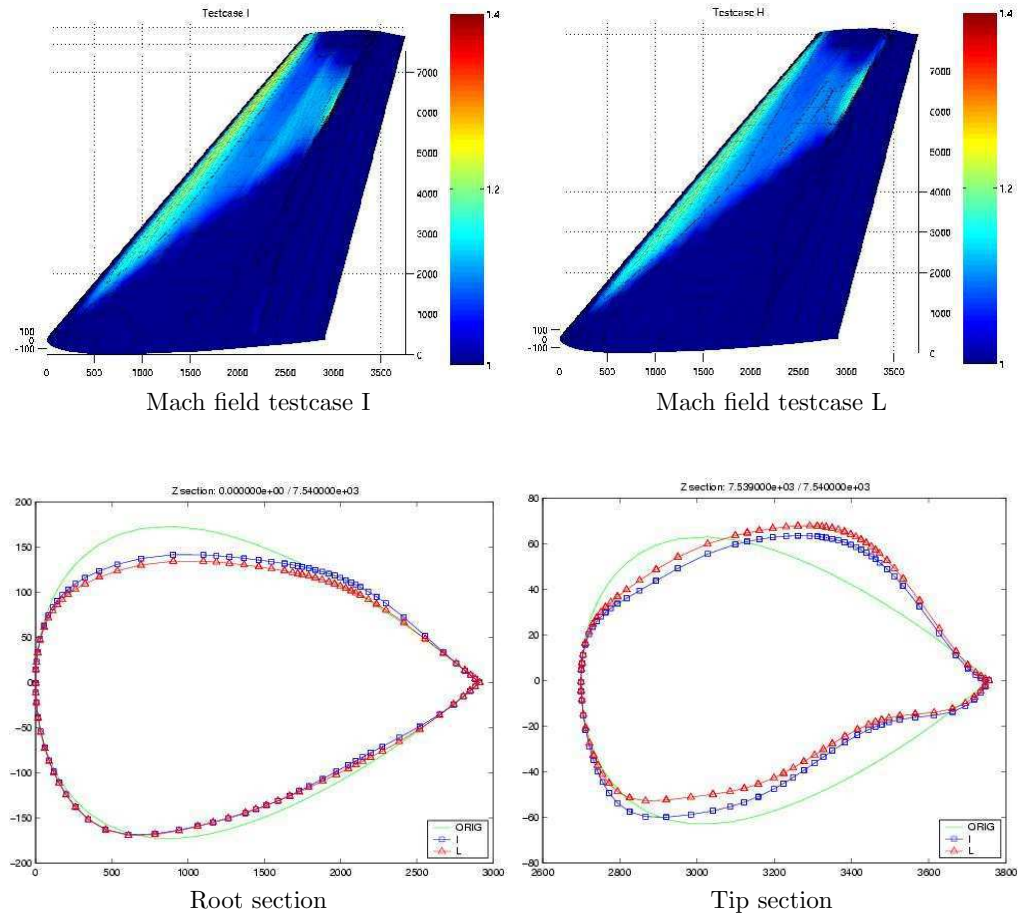


Figure 58: Testcases I and L: precise vs. rough flow resolution for large simplex.

Now, we are about to testign the following idea: by successive enriching of the parametric space, we could start with a low-degree parameterization to speedup the convergence, but during the optimization process, we could switch to higher-degrees of parameterizations until the target refinement is attained. The key in the successive refinement process is not to lose information gained in the precedent steps. Therefore, we use the degree-elevation property of Bézier parameterization, which assures that shapes are represented *exactly* by the parameterization enriching. To respect our constraints on planform preserving and no-double curvature, we are applying, in 4 steps, the degree elevation just in x-direction (chordwise), obtaining successively degrees 6-1-1, 7-1-1, 8-1-1 and 9-1-1, which is our target space.

In the following two Scetions, we are making some numerical tests and comparisons of such an hierarchical optimization with a degree 9-1-1 only optimization.

Also, we try to gain some experience on how the simplex vertices should be treated during the degree-elevation. Indeed, as we pass from a coarse parameterization with parameters from \mathbb{R}^{n_1} to a richer parameterization with parameters from \mathbb{R}^{n_2} , $n_2 > n_1$, our $n_1 + 1$ -simplex should

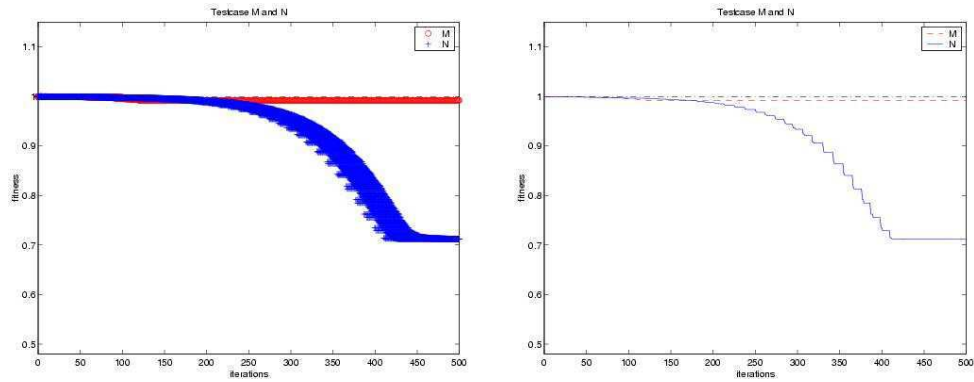


Figure 59: Convergence history (testcases M and N): precise vs. rough flow resolution for small simplex.

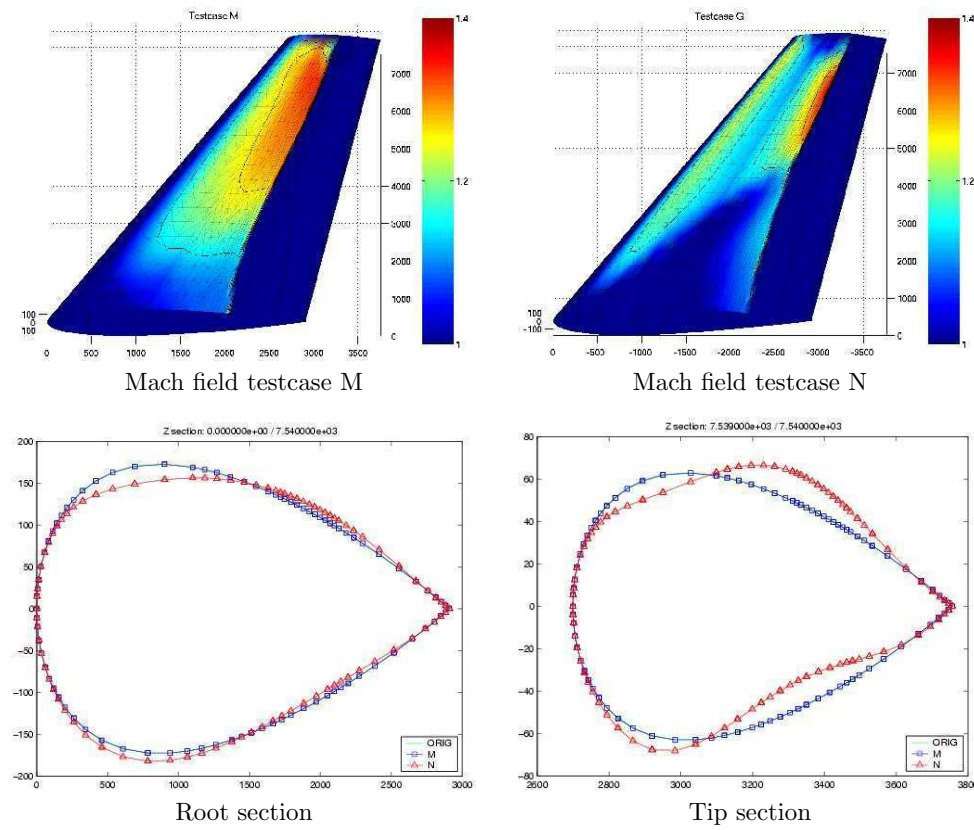


Figure 60: Testcases M and N: precise vs. rough flow resolution for small simplex.

be mapped to a $n_2 + 1$ -simplex with more vertices. Two issues need to be treated: we do not want to lose information already gained in the optimization process and we need to assure the non-degenerescence of the new simplex in order to better explore all \mathbb{R}^{n_2} .

In this respect, we are going to try two strategies for degree elevation of a simplex: either just the best individual will be elevated and then a new simplex will be created by an ϵ -perturbation of this individual, or the whole simplex will be elevated and just the complementary vertices will be obtained by perturbation.

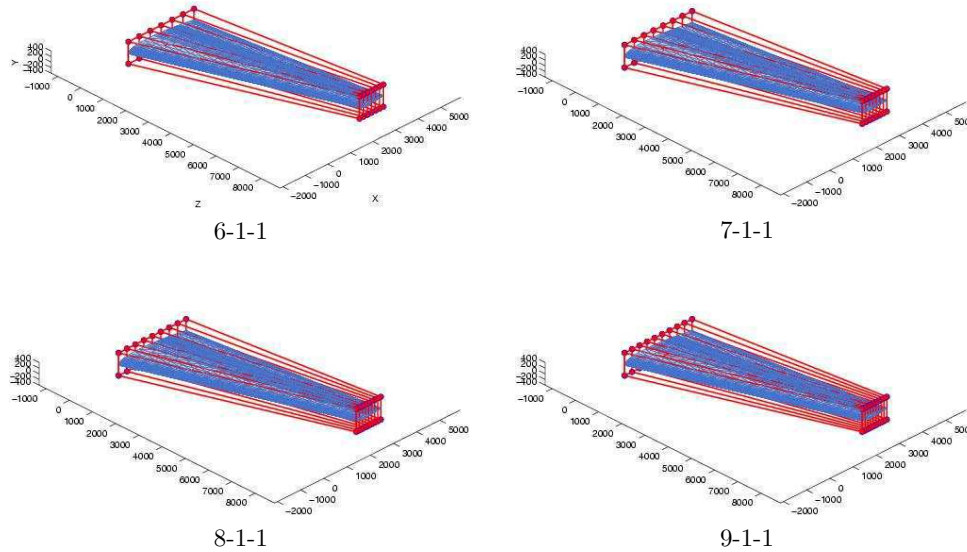


Figure 61: Degree elevation

6.5.1 Testcase 1: degree elevation for small simplex.

First of all, let us try the degree elevation strategy for a small simplex. Let us start with 250 simplex iteration for the coarse parameterization (degree 6-1-1). Then, we elevate the best individual/vertex and set up a new simplex of size ϵ (simplex diameter) by perturbation of the best individual using parameterization of degree 7-1-1. After another 250 simplex iterations we elevate the degree to 8-1-1 and, still after another 250 iterations, we finish with degree 9-1-1.

Let us compare convergence histories, convergence speed and quality of the solution for two tests with a different flow solver precision (non-linear flow residual). The test-case parameters are displayed in Tab. 16, the symbol $6 \rightarrow 9$ means that parameterization has been progressively enriched from 6-1-1 to 9-1-1 by one degree at a time.

	degree	ϵ	res
1A	$6 \rightarrow 9$	10^{-1}	10^{-3}
1B	$6 \rightarrow 9$	10^{-1}	10^{-6}

Table 16: Testcase 1

In Fig.62 we can see the convergence history and the CPU-time for these two cases. We see, that the experiment with the more precise solver has found by about 7% better solution.

The differences in C_L , C_D and fitness can be seen in Tab. 17.

Root and tip sections and the Mach field distributions are shown in Fig. 63.

By using just an approximative flow solver, we have saved almost 50% of the CPU-time and the obtained solution is qualitatively similar to the one obtained by a precise solver.

	C_L	C_D	Fitness	Variation
Original	0.3192007875	0.0263532471	1	
1A	0.3582733176	0.0178659400	0.677920912	-32.2%
1B	0.3191661183	0.0160547968	0.609215129	-39.1%

Table 17: Testcase 1

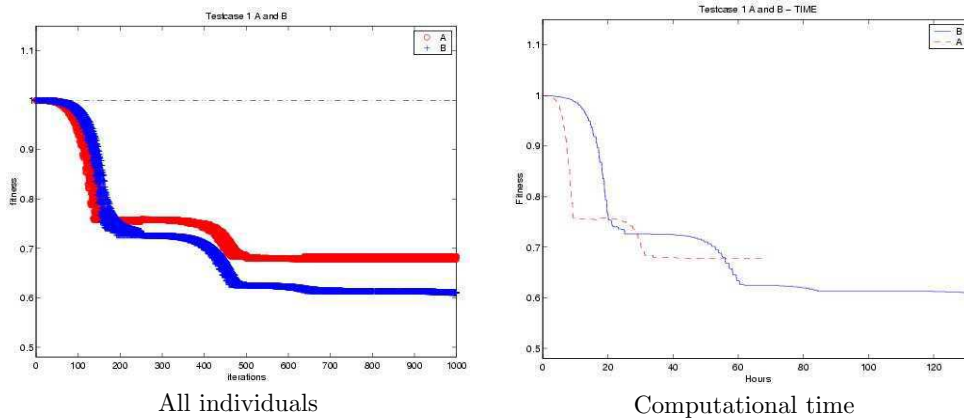


Figure 62: Degree elevation convergence history: small simplex precise vs. rough flow solver.

6.5.2 Testcase 2: degree elevation of best vs. all simplex vertices.

As we have remarked in the introduction of this section, the key question with degree elevation is how to keep already gained information and, at the same time, do not degenerate the search into only a subspace of the new parameterization. Here, we design a test-case which should reveal the influences on the choice of the degree-elevation strategy: taking the simplex method with large initial simplex ($\epsilon = 10+2$) and degree 6-1-1 parameterization, we do 250 simplex iterations and then elevate to 7-1-1. For one optimization we elevate only the best vertex/individual and re-create a new simplex by perturbations with $\epsilon = 10+2$ around the best individual (test 2A). For the other optimization we elevate all simplex vertices and complement them with the perturbations ($\epsilon = 10+2$) around the best individual (test 2B). Then we perform, for both algorithms, another 250 iterations of simplex method and repeat the degree elevation to get degree 8-1-1. We repeat this process until the final 250 iterations are in degree 9-1-1 parametric space, see Fig. 64. The test-case parameter are summarized in Tab. 18.

In Tab. 19 and in Fig. 65 we can see that the two solutions are very similar in fitness but not in the shape.

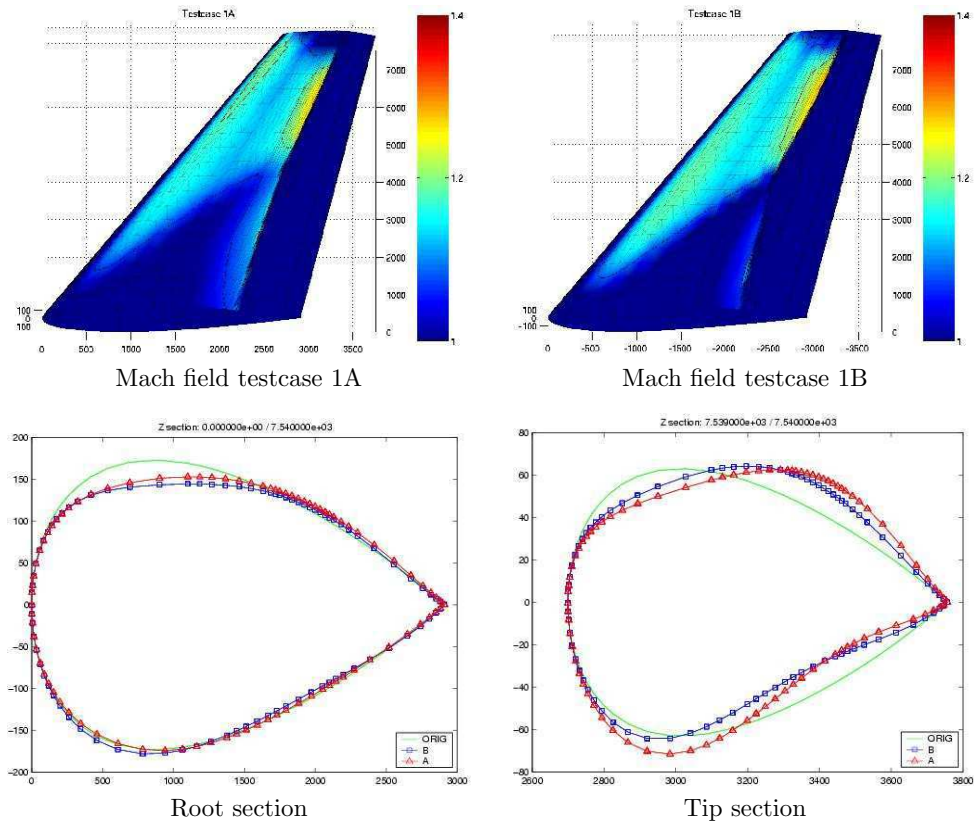


Figure 63: Testcases 1 (A and B)

	degree	ϵ	res
2A	6 \rightarrow 9	10^{+2}	10^{-6}
2B	6 \rightarrow 9	10^{+2}	10^{-6}

Table 18: Testcase 2

It seems that the choice for the elevation is not very important in the convergence speed

	C_L	C_D	Fitness	Variation
Original	0.3192007875	0.0263532471	1	
2A	0.3188849846	0.0125971202	0.478010097	-52.2%
2B	0.3194768778	0.0125152769	0.474904470	-52.5%

Table 19: Testcase 2

and in the quality of the solution, measured by the fitness. The optimum shapes however, are different, see Fig. 65.

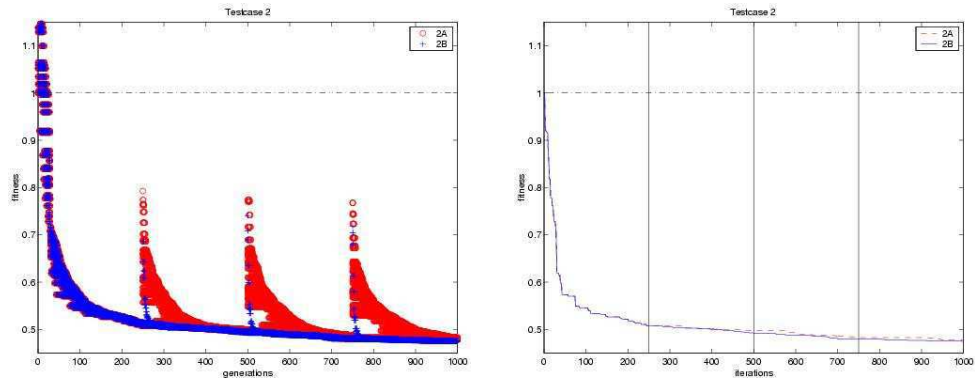


Figure 64: Convergence history (testcase 2)

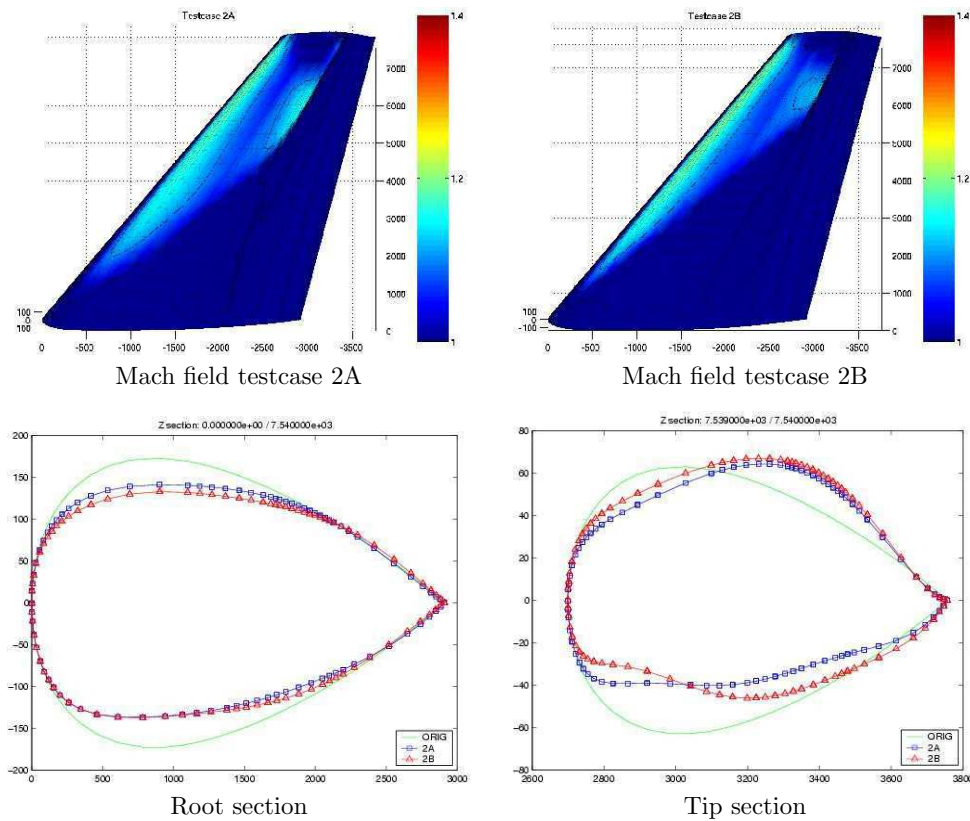


Figure 65: Testcases 2 (A and B): degree elevation, best vs. all.

6.6 Parameterization enriching vs. finest parameterization only.

In the elevation process, we successively enrich the parametric space starting from a coarse parameterization going towards the finest one. Hence, the results could be compared to an optimization process using the finest parameterization only (fixed degree).

It is interesting to see if we are able to improve the quality of the solution or we are able to have the same fitness with less iterations (in less CPU-time).

We remember here that, in general, if we have the same fitness from two tests, the shape of the wing can be different.

Let us compare the already presented test-cases from a different prospective. The test-case G and 1B, for small simplex, are of interest, we recapitulate their parameters in Tab. 20.

	degree	ϵ	res
G	9 - 1 - 1	10^{-1}	10^{-6}
1B	6 \rightarrow 9	10^{-1}	10^{-6}

Table 20: Testcases G vs. 1B

A comparison of the results can be seen in Tab. 21. The convergence is shown in Fig. 66.

	C_L	C_D	Fitness	Variation
Original	0.3192006583	0.0263540181	1	
Testcase G	0.3261269982	0.0187096749	0.709957104	-29.01%
Testcase 1B	0.3191661183	0.0160547968	0.609215129	-39.1%

Table 21: Testcase G vs. 1B results

We observe that the elevation process works well in this case. We have attained optimal shape of better quality (lower fitness) and the speed of convergence is faster. In Fig. 67 we can see also that the two solutions are qualitatively very similar.

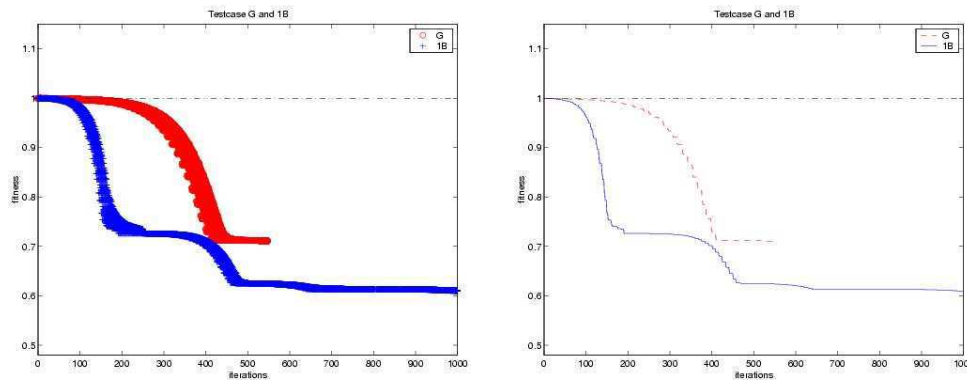


Figure 66: Convergence history: degree elevation vs. one finest parameterization, small simplex

6.6.1 Large simplex

Another interesting comparison is between the testcase 2 of Section 6.5.2 and the testcase L, for large initial simplex. Their parameters are recapitulated in Tab. 22. Here we are comparing

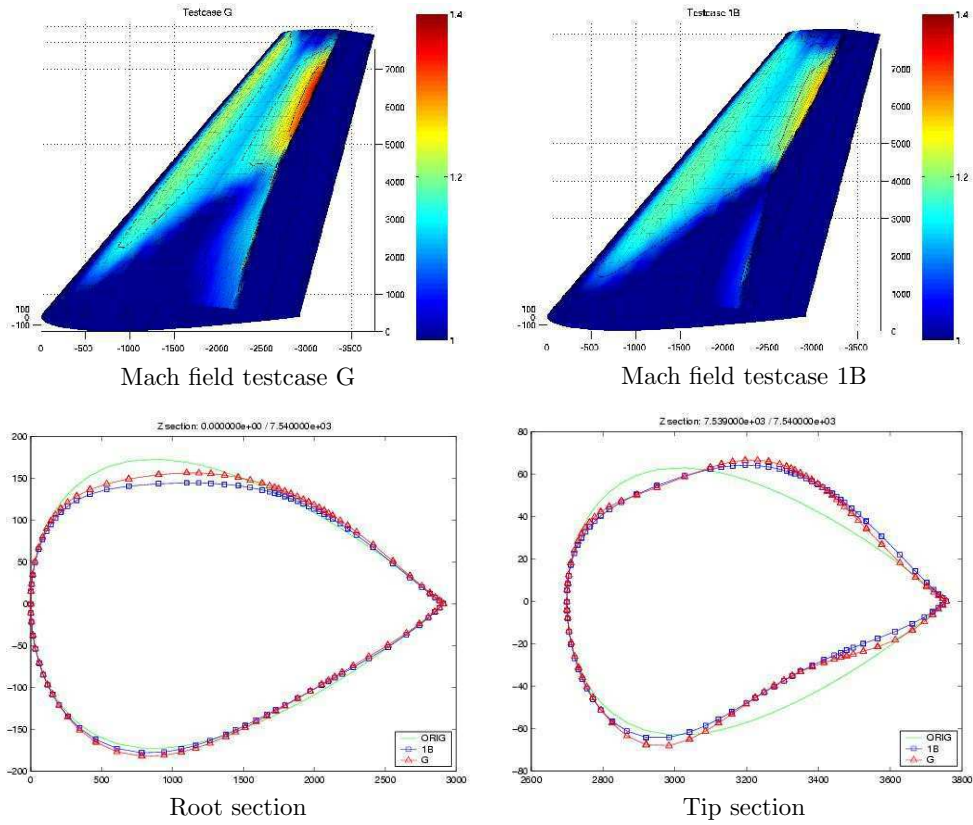


Figure 67: Degree elevation vs. finest parameterization: small simplex.

a degree-elevation testcase 2 with a test-case L using just degree 9-1-1 parameterization during the whole optimization.

	degree	ϵ	res
L	9 - 1 - 1	10^{+2}	10^{-6}
2A	6 \rightarrow 9	10^{+2}	10^{-6}
2B	6 \rightarrow 9	10^{+2}	10^{-6}

Table 22: Testcases L vs. 2

The results can be seen in Tab. 23 and in Figs. 68 - 69.

Also for this test, the speed of convergence is higher with the elevation process. The quality of the solution is slightly better with the elevation test.

The results tend to confirm our perception about the stiffness of the optimization process. It seems, that the more parameters we have, the better quality of the optimal shape we can attain, but also the slower of the convergence of the optimization process. Our degree-elevation seems to work more rapidly, because of its superior convergence speed at the beginning of the optimization where it operates only in coarse parametric space.

	C_L	C_D	Fitness	Variation
Original	0.3192007875	0.0263532471	1	
L	0.3190795710	0.0130757173	0.496170934	-50.4%
2A	0.3188849846	0.0125971202	0.478010097	-52.2%
2B	0.3194768778	0.0125152769	0.474904470	-52.5%

Table 23: Testcase L vs. 2 results

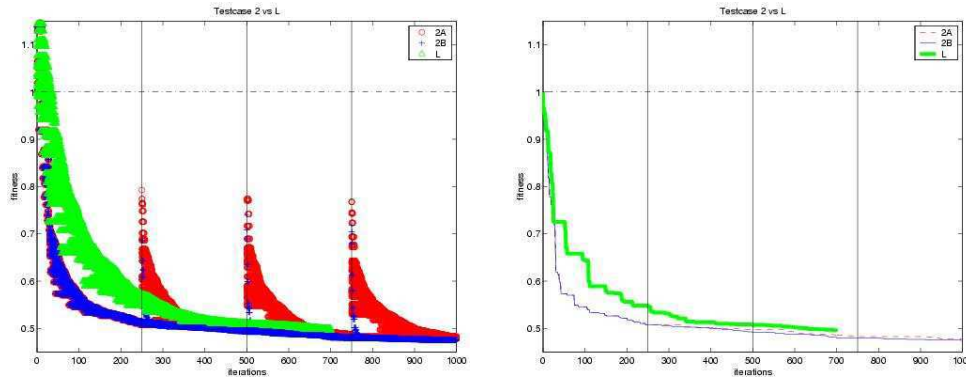


Figure 68: Convergence history: degree elevation vs. finest parameterization, large simplex

6.7 Summary and conclusions for simplex experiments

Let us recapitulate the set-up parameters and results for all the tests performed in this Section, see Tab. 24.

We have seen during all the tests, that the choice of the initial simplex size ϵ seems to be crucial. We suppose that the larger simplices have the potential to overcome *local* minima, as described in Section 6.3.1. However, more tests for different cost functionals (with for example volume-preserving constraints) should be performed to support our hypothesis.

The non linear flow residual results drive us to say that if we are interested only in a qualitative solution, we can save up to 50% CPU-time using just a weak resolution of the flow problem. The residual is strictly correlated with the parameterization degree and the size of the simplex. A small control point displacement for high-degree parameterization creates a perturbation that only an accurate flow solution can recognize/distinguish.

The choice of the degree, as we can see by comparing Figs. 45-46 and Figs. 53-54, has an influence on the number of iterations. Higher degree results in more parameters to optimize.

We remark that even if the fitness from two different tests is almost the same, it does not mean that the shape of the two wings is the same. This should follow from a uniqueness result for the optima, which is not disponible.

In Figs. 70-71 there are the differences between the original wing and the best one obtained with simplex method (test-case 2B). On the left column we have the pressure isolines plot for three different sections (root, mid-section and tip) in spanwise direction and on the right column the C_p distribution.

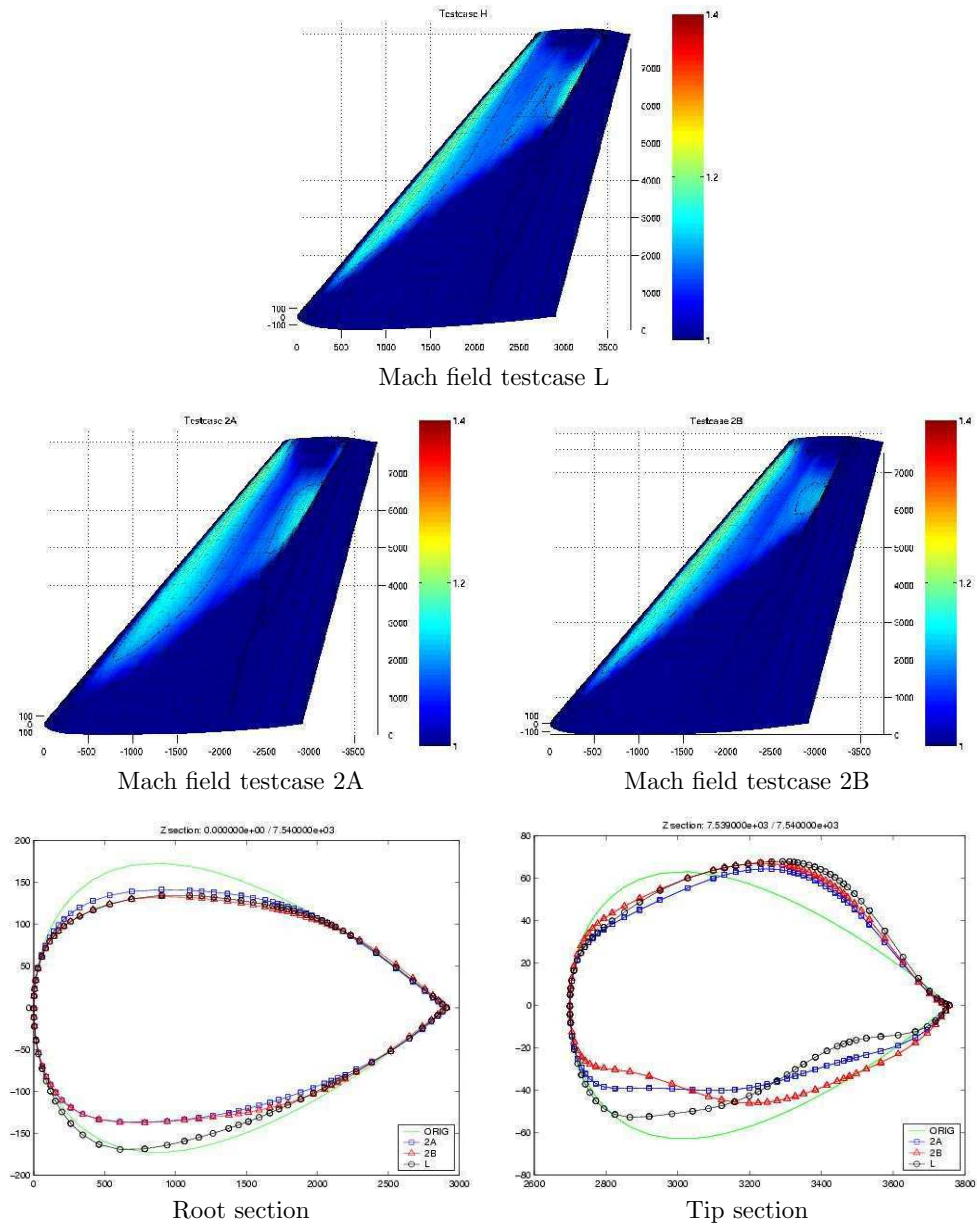


Figure 69: Degree elevation vs. finest parameterization: large simplex.

Testcase	degree	res	ϵ	C_L	C_D	Variation
Orig		10^{-6}		0.3192007875	0.0263532471	
A	6-1-1	10^{-6}	10^{-1}	0.3189389963	0.0191390335	-27.4%
B	6-1-1	10^{-6}	10^{+2}	0.3188854856	0.0129805887	-50.8%
C	6-1-1	10^{-3}	10^{+2}	0.3190279479	0.0130044710	-50.7%
D	6-1-1	10^{-6}	10^{+2}	0.3188854856	0.0129805887	-50.8%
E	6-1-1	10^{-3}	10^{-1}	0.3269697856	0.0198700887	-24.6%
F	6-1-1	10^{-6}	10^{-1}	0.3189389963	0.0191390335	-27.4%
G	9-1-1	10^{-6}	10^{-1}	0.3261269982	0.0187096749	-29.01%
H	9-1-1	10^{-6}	10^{+2}	0.3190795710	0.0130757173	-50.4%
I	9-1-1	10^{-3}	10^{+2}	0.3194382263	0.0133210986	-49.5%
L	9-1-1	10^{-6}	10^{+2}	0.3190795710	0.0130757173	-50.4%
M	9-1-1	10^{-3}	10^{-1}	0.3188905806	0.0261525242	-0.8%
N	9-1-1	10^{-6}	10^{-1}	0.3261269982	0.0187096749	-29.01%
1A	6 \rightarrow 9	10^{-3}	10^{-1}	0.3582733176	0.0178659400	-32.2%
1B	6 \rightarrow 9	10^{-6}	10^{-1}	0.3191661183	0.0160547968	-39.1%
2A	6 \rightarrow 9	10^{-6}	10^{+2}	0.3188849846	0.0125971202	-52.2%
2B	6 \rightarrow 9	10^{-6}	10^{+2}	0.3194768778	0.0125152769	-52.5%

Table 24: Summary results

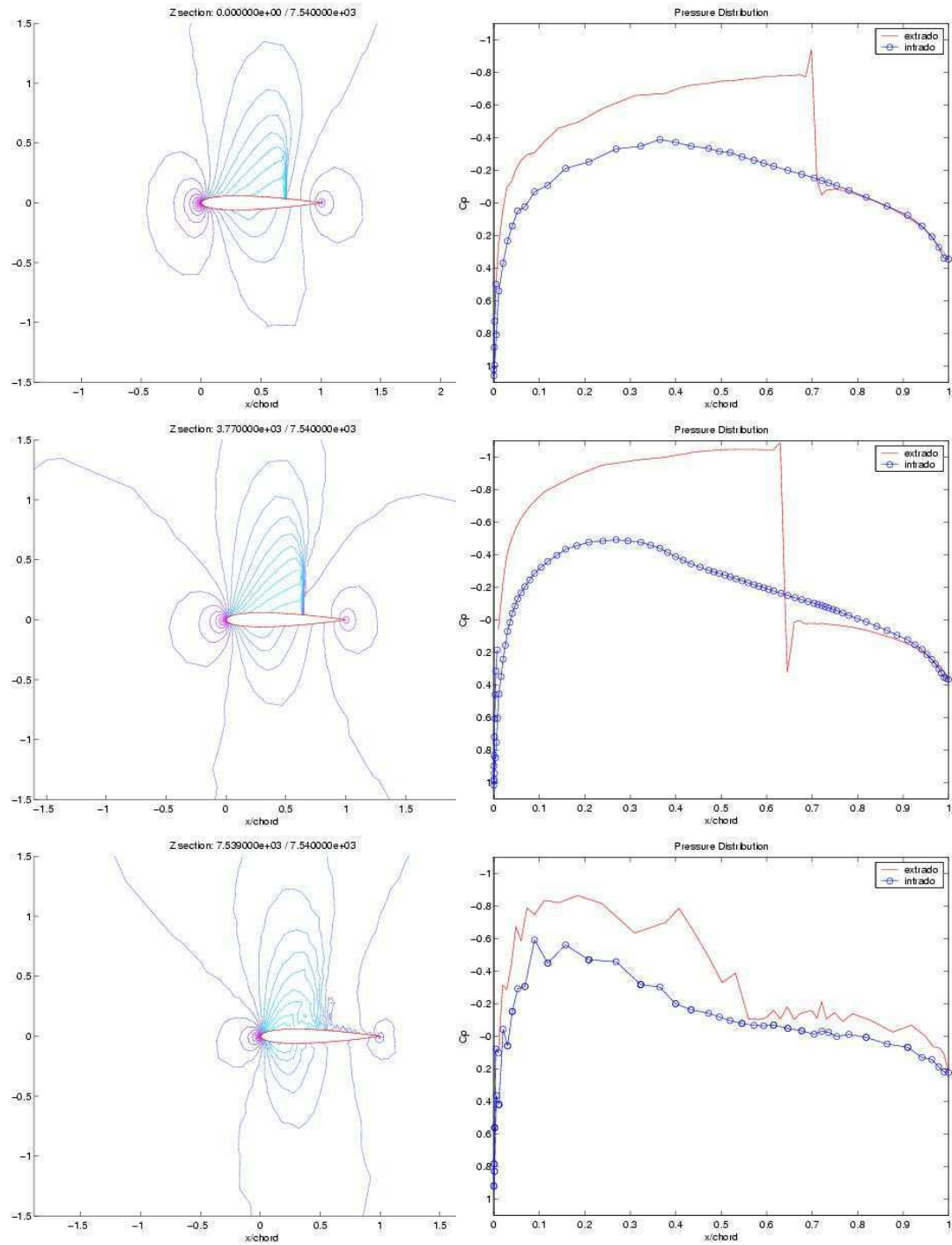


Figure 70: Original Wing

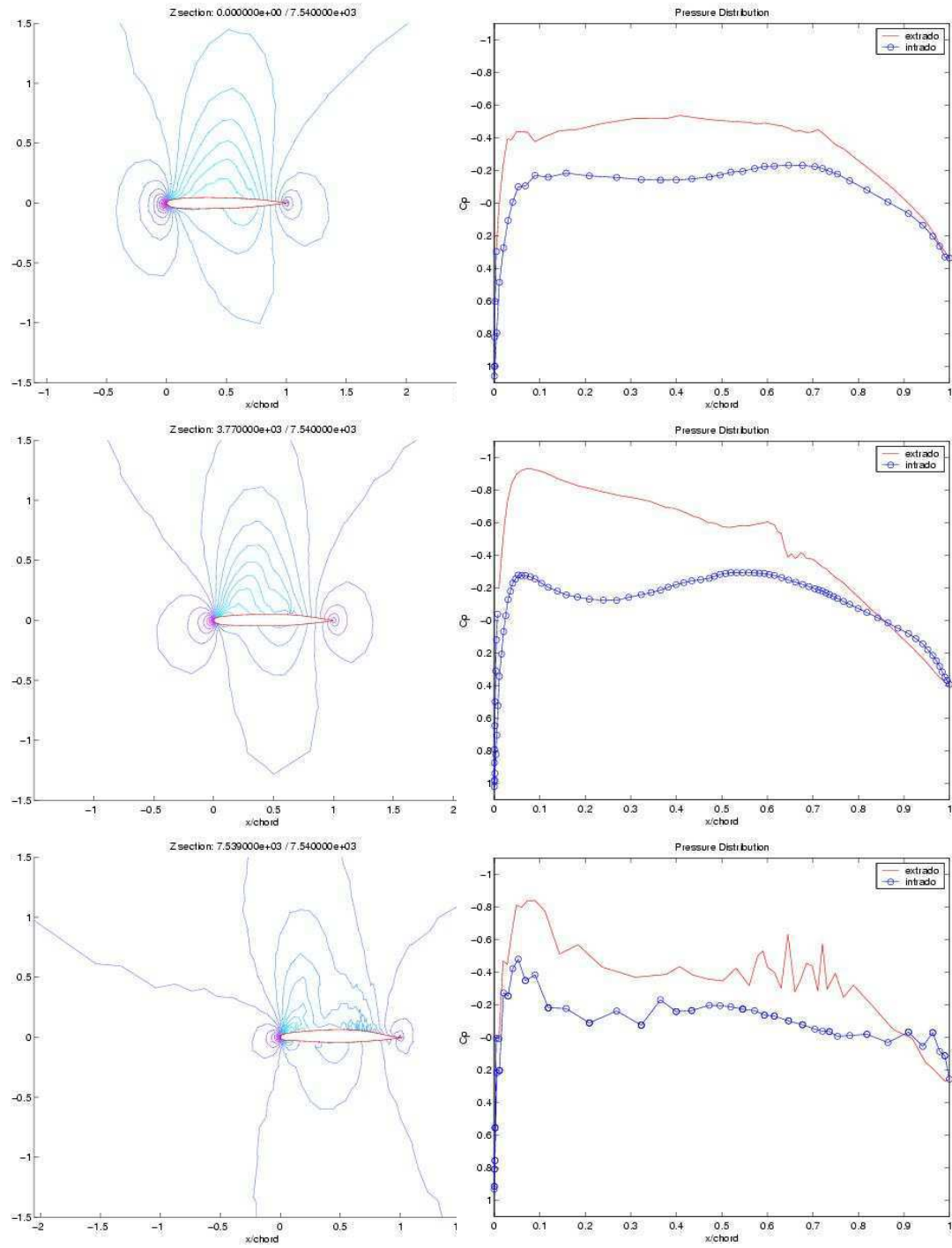


Figure 71: Optimized Wing

Genetic Algorithms

Genetic Algorithms are very robust optimization algorithms. They are very well suited for problems in which the initialization is not intuitive, the minimized cost function may present several local minima. Moreover, they give as a result not only one, but a whole class of potential candidates for optimal shape and they permit to take into account several different minimization criteria. As seen in Chapter 4, they are different from classical optimization procedures (e.g. gradient methods or simplex methods) in many ways:

- they work with a coding of the parameter set and not the parameters themselves
- they work simultaneously with a class/population of individuals/shapes
- they use probabilistic rules (the genetic operators are applied with probabilities)
- they do not work with only one shape and some information about local behaviour of the fitness around this shape (gradient information or descent direction), they use the information of all the population to make *global* choice of optimum.

6.8 Set-up parameters for genetic algorithm

As seen in Section 4.6, in the set-up for genetic algorithms there are a lot of parameters to specify. In all our tests we will work everytime with these parameters and options:

- popsize : 40
- pcross : 0.85
- pmutat : $5 \cdot 10^{-3}$
- selecttype : roulette
- crosstype : 2-point crossover

The maximal number of generations *maxgen* is not fixed and it depends from the test that we choose to run.

The genetic algorithms being extremely costly, the presented test-cases are stopped well before a good convergence has been achieved.

Unlike the simplex method, where we search the parameters in a space of real numbers, with our genetic algorithm with binary coding, we use a fix-point representation of doubles in some interval, called further *Genetic Range*, with some precision. Of course, the more precise our coding is, or the larger *Genetic Range*, the more bits are needed for the encoding of the chromosome.

6.9 Genetic Range

We will show in this paragraph two different choices of the range. It is obvious, that the global optimum might not be within the genetic range. Hence, the a-priori choice of the genetic range is important. Let us compare two optimizations which differ only in the range, while the length of the binary chromosome is about the same,

- Testcase GA1: see Table 25;
- Testcase GA2: see Table 26.

The common parameters for the two test-cases are:

- parameterization degree: 6-1-1
- maximum number of GA generations: maxgen=100
- flow solver precision: 10^{-3}

In the two Tables 25 - 26 the control points are numbered according to our convention i-j-k in x, y and z-directions and the displacements in y-direction (minimum and maximum) are in millimeters [mm]. As already said, we move the control points only in y-direction.

We can see in Figs. 72 - 73 the convergence history of the genetic algorithm. On the x-axis we plot the number of generations. Each of the dots on the plot correspond to one shape evaluated in the Euler solver, whose fitness is given on the y-axis.

In Table 27 and in Fig. 74 we can see the best results and shapes obtained with the two choices. The two results are quite different.

Also, we can see in Fig. 73 that after 100 generations, the convergence is still not stagnating, as it is in Fig. 72. Therefore, it is probable that the best solution is not the one shown in Fig. 74.

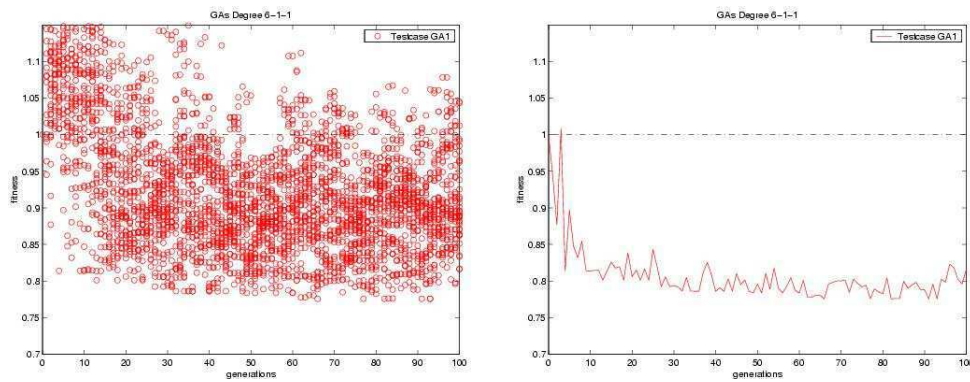


Figure 72: Convergence history (Testcase GA1)

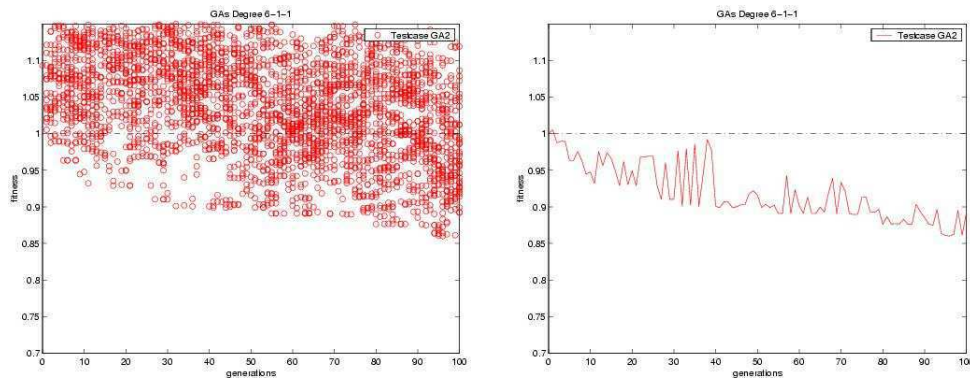


Figure 73: Convergence history (Testcase GA2)

Control points (i,j,k)	min (dY)	max (dY)	accuracy (dY)
0 0 0	0	0	0.1
1 0 0	-25.6	25.6	0.1
2 0 0	-25.6	25.6	0.1
3 0 0	-25.6	25.6	0.1
4 0 0	-25.6	25.6	0.1
5 0 0	-25.6	25.6	0.1
6 0 0	0	0	0.1
0 1 0	0	0	0.1
1 1 0	-25.6	25.6	0.1
2 1 0	-25.6	25.6	0.1
3 1 0	-25.6	25.6	0.1
4 1 0	-25.6	25.6	0.1
5 1 0	-25.6	25.6	0.1
6 1 0	0	0	0.1
0 0 1	0	0	0.1
1 0 1	-25.6	25.6	0.1
2 0 1	-25.6	25.6	0.1
3 0 1	-25.6	25.6	0.1
4 0 1	-25.6	25.6	0.1
5 0 1	-25.6	25.6	0.1
6 0 1	0	0	0.1
0 1 1	0	0	0.1
1 1 1	-25.6	25.6	0.1
2 1 1	-25.6	25.6	0.1
3 1 1	-25.6	25.6	0.1
4 1 1	-25.6	25.6	0.1
5 1 1	-25.6	25.6	0.1
6 1 1	0	0	0.1

Table 25: Testcase GA1: 6-1-1 control points displacement limits and precision in y-direction

Control points (i,j,k)	min (dY)	max (dY)	accuracy (dY)
0 0 0	0	0	0.1
1 0 0	-15.6	35.6	0.1
2 0 0	-25.6	25.6	0.1
3 0 0	-25.6	25.6	0.1
4 0 0	-25.6	25.6	0.1
5 0 0	-25.6	25.6	0.1
6 0 0	0	0	0.1
0 1 0	0	0	0.1
1 1 0	55.6	105.6	0.1
2 1 0	-25.6	25.6	0.1
3 1 0	-15.6	35.6	0.1
4 1 0	-15.6	35.6	0.1
5 1 0	-25.6	25.6	0.1
6 1 0	0	0	0.1
0 0 1	0	0	0.1
1 0 1	-25.6	25.6	0.1
2 0 1	-25.6	25.6	0.1
3 0 1	-25.6	25.6	0.1
4 0 1	-25.6	25.6	0.1
5 0 1	-45.6	5.6	0.1
6 0 1	0	0	0.1
0 1 1	0	0	0.1
1 1 1	-75.6	-25.6	0.1
2 1 1	-25.6	25.6	0.1
3 1 1	-25.6	25.6	0.1
4 1 1	5.6	55.6	0.1
5 1 1	-15.6	35.6	0.1
6 1 1	0	0	0.1

Table 26: Testcase GA2: 6-1-1 control points displacement limits and precision in y-direction

	C_L	C_D	Fitness	Variation
Original	0.3192006583	0.0263540181	1	
Testcase GA1	0.3190283345	0.0204432070	0.775714988	-22.5%
Testcase GA2	0.3218896909	0.0226687454	0.860162770	-14.0%

Table 27: Testcase GA1 and GA2 results

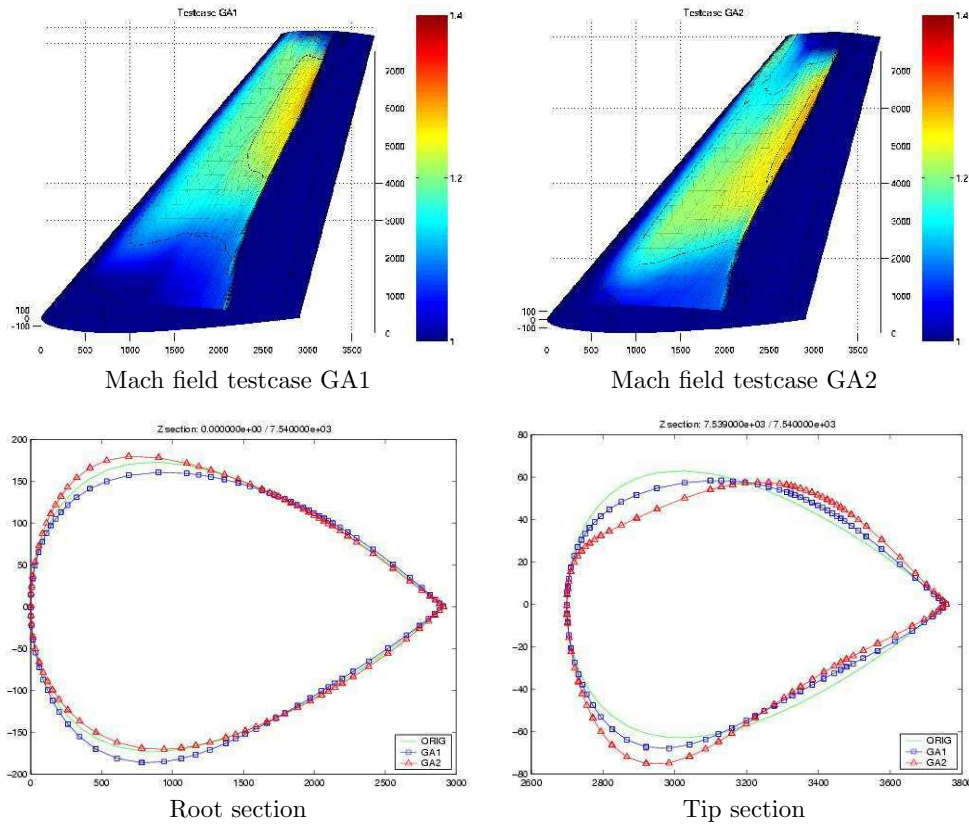


Figure 74: Testcases GA1 and GA2: different Genetic Range

6.10 Genetic algorithm with degree Elevation

It is interesting to see how the degree elevation process works with the genetic algorithms. In this test we will apply the elevation only for the best individual, while the rest of generation is re-set by random perturbation.

The parameters that we choose for this test-case (GA3) are:

- degree : 6-1-1 \rightarrow 9-1-1

- number of generations with one fixed degree: 50
- flow solver precision: 10^{-3}

The *Genetic Range* is the same of the testcase GA1 and can be seen in Tab. 25. The results are shown in Figs. 75 - 76 and in the Tab. 28.

In the left plot of Fig. 75 we see how the fitness of all individuals has been affected by the

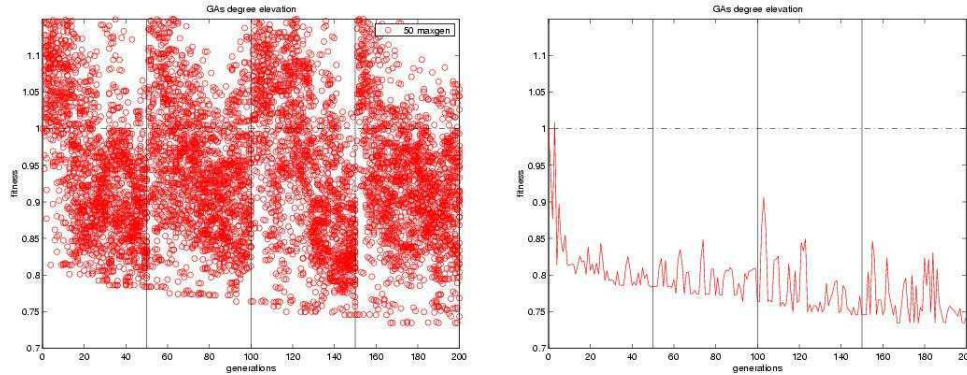


Figure 75: Convergence history (Testcase GA3)

	C_L	C_D	Fitness	Variation
Original	0.3192006583	0.0263540181	1	
Testcase GA3	0.3191186977	0.0193579220	0.734533986	-26.5%

Table 28: Testcase GA3 results

degree elevation process after each 50 generations. The peaks in fitness correspond to the randomly perturbed individuals after the elevation. Nevertheless, we see that the overall mean convergence rate, represented as an envelope of best individuals (Fig. 75 right) is not influenced by the random re-initializations after each elevation.

6.10.1 Non linear flow residual

We want to see if the choice of the non linear flow residual is important for the solution or not. For time reasons, we choose to apply the elevation after 30 generations. The *Genetic Range* can be seen in Tab. 25. The set-up parameters are summarized in Tab. 29.

	res	maxgen
Testcase GA4	10^{-3}	120
Testcase GA5	10^{-6}	120

Table 29: Testcases GA4 and GA5 parameters

The results are shown in Figs. 77 - 78 and in the Tab. 30. The tests were done on a 1 CPU machine PC Pentium 4 at 2.2 GHz, the test-case GA4 with a reduced precision of the flow solver has taken about 10 days, while the test-case GA5 with a good flow-resolution took

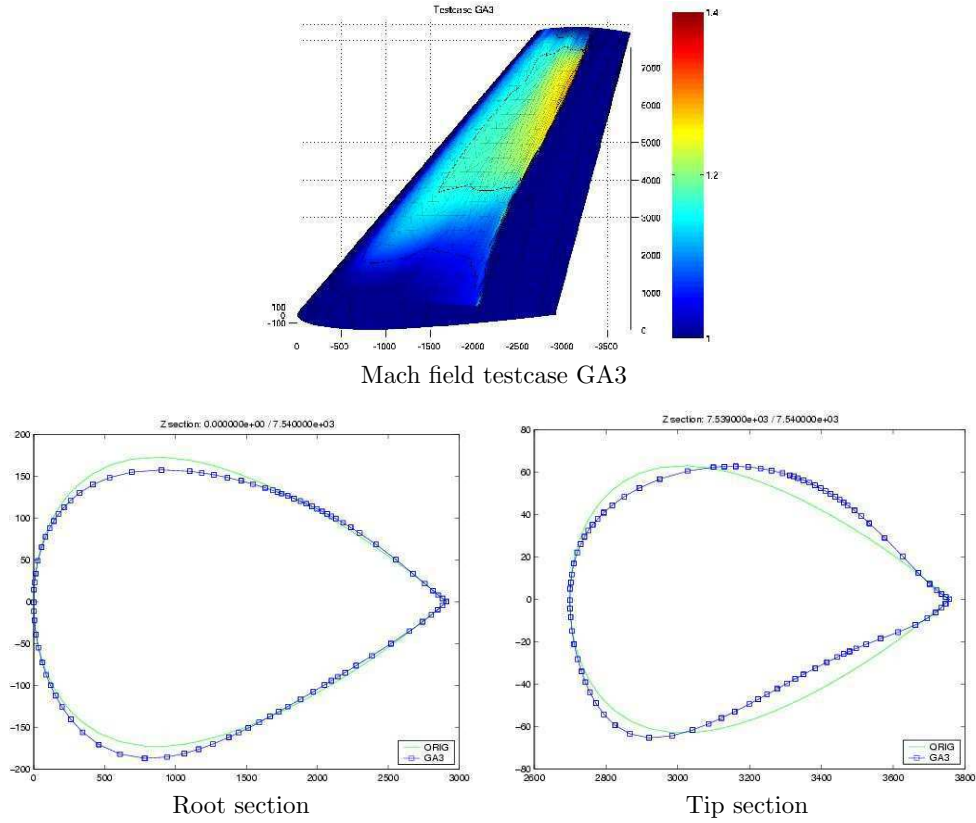


Figure 76: Testcases GA3

26 days. As we are using populations of 40 individuals and as the genetic algorithm offers quite a straightforward parallelization without excessive overheads, we might expect, that on a 40 processor parallel machine the test-cases GA4 and GA5 take about 6 hours and 16 hours, respectively. In order to change the non linear flow residual, the two solutions are qualitatively similar. It is the same result that we have seen in the simplex method.

	C_L	C_D	Fitness	Variation
Original	0.3192006583	0.0263540181	1	
Testcase GA4	0.3200005560	0.0195637896	0.742345601	-25.8%
Testcase GA5	0.3230559605	0.0194338124	0.737435213	-26.3%

Table 30: Testcase GA4 and GA5 results

6.11 Degree elevation vs. fine parameterization only

Like for the simplex method, let us compare one optimization with successively enriched parameterization by degree elevation with an optimization using only the finest parameterization.

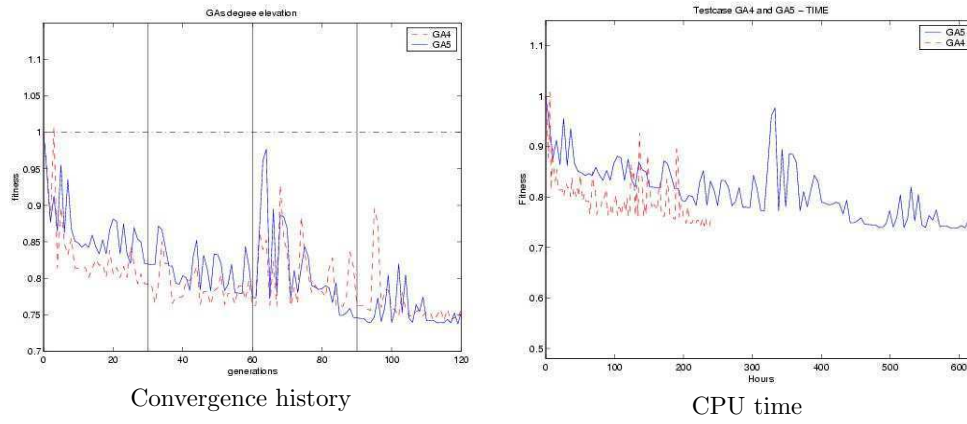


Figure 77: Convergence history (testcases GA4 and GA5) and CPU time

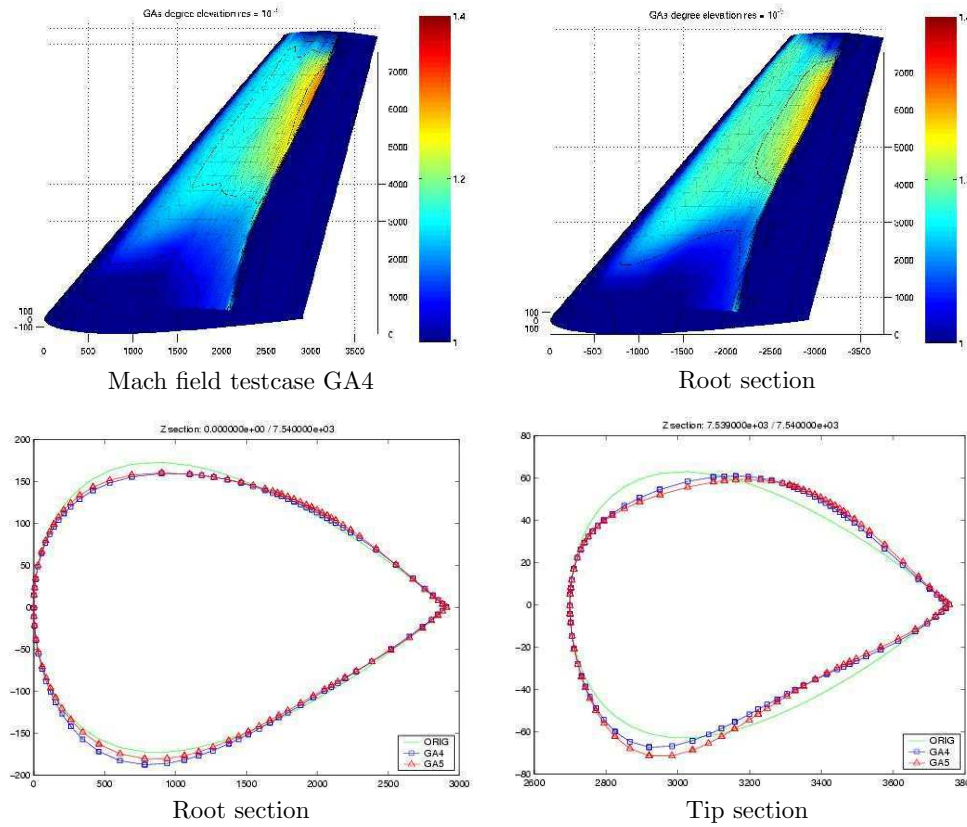


Figure 78: Testcases GA4 and GA5

The parameters set-up is summarized in Tab. 31. The degree elevation is applied every 30 generations.

	degree	res	maxgen
Testcase GA4	6 → 9	10^{-3}	120
Testcase GA6	9-1-1	10^{-3}	100

Table 31: Testcase GA6 parameters

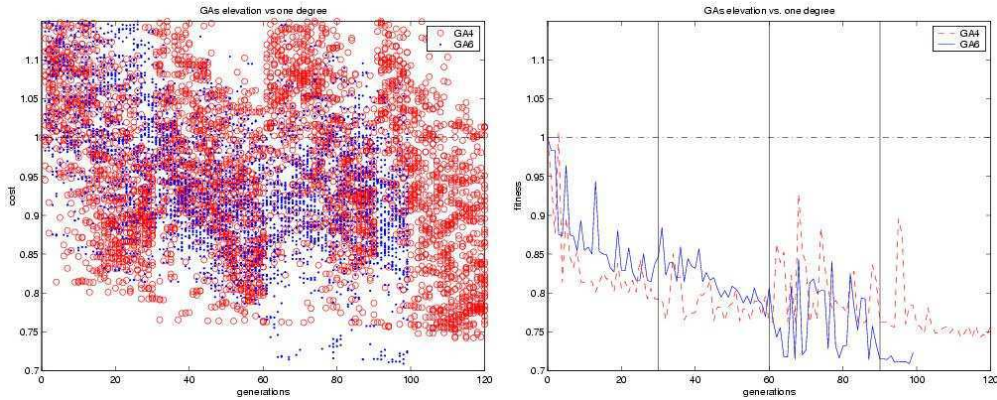


Figure 79: Convergence history (GA4 and GA6)

We can see the convergence history and the results in Fig. 79-80 and in Tab. 32.

	C_L	C_D	Fitness	Variation
Original	0.3192006583	0.0263540181	1	
Testcase GA4	0.3200005560	0.0195637896	0.742345601	-25.8%
Testcase GA6	0.3263465147	0.0186838363	0.708955888	-29.1%

Table 32: Testcase GA4 and GA5 results

A comparison between the degree-elevation strategy and one finest parameterization is difficult to do. While in the first case the speed of convergence is faster, in the second one we are able to find a better solution. One problem should be our choice for the elevation strategy. We have chosen to apply the elevation only for the best individual while the rest of the generation is re-initialized. We can observe what happens choosing a different approach. After some iterations of coarse parameterization we elevate all the individuals for the new degree. A summary of the comparison between the two choices is presented in Tab. 33. The elevation of degree is done every 30 generations.

In Fig. 81 and in Tab. 34 we show the convergence history and the fitness results. The different approaches for the elevation strategy have given two different results. However, it is still not clear how we can transfer information from one level to another using genetic algorithms. While in one case, test-case GA4, we are losing genetic information but gaining in

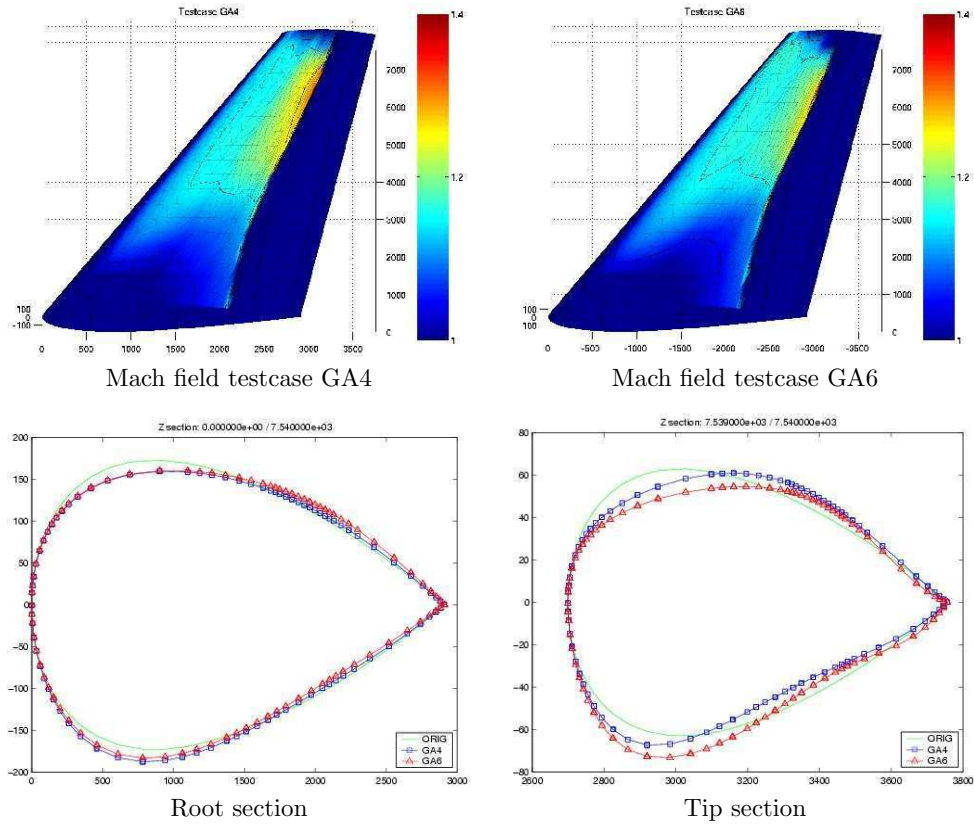


Figure 80: Testcases GA4 and GA6

	res	maxgen
Testcase GA4 (best)	10^{-3}	120
Testcase GA7 (all)	10^{-3}	120

Table 33: Testcase GA7 parameters

	C_L	C_D	Fitness	Variation
Original	0.3192006583	0.0263540181	1	
Testcase GA4 (best)	0.3200005560	0.0195637896	0.742345601	-25.8%
Testcase GA7 (all)	0.3236557100	0.0204623210	0.776441981	-22.4%

Table 34: Testcase GA4 and GA7 results

search versatility, in the other case, test-case GA7, we are doing the contrary. The results are not giving us a clear indication of the behaviour for a multi-level approach. At the same time, the comparison between the degree-elevation process and the finest parameterization of Fig. 79 is not explanatory.

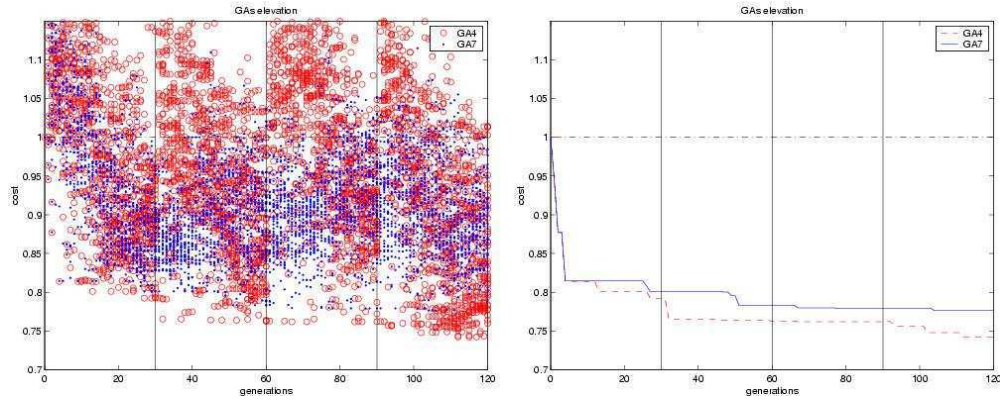


Figure 81: Convergence history (GA4 and GA7)

6.12 Summary and conclusions for GAs experiments

Let us recapitulate the set-up parameters and results for all the tests performed in this Section in Tab. 35.

Testcase	degree	res	gen's	range	C_L	C_D	Variation
Orig		10^{-6}			0.3192007875	0.0263532471	
GA1	6-1-1	10^{-3}	100	Tab. 25	0.3190283345	0.0204432070	-22.5%
GA2	6-1-1	10^{-3}	100	Tab. 26	0.3218896909	0.0226687454	-14.0%
GA3	6→9	10^{-3}	200	Tab. 25	0.3191186977	0.0193579220	-26.5%
GA4	6→9	10^{-3}	120	Tab. 25	0.3200005560	0.0195637896	-25.8%
GA5	6→9	10^{-6}	120	Tab. 25	0.3230559605	0.0194338124	-26.3%
GA6	9-1-1	10^{-3}	100	Tab. 25	0.3263465147	0.0186838363	-29.1%
GA7	6→9	10^{-3}	120	Tab. 25	0.3236557100	0.0204623210	-22.4%

Table 35: GAs results

During all the tests, we have tried to gain some experience with the Genetic Algorithms. The choice of the correct set-up parameters seems fundamental. We have seen, for example with test-cases GA1 and GA2, that a different Genetic Range has an influence not only on the quality of the solution but also in the convergence speed even if the length of the chromosome is about the same. At this time, however, it is not clear how to choose the correct set-up parameters.

The convergence speed is strictly correlated with the size of the population in every generations. The genetic algorithm has more chance to find a good optimal solution if its search space is bigger. However, we are also very limited by the CPU-time.

At this time, we cannot conclude about the advantages and limits for a multilevel approach using genetic algorithms. More tests should give a better understanding of the degree-elevation process.

However, the power of Genetic Algorithm is the possibility to search a trade-off optimum with respect to several criteria by Nash games or Pareto fronts. In all the tests, we have seen

an optimization using a cost function with only one constraint (to keep lift). In Aerodynamics, more constraints can be applied (e.g. volume preserving, thickness, momentum coefficient, lift distribution in span-wise direction, twist and other) and the ability of genetic algorithms to implement a multi-point optimization will become necessary (e.g. subsonic regime, transonic regime, landing, take-off and other). Genetic Algorithms are one of the unique algorithms able to solve multi-objective and multi-point optimization problems (Pareto front, Nash game) in a very transparent way.

7 Conclusions and perspectives

This work has been intended to give preliminary experiments and bring up some interesting questions about hierarchical parametrizations for 3D aerodynamic bodies. We were particularly interested in testing Bezier parametrization and free-form deformation, and verifying that a multi-level approach improves the convergence rate of optimization algorithms.

To this point, we have implemented to an existing Euler solver the parametrization and elevation routines and the whole external loop of generic optimization algorithms, either by simplex method or by genetic algorithm. Thus, we have created a new optimization package capable to deal with fairly general 3D geometries. The code will be used for future developments by the OPALE team, besides other things, in the framework of the Supersonic contract with the French government and in technical collaboration with Piaggio Aero Industries.

It appears, based on our experiments with the simplex method, that the multi-level approach in this framework might be of interest, helping to unlock the stiff optimization problem. Our tests with genetic algorithm are not so conclusive. Nevertheless, they bring up some questions about the optimal way of transfer of genetic information at the elevation process.

The future work should concentrate on the implementation of a trully multigrid-like hierarchical optimization, with not only successive enriching of parametrization, but also with parametrization coarsening. The idea is to decouple, by the means of the hierarchical parametrization, the high and low frequencies of shape deformation and treat them quasi-separately, the coupling between them being reduced to repeatedly performed degree elevation and degree reduction processes.

Also, the high CPU-cost of the genetic algorithm is an obstacle to a successful use of genetic optimization in an engineering design loop. With this respect, we propose as a necessary step, to either hybridize genetic algorithm [36] to speed up its convergence, or to use interpolation techniques [2], reduced model for flow problem [15] or neural networks [18].

References

- [1] Coquillart, S. Extended free form deformation: a sculptural tool for 3D geometric modelling, SIGGRAPH 24,4 (1990), pp. 187–196.
- [2] Berard, Y. and Habbal, A: Algorithmes génétiques perturbés par le gradient, to appear as INRIA Research Report.
- [3] Darwin, C. On the origin of species by means of natural selection, London, John Murray, 1859 [1st edn.].
- [4] Dolean, V. and Lanteri, S.: A domain decomposition approach to finite volume solutions of the Euler equations on triangular meshes, INRIA Research Report 3751, August 1999.
- [5] Duvigneau, R.: Contribution à l’optimisation de forme pour des écoulements à forts nombres de Reynolds autour de géométries complexes, Thèse de Doctorat, Octobre 2002, Ecole Centrale de Nantes.
- [6] Farhat, C., Degand, C., Koobus, B., Lesoinne, M.: Torsional springs for two-dimensional dynamic unstructured fluid meshes, *Comput. Methods Appl. Mech. Engrg.* 163 (1998), pp. 231–245.
- [7] Farhat, C., Degand, C.: A three-dimensional torsional springs analogy method for unstructured dynamic meshes, *Computer and Structures* 80 (2002) 305–316.
- [8] Fezoui, L. and Stoufflet, B.: A class of implicit upwind schemes for Euler simulations with unstructured meshes, *J. of Comp. Phys.*, 84 (1989), pp. 174–206.
- [9] Fisher, CF. and Arena, AS. On the Transpiration Method for Efficient Aeroelastic Analysis Using an Euler Solver, AIAA 96-3436, American Institute of Aeronautics and Astronautics, 1996.
- [10] George, PL. and Frey, PJ.: *Maillages applications aux éléments finis*, Hermes, 1999.
- [11] George, PL. and Borouchaki, H.: *Triangulation de Delaunay et maillage*, Hermes, 1997.
- [12] Hadamard, J.: *Leçon sur le calcul des variations*, Gauthier Villars, 1910.
- [13] Haug, EJ. and Cea, J.: *Optimization of distributed parameter structures*, vol 1 and 2, Sitjhoff and Noordhoff, 1981.
- [14] Huffman, W.; Melvin, R.; Young, D.; Johnson, J.; Bussoletti, J.; Bieterman, M. and Hilmes, C.: *Practical Design and Optimization in Computational Fluid Dynamics*, AIAA Paper 93-3111, 1993.
- [15] Iollo, A.; Lanteri, S.; Désidéri, JA.: Stability Properties of POD-Galerkin Approximations for the Compressible Navier-Stokes Equations, INRIA Research Report no. 3589, December 1998.
- [16] Jameson, A.: Optimal Shape Design for Aerodynamics, in *Optimum Design methods for Aerodynamics*, AGARD Report 803, J. Periaux, Special Course Director at the VKI, Rhode Saint-Gense, Belgium, 25-29 april 1994.
- [17] Jameson, A.: *Optimum Aerodynamic Design via Boundary Control*, AGARD Report 803, VKI Lectures, 1994.

- [18] Karakis, M.; Désidéri, J.A.: Model Reduction and Adaption of Optimum-shape design in aerodynamics by Neural Networks, INRIA research Report no. 4503, July 2002.
- [19] Kuiper, H.; van der Wees, A.J.; Hendriks, C.F., Labrujere, T.E.: Application of genetic algorithms to the design of airfoil pressure distribution, NLR Technical publication TP95342L for the ECARP European Project.
- [20] Labrujere, T.: Residual-Correction Type and Related Computational Methods for Aerodynamics, AGARD Report 803, J. Periaux, Special Course Director at the VKI, Rhode Saint-Genese, Belgium, 25-29 april 1994.
- [21] Lagarias, J.; Reeds, J.; Wright, M.: Convergence properties of the Nelder-Mead algorithm in low dimensions, SIAM Journal on Optimization 9 (1998), pp.112–147.
- [22] Lamousin, H. and Waggenspack, W.: NURBS-Based Free-Form Deformation, IEEE Computer Graphics and Applications, Vol.14, No.6, 1994, pp. 1–9.
- [23] Lewis, R.; Torczon, V. and Trosset, M.: Direct search methods: Then and now, ICASE Report, 2000.
- [24] Lighthill, M.J.: A new method of two-dimensional aerodynamics design, R&M1111, Aeronautical Research Council, 1945.
- [25] Lighthill, M.J.: On Displacement Thickness, Journal of Fluid Mechanics 4, 1958, pp.383–392.
- [26] Lions, J.L.: Optimal control of system governed by PDEs, Springer Verlag, New York, 1971.
- [27] Marco, N. and Dervieux, A.: Multilevel Parametrization for Aerodynamical Optimization of 3D Shapes, INRIA Research Report no. 2949, July 1996.
- [28] Marco, N., and Désidéri, J.A.: Numerical solution of optimization test-case by Genetic Algorithms, INRIA Research Report no. 3622, February 1999.
- [29] Marco, N., Désidéri, J.A. and Lanteri, S.: Multi-Objective Optimization in CFD by Genetic Algorithms, INRIA Research Report no. 3686, April 1999.
- [30] Marco, N.; Lanteri, S.: A Two-Level Parallelization Strategy for Genetic Algorithms Applied to Shape Optimum Design, INRIA Research Report no. 3463, July 1998.
- [31] Marocco, A.: Simulations Numériques dans la Fabrication des Circuits à Semiconducteurs, INRIA Research Report no. 0305.
- [32] Mohammadi, B.; Pironneau, O.: Applied Shape Optimization for Fluids, Clarendon Press, Oxford, 2001.
- [33] Mühlenbein, H.; Schomisch, D. and Bord, J.: The Parallel Genetic Algorithm as Function Optimizer, Parallel Computing 17 (1991), pp. 619–632.
- [34] Nelder, J.A., Mead, R.: A simplex method for function minimization, Computer Journal 7 (1965), pp.308–313.

-
- [35] Obayashi, S.; Oyama, A.: Three dimensional aerodynamic optimization with genetic algorithms Third ECCOMAS Computational Fluid Dynamics Conference and Second ECCOMAS Conference on Numerical Methods in Engineering, volume Computational Fluid Dynamics '96, John Wiley & Sons, 1996 pp. 420–424.
- [36] Oulladji, L.; Janka, A.; Désidéri, JA.; Dervieux, A.: Optimisation aérodynamique par algorithmes génétiques hybrides: application à la réduction d'un critère de bang sonique, INRIA Research Report no. 4884, July 2003.
- [37] Périaux, J.; Sefrioui, M.; Stoufflet, B.; Mantel, B.; Laporte, E.: Robust genetic algorithms for optimization problems in aerodynamic design, Genetic algorithms in engineering and computer science, John Wiley & Sons 1995, pp. 397–415.
- [38] Pironneau, O.: Optimal shape design for elliptic systems, Springer-Verlag, New York, 1984.
- [39] Powell, M.: Direct search algorithms for optimization calculations, Acta Numerica 7 (1998), pp. 287–336.
- [40] Quagliarella, D.: Genetic algorithms applications in computational fluid dynamics, Genetic algorithms in engineering and computer science, John Wiley & Sons, 1995 pp. 417–442.
- [41] Raj, P. and Harris, B.: Using Surface Transpiration with an Euler Method for Cost-effective Aerodynamic Analysis, AIAA 93-3506, American Institute of Aeronautics and Astronautics, 1993.
- [42] Roe, PL.: Approximate Riemann solvers, parameter vectors and difference scheme, J. of Comp. Phys., 43 (1981), pp.357–371.
- [43] Samareh, J.: A survey of shape parameterization techniques, CEAS AIAA ICASE NASA Langley International Forum on Aeroelasticity and Structural Dynamics, June 1999.
- [44] Sederberg, T. and Parry, S.: Free-Form Deformation of Solid Geometric Models, Computer Graphics 20, no. 4 (1986), pp. 151–160.
- [45] Spendley, W.; Hext, GR.; Himsworth, FR.: Sequential application of simplex designs in optimization and evolutionary operation, Technometrics 4 (1962), pp. 441–461.
- [46] Thompson, JF., Warsi, ZUA. and Mastin, CW.: Numerical Grid Generation, North Holland 1985, <http://www.erc.msstate.edu/publications/gridbook>.
- [47] Törn, A. and Zilinskas, A.: Global Optimization, Lecture Notes in Computer Science, no. 350, Springer-Verlag, Berlin, 1989.
- [48] Toro, EF.: Riemann Solvers and Numerical Methods for Fluid Dynamics, Springer 1997.
- [49] van Leer, B.: Towards the ultimate conservative differences scheme V : a second-order sequel to Godunov's method J. of Comp. Phys., 32 (1979), pp. 361–370.



Unité de recherche INRIA Sophia Antipolis
2004, route des Lucioles - BP 93 - 06902 Sophia Antipolis Cedex (France)

Unité de recherche INRIA Futurs : Parc Club Orsay Université - ZAC des Vignes
4, rue Jacques Monod - 91893 ORSAY Cedex (France)

Unité de recherche INRIA Lorraine : LORIA, Technopôle de Nancy-Brabois - Campus scientifique
615, rue du Jardin Botanique - BP 101 - 54602 Villers-lès-Nancy Cedex (France)

Unité de recherche INRIA Rennes : IRISA, Campus universitaire de Beaulieu - 35042 Rennes Cedex (France)

Unité de recherche INRIA Rhône-Alpes : 655, avenue de l'Europe - 38334 Montbonnot Saint-Ismier (France)

Unité de recherche INRIA Rocquencourt : Domaine de Voluceau - Rocquencourt - BP 105 - 78153 Le Chesnay Cedex (France)

Éditeur
INRIA - Domaine de Voluceau - Rocquencourt, BP 105 - 78153 Le Chesnay Cedex (France)
<http://www.inria.fr>
ISSN 0249-6399